Characterization of the ^{229}Th nuclear clock transition

Benedict Seiferle

München 2019

Characterization of the ^{229}Th nuclear clock transition

Benedict Seiferle

Dissertation
an der Fakultät für Physik
der Ludwig–Maximilians–Universität
München

vorgelegt von
Benedict Seiferle
aus Bad Säckingen

München, den 29. August 2019

Erstgutachter: PD Dr. Peter G. Thirolf
Zweitgutachter: Prof. Dr. Thomas Udem
Tag der mündlichen Prüfung: 11.10.2019

Zusammenfassung

Charakterisierung des ^{229}Th Kernuhren-Übergangs

Von allen derzeit ca. 180 000 bekannten nuklearen Energieniveaus besitzt der erste (isomere) angeregte Zustand in ^{229}Th (genannt ^{229m}Th oder "Thorium-Isomer") die niedrigste Anregungsenergie von weniger als 10 eV. Seine Energie ist mit modernen Lasern erreichbar und erlaubt daher die direkte Laseranregung eines Kerns. Das eröffnet ein neues Feld der Laser-basierten Kernspektroskopie, das zu einer Vielzahl von Anwendungen führen könnte. Als prominentestes Beispiel ist die Realisierung einer Kernuhr zu nennen, die neben praktischen Anwendungen z.B. in relativistischer Geodäsie oder satellitengestützter Navigation zur Suche nach dunkler Materie oder der Untersuchung der zeitlichen Konstanz von Fundamentalkonstanten eingesetzt werden könnte. Ein seit langem bestehendes Problem bestand darin, dass nur sehr wenig über diesen angeregten Zustand bekannt war. Aus diesem Grund bestand das Ziel dieser Arbeit in einer genauen und direkten Energiemessung, sowie einer ersten Lebensdauermessung dieses Übergangs.

Die Lebensdauer des ^{229}Th-Isomers hängt stark von seinem Ladungszustand ab, da durch diesen verschiedene Zerfallskanäle energetisch verboten oder erlaubt sind. Es lassen sich zwei Zerfallskanäle unterscheiden, γ-Zerfall und innere Konversion (IC), wobei Letzerer um Größenordnungen schneller verläuft. In diesem Zerfallskanal wechselwirkt der Kern direkt mit den Hüllenelektronen des Atoms und gibt seine Energie an ein Elektron ab, das daraufhin die Hülle verlässt und ^{229}Th als Ion zurücklässt. Über die kinetische Energie dieses Elektrons lässt sich daraufhin die Energie des angeregten Kernzustands bestimmen. Im Fall von ^{229m}Th ist dieser Zerfallskanal nur in neutralen ^{229m}Th Atomen erlaubt, da nur hier die Energie ausreicht, um ein Elektron aus der Hülle zu entfernen. Im Rahmen dieser Arbeit wurde der IC-Kanal benutzt, um ^{229m}Th zu charakterisieren. Erste Messungen der Lebensdauer wurden mit neutralen, auf einer Oberfläche deponierten ^{229m}Th-Atomen durchgeführt. Zusätzlich wurden Energiemessungen der emittierten Konversionselektronen durchgeführt. Die daraus resultierenden

Ergebnisse werden schließlich die Entwicklung eines Lasers ermöglichen, der für die direkte optische Anregung des ersten angeregten Kernzustands in ^{229}Th und somit für die Realisierung einer Kernuhr genutzt werden kann.

Der experimentelle Aufbau, der in dieser Arbeit benutzt wurde, basiert auf einer Puffergas-Stoppzelle, die verwendet wurde um $^{229(m)}$Th-Ionen aus einer ^{233}U α-Rückstoßquelle zu thermalisieren und zu extrahieren. Zur Verbesserung des Signal-zu-Untergrund-Verhältnisses für eine Energiemessung und um Lebensdauermessungen zu ermöglichen, wurden Phasenraum-gekühlte Ionenpakete in einem Radiofrequenz-Quadrupol-Buncher (RFQ-Buncher) erzeugt. Für Lebensdauermessungen wurden die Ionenpakete direkt auf einem Mikrokanal-Platten-Detektor gesammelt, wo die Ionen neutralisierten und der angeregte Kernzustand anschließend über innere Konversion in den Grundzustand zerfiel. Es wurde eine Halbwertszeit von 7$\pm$1 μs gemessen. Des Weiteren konnte gemessen werden, dass die Lebensdauer stark von der elektronischen Umgebung des Kerns abhängt.
Um die Energie des angeregten Kernzustands erstmalig direkt zu messen, wurden $^{229(m)}$Th Ionen zur Neutralistation durch doppel-lagiges Graphen gesendet. Anschließend flogen ^{229m}Th Atome durch ein Elektronenspektrometer vom Typ einer magnetischen Flasche mit Retardierungspotential. Der angeregte Kernzustand kann dadurch im Flug zerfallen und die kinetische Energie des Konversionselektrons kann mit dem Spektrometer gemessen werden. Eine sorgfältige Analyse sowie der Vergleich mit theoretischen Vorhersagen erlaubte es, die Anregungsenergie von ^{229m}Th zu 8.28$\pm$0.17 eV zu bestimmen. Der seit über 10 Jahren gültige und indirekt gemessene Referenzwert, lässt sich damit durch einen mit dreifach verbesserter Genauigkeit und erstmals direkt gemessenen Wert ersetzen.

Die vorliegende Arbeit ist wie folgt strukturiert: Das erste Kapitel besteht aus einer Einführung und gibt einen Überblick über bisherige Energiemessungen an ^{229m}Th, fasst aktuelle experimentelle Ansätze zusammen und zeigt mögliche Anwendungen auf. Das zweite Kapitel beschreibt die theoretischen Grundlagen. Der experimentelle Aufbau, sowie vorbereitende Messungen zur Charakterisierung des Aufbaus sind in Kapitel 3 und 4 beschrieben. Lebensdauer- und Energiemessungen befinden sich in Kapitel 5 und 6. Das letzte Kapitel liefert eine abschließende Zusammenfassung und einen Ausblick.

Abstract

Characterization of the ^{229}Th nuclear clock transition

Of all presently known about 180,000 excited nuclear states, the first isomeric excited state of ^{229}Th (called $^{229\mathrm{m}}$Th or 'thorium isomer') has the lowest excitation energy of less than 10 eV. Its energy is accessible with today's laser technology and therefore allows for direct laser excitation of a nucleus. This opens up a new field of precision nuclear spectroscopy leading to a multitude of applications, such as the realization of a nuclear clock, which, besides utilization in relativistic geodesy or satellite-based navigation, could be employed in dark-matter research or the investigation of a potential temporal variation of fundamental constants. A long-standing problem, however, was that not much was known about the properties of the excited state. Therefore the goal of the thesis was to provide measurements of the energy and lifetime of the first excited state in ^{229}Th.

The lifetime of the ^{229}Th nuclear isomer depends strongly on its charge state, as different charge states make it possible to energetically open or close decay channels. There exist two main decay channels, γ decay and internal conversion (IC), where the latter proceeds several orders of magnitude faster than the former. In this decay channel the nucleus interacts with the electronic shell of the atom and transfers the energy of the excited nuclear state to a shell electron, thereby ionizing the atom. The kinetic energy of the expelled electron allows to conclude on the isomer's energy. For $^{229\mathrm{m}}$Th this is only possible in a neutral atom, as only in this case the nuclear excitation energy exceeds the electron binding energy. Within the scope of this thesis, the IC decay channel was used to investigate the properties of the isomer. First measurements of the lifetime of $^{229\mathrm{m}}$Th in neutral, surface-bound atoms were realized. Additionally, energy measurements using the emitted internal conversion electrons were performed. The results will allow to develop a laser that can be used for a direct optical excitation of the first excited nuclear state in ^{229}Th and thus for the realization of nuclear clock.

The experimental setup that is employed in this thesis consists of a buffer-gas stopping cell that is used to thermalize and extract $^{229(m)}$Th ions from a ^{233}U α-recoil source. In order to measure the lifetime of ^{229m}Th following the decay by internal conversion and to increase the signal-to-noise ratio for energy measurements, phase-space cooled $^{229(m)}$Th ion bunches are generated in a radio-frequency quadrupole (RFQ) ion buncher. For lifetime measurements, the ions are collected directly on the surface of an MCP detector, where they neutralize and subsequently decay via internal conversion. A half-life of 7$\pm$1 μs was measured. Moreover, a strong dependence of the lifetime on the electronic environment of the nucleus could be shown.
In order to measure the excitation energy of the isomeric state, $^{229(m)}$Th ions are sent through a bi-layer of graphene for neutralization. They continue their flight as neutral atoms through a magnetic-bottle type retardation electron spectrometer. The isomeric state decays in-flight and the kinetic energy of the emitted internal conversion electrons can be measured with the spectrometer. By a careful analysis and comparison with theoretical spectra it is possible to measure the isomeric energy to 8.28$\pm$0.17 eV. Thus, the present reference value of 7.8(5) eV, measured indirectly more than 10 years ago, could be replaced with threefold improved precision.

The thesis is structured as follows: The first chapter provides an introduction to the isomeric first excited state in ^{229}Th, gives a short overview on previously performed energy measurements, summarizes current experimental approaches and outlines possible applications.
The second chapter summarizes the theoretical background. The experimental setup is detailed in the third chapter and its characterization in preparatory measurements is described in chapter 4. Lifetime and energy measurements are presented in chapter 5 and 6, respectively. The last chapter provides a conclusion and an outlook.

Contents

CHAPTER 1

Introduction & Motivation

Nuclear and atomic physics are situated in completely different energy regions: While the energies that are normally associated with nuclei range from keV to MeV, energies related to atoms are orders of magnitude lower and situated in the meV to eV regime. This large difference is also reflected in the methods that are used to manipulate nuclei and atoms.

There exists only one nuclear excited state with an excitation energy comparable to the excitation energies found in atoms: The isomeric first excited state in ^{229}Th with an excitation energy of (as will be determined in the course of this thesis) only 8.28±0.17 eV [1]. Although it is a nuclear excited state, the first isomeric state of ^{229}Th can be investigated with methods known from atomic physics.
A long-standing problem was that the properties of this first excited state were not known to high precision. This has hindered the utilization of $^{229\mathrm{m}}$Th for the multitude of applications that have been proposed in the literature over the last four decades. Therefore, the goal of this thesis is to form a bridge between these fields and to measure the properties of the isomeric transition with a precision and reliability such that a dedicated laser can be developed to directly optically excite the isomeric state in ^{229}Th ions confined in a Paul trap, which forms the basis of a nuclear optical clock.
In the following chapter, a short overview of the properties of the isomeric state (section 1.1) as well as a short introduction to the measurements that led to the current knowledge on the thorium isomer (sections 1.2 and 1.3) will be given. At the end of this chapter, in section 1.4, a nuclear frequency standard based on ^{229}Th together with its applications will be detailed and an overview of current experimental research on $^{229\mathrm{m}}$Th will be given.

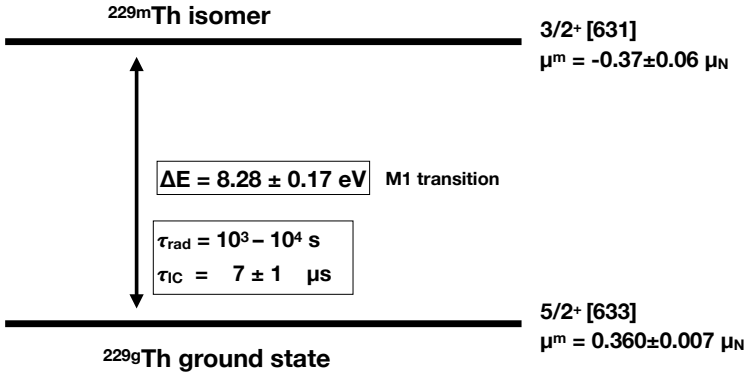

Figure 1.1: Level scheme of ^{229}Th, showing the ground state and the first excited isomeric state together with its magnetic moments, Nilsson quantum numbers and decay properties.

1.1 The isomeric first excited state of ^{229}Th

The first excited state of ^{229}Th, denoted with $^{229\mathrm{m}}$Th[1], exhibits the lowest excitation energy of all presently known nuclear excited states. A nuclear level scheme including the ground state and the isomeric state is shown in Fig. 1.1. Its energy is in the eV range, which makes the first nuclear excited state in ^{229}Th the only presently known nuclear state that can be excited with a laser. The outstanding position of the ^{229}Th isomer in contrast to other nuclear isomers is visualized in Fig. 1.2, where a compilation of all nuclear isomers (*i.e.* lifetime longer than 10^{-9} s) is displayed in a plot of excitation energy versus half-life (blue symbols), in comparison with selected electronic transitions used for precision laser spectroscopy experiments or atomic clocks.
In the recent decades, especially after the proposal of a nuclear optical clock based on $^{229\mathrm{m}}$Th (see section 1.4), interest in the isomeric state was growing. However, still today, the direct optical excitation of the thorium isomer has not been achieved. The main reason is the imprecise knowledge of the isomer's properties, especially its excitation energy. In the following sections the possible decay channels as well as possible ways to populate the isomeric state will be discussed briefly.

[1] where *m* stands for 'metastable' and indicates a lifetime longer than 10^{-9} s, which qualifies an excited state as a nuclear isomer.

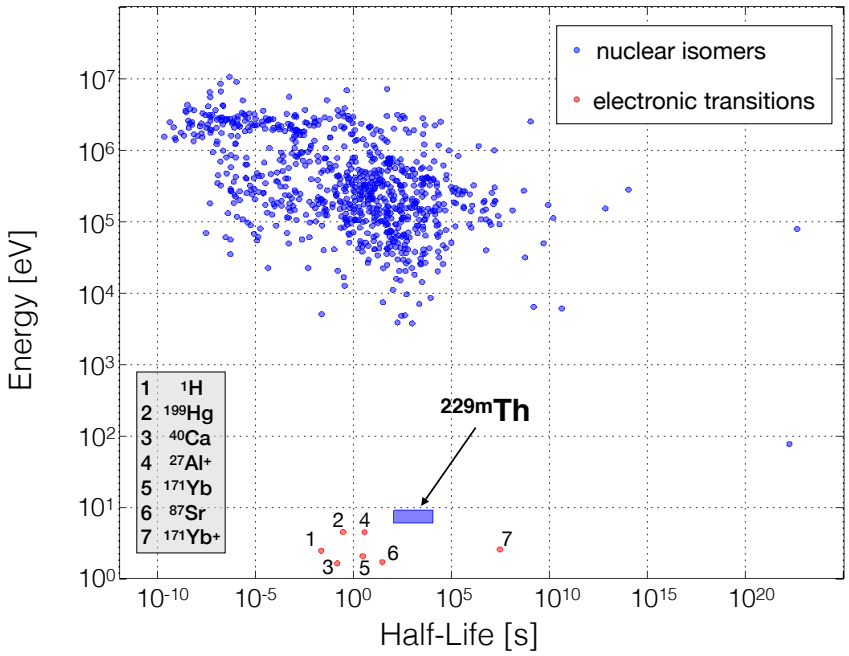

Figure 1.2: Scatter plot that visualizes the half-life and excitation energy of all known nuclear isomers (blue, data taken from [2]) and of a selection of electronic transitions which are used in precision laser spectroscopy experiments, including transitions that are currently used in optical atomic clocks (red) [3]. The plot is adapted from Ref. [4].

1.1.1 Decay channels of ^{229m}Th

The isomer-to-ground-state transition, ^{229m}Th $\rightarrow ^{229}$Th, can proceed via several decay channels, which are detailed in the following section. The possible decay channels are schematically shown in Fig. 1.3.
In the γ decay (Fig. 1.3a , with an expected lifetime of up to 10^4 s [5–7], a photon is emitted carrying the transition energy of the isomer (see also section 2.2).
Besides γ decay, an alternative decay channel for nuclear excited states (especially important for excited states of low energy in high-Z isotopes) is internal conversion (IC), shown in Fig. 1.3b. In this decay mode, the nuclear transition energy is directly transferred to the electrons in the vicinity of the nucleus. The IC decay rate depends on the spatial overlap of the nuclear and electronic wavefunctions (see for example [8] or [9]). Therefore, typically, IC proceeds predominantly via inner shell electrons. For ^{229m}Th the situation is different: Generally, the IC decay channel is energetically possible when the binding energy of the ejected electron is smaller than the transition energy of the nuclear excited state [8, 9]. In case of ^{229m}Th, IC is therefore only possible for neutral ^{229}Th, because only then the electron's binding energy (given by the first ionization potential, which is well-known as IP$\approx$ 6.31 eV [10]), lies below the excitation energy of ^{229m}Th. The energy of the isomer is transferred to an electron in the electronic shell, which is subsequently emitted into the continuum within microseconds [11] (for details see section 5). This has two consequences: First, by removing valence electrons it is possible to completely suppress IC as a decay channel. Second, as the IC lifetime depends on the overlap between the nuclear and electronic wavefunctions, it is expected that the lifetime is strongly influenced by the chemical environment of ^{229m}Th [12].

In the bound internal conversion decay (BIC, Fig. 1.3c), also called resonant internal conversion [13–15], the energy of the isomer is transferred to the electronic shell and promotes an electron to an excited state. BIC is a resonant process that is only possible when an electronic transition exists with the same energy as the nuclear isomer. The excited electronic state then decays to its ground state via the emission of photons.
There also exists a third-order process, where a 'virtual' electronic state is populated, which subsequently decays to a lower electronic state by photon emission. This process is called electronic bridge (EB) and schematically shown in Fig. 1.3d.

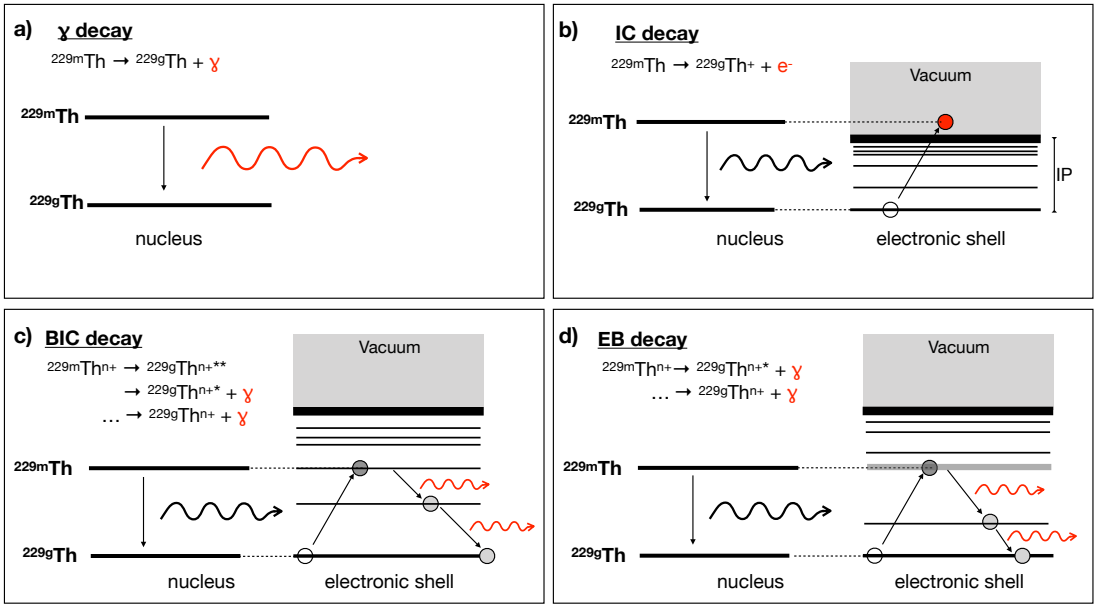

Figure 1.3: The four ground-state decay channels of the isomeric state in ^{229}Th. The signature of each process (*i.e.* the emitted particle) is shown in red: a photon in the γ decay (panel a), an electron in the internal conversion (IC) decay (panel b) and photons from electronic excited states in the bound internal conversion (BIC) or electronic bridge (EB) processes, panel c and d, respectively. It should be noted, that the intermediate level in the electronic-bridge decay is virtual (visualized with the light-grey line).

1.1.2 ^{229m}Th population

There are several ways to populate the isomer. The different excitation schemes are depicted in Fig. 1.4.
The isomer can be excited directly in a transition from the ground state to the isomeric state. This can be achieved via the inverse processes of the decay channels described above: (*i*) direct laser excitation, which requires a photon with an energy that is resonant with the isomer, (*ii*) nuclear excitation by electron capture (NEEC), where an ion recombines with an electron and the energy is transferred to the nucleus, thereby exciting the isomer. This can be understood as the inverse process of internal conversion. (*iii*) There exist also the inverse processes of bound internal conversion and electronic bridge, where an electronic excited state (depicted by the dashed line in Fig. 1.4a) decays to a different electronic state (not neccessarily the ground state) and populates the isomer in ^{229}Th [16]. For EB the electronic excited state is virtual.
Alternatively, the isomer can also be populated naturally in the radioactive decay of other isotopes, for example in the α decay of ^{233}U (with a 2% branching ratio [17]) or the β decay of ^{229}Ac (with a branching ratio of at least 14% [18, 19]).
Another way to populate the isomer is by first exciting a higher-lying nuclear state, which then decays to ^{229m}Th. This was achieved only recently [20]: the second excited state in ^{229}Th (at about 29 keV) has been successfully excited using resonant synchrotron radiation. In its decay it feeds the ground state with a branching ratio of ≈89% [20], which allows for an efficient population of ^{229m}Th.

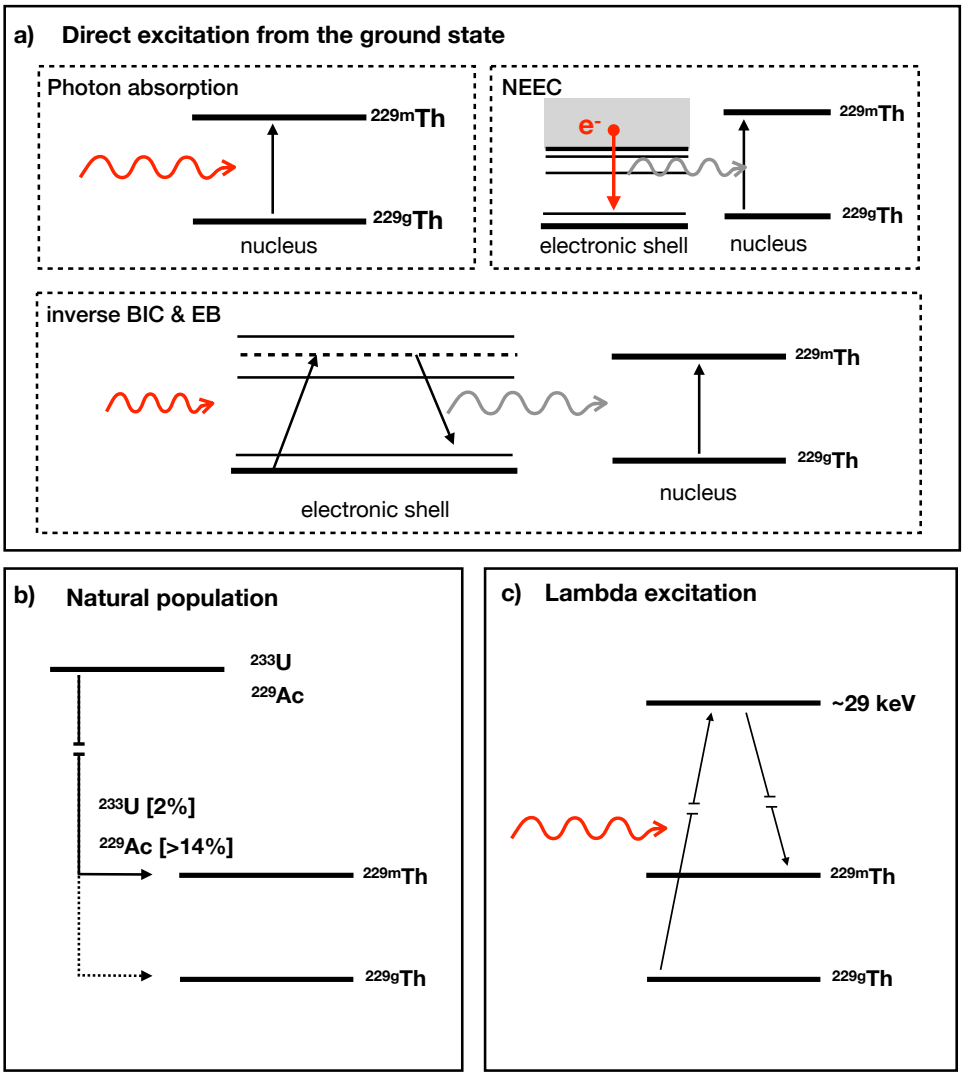

Figure 1.4: Visualization of excitation schemes that can be used to populate the first excited state in ^{229}Th. Direct excitation (panel a refers to the excitation from the ground-state and includes all inverse processes shown in Fig. 1.3: photon absorption as the inverse process of γ decay, nuclear excitation by electron capture (NEEC) as the inverse internal conversion process and inverse BIC and electron bridge (EB). The isomer is also populated naturally in α- and β decays of ^{233}U and ^{229}Ac, respectively (panel b). The branching ratios to the isomeric first excited state are given with 2% (^{233}U) and at least 14% (^{229}Ac). Additionally a Lambda-excitation scheme via the second excited state (at $\approx$ 29 keV) is shown. Further details are given in the text.

1.2 Indirect energy measurements of ^{229m}Th

Prior to this work, knowledge of the isomeric energy was obtained in indirect measurements (*i.e.* using differences of γ transitions originating from higher-lying excited states populating the ground state and the isomeric state). Starting with first evidence of a low energy isomeric state in 1976 [21] up to a first direct detection of the isomer in 2016 [4], a precise energy determination of the isomeric energy has been a long-standing problem.

First hints at ^{229m}Th

First evidence for the existence of a low energy state in ^{229}Th was discovered in 1976 by Kroger and Reich as they investigated the γ radiation which follows the α decay from ^{233}U to ^{229}Th [21]. From these measurements they deduced a level scheme and suggested a rotational band head with spin-parity numbers $I^{\pi} = 3/2^{+}$ and an excitation energy below 100 eV. Evidence for such a low excited state could not be found directly, since the splitting between the ground state and the first excited state could not be resolved. The low-lying excited state was interpreted as the $\frac{3}{2}^{+}[631]$ Nilsson orbital. Shortly after, in 1977, the ^{229}Th level structure was re-examined by Canty et al. [22] and the interpretation of a low-energy state with $\frac{3}{2}^{+}[631]$ was strengthened.
Further examination of the nuclear structure of ^{229}Th was performed in ^{230}Th(d,t)^{229}Th reactions by Burke et al. [23]. Angle-resolved measurements allowed to assign l-values to the energy levels. By comparing cross-section patterns for (d,t)-reactions in ^{232}Th(d,t)^{231}Th and ^{230}Th(d,t)^{229}Th, the band assignment was put to test. These investigations gave evidence of two rotational bands with band heads at $\frac{5}{2}^{+}[633]$ (for the ground state) and $\frac{3}{2}^{+}[631]$ (for the isomeric state).

A first indirect energy determination of ^{229m}Th

While in the measurements described above information on the energy of the ground-state doublet was inferred by the fact that it could not be resolved, Reich and Helmer performed a first indirect energy measurement in 1990 [24]. In their experiment they again used γ rays which were emitted after the α decay of ^{233}U. In order to obtain a value for the isomeric energy they compared transition lines (or cascades of lines) which are emitted from levels which populate both, the ground state and the isomeric state. A partial level scheme is shown in Fig. 1.5, where the different schemes together with the relevant transition lines are shown.

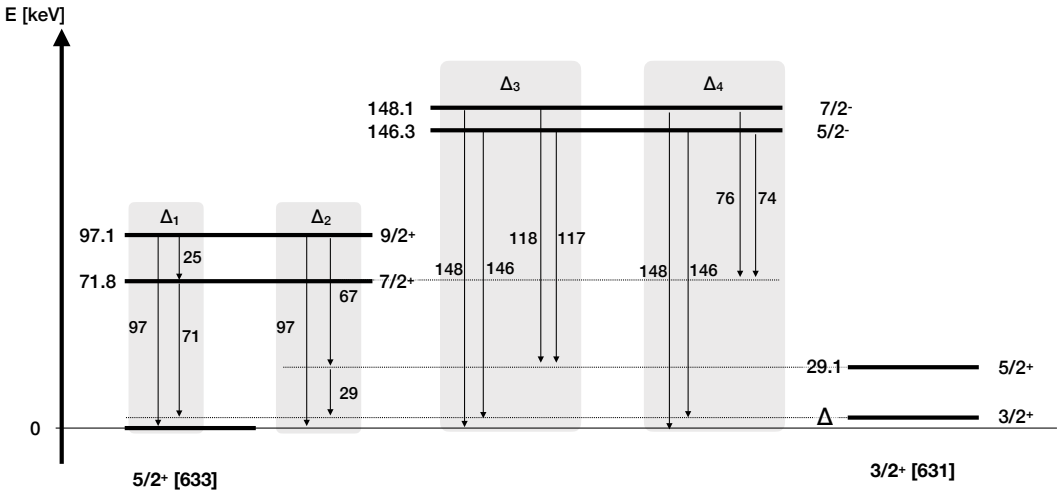

Figure 1.5: Partial level scheme of ^{229}Th. The different schemes used for an indirect energy determination of the energy (Δ) of the first isomeric state in ^{229}Th are indicated (cf. [24] and [25]). Details are given in the text.

They reported three different schemes that were used for the measurement:

$$\begin{aligned}
\Delta_1 &= E(97) - [E(25) + E(71)] &&= -3 \pm 5 \text{ eV} \\
\Delta_2 &= E(97) - [E(67) + E(29)] &&= -1 \pm 6 \text{ eV} \\
\Delta_3 &= [E(148) - E(146)] - [E(118) - E(117)] &&= 2 \pm 8 \text{ eV}.
\end{aligned}$$

The weighted average of the results shown above led to a value for the isomeric excitation energy of $\Delta = -1 \pm 4$ eV and the authors conclude that the energy is „in any event [..] almost certainly less than 10 eV“[24]. The energy resolution of their germanium detectors was between 450 and 610 eV (full width at half maximum) at 29 keV and 146 keV, respectively.
In 1994 Helmer and Reich presented an improved energy determination of ^{229m}Th [25]. This new measurement benefitted from a multitude of improvements involving a higher energy resolution (down to 270 eV at 29 keV), the use of five different detector types and more calibration lines. In addition to the measurements performed in 1990, the authors used not only three but four difference schemes to obtain a value for the isomeric energy. The additional scheme is shown in Fig. 1.5 and labelled with Δ_4.

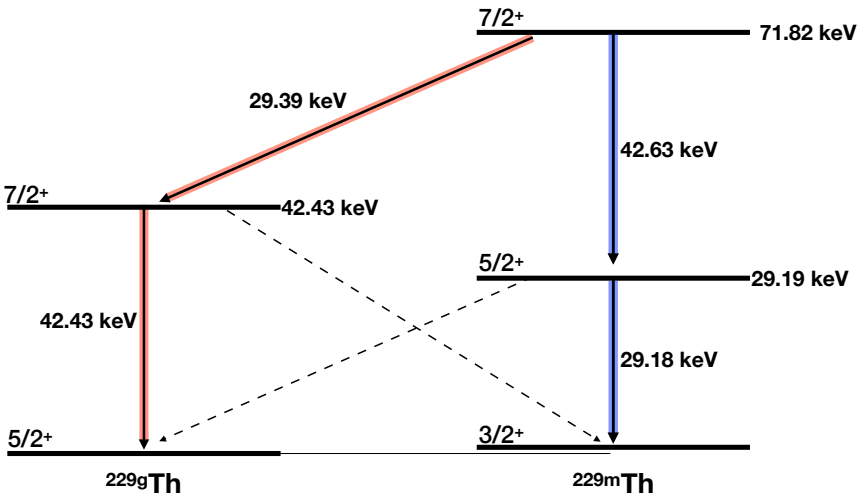

Figure 1.6: Level scheme of the four lowest excited states in ^{229}Th. The cascade that is feeding the ground-state (isomeric state) is highlighted in red (blue). Dashed lines indicate interband transitions of the lowest members of the two rotational bands (based on the ground state and the isomeric state), to the other respective band head. The energy difference between the cascade feeding the ground state (red) and the cascade feeding the isomeric first excited state was used in [30] and [31] to extract the excitation energy of the latter. For details see text.

A final value of 3.5±1.0 eV was concluded. These measurements were the first ones to exclude the energy for the first isomeric state to be equal to zero. The energy corresponds to a wavelength of 350 $^{+150}_{-75}$ nm and puts the energy in a region accessible with lasers in the UV range.

In the following years research was conducted that was aiming on the detection of a 3.5 eV photon emitted from the nuclear deexcitation. In 1997 [26] and 1998 [27] the observation of photons in the energy region around 3.5 eV emitted from ^{233}U samples in air was reported. It was assumed that the signals resulted from the isomeric decay in ^{229}Th. Later the observed signals were proven to result from N_2 discharge induced by α particles in collisions with the air surrounding the samples [28, 29].

In 2005 the data from [25], which led to the value of 3.5 eV, were re-examined by using updated branching ratios of the γ transitions. This re-analysis led to a slightly larger value of 5.5±1.0 eV[32].

Unexpectedly, in 2007 a paradigm shift occurred, when the use of improved detector technology allowed for employing a new differencing scheme that enabled measuring the isomer's energy with 7.6±0.5 eV [30]. In these measurements X-ray microcalorimeters developed for space applications were used that reached an energy resolution of ≈ 26 eV [30]. The differencing scheme that was employed in these measurements is shown in Fig. 1.6. In this scheme the $7/2^+$ state at 71.82 keV is used. This state decays to the ground state (red path in Fig. 1.6) and to the isomeric first excited state. This decay occurs in a cascade with two emitted γ rays per path: 29.39 keV (inter-band transition) and 42.43 keV γ rays for the decay to the ground state and 42.63 keV and 29.18 keV γ rays for the decay to the isomeric state. Thus, the energy of the isomer can be deduced from:

$$E_I = [\mathrm{E}(29.39) + \mathrm{E}(42.43)] - [\mathrm{E}(42.63) + \mathrm{E}(29.18)]. \tag{1.1}$$

An advantage of this approach is that the emitted γ rays form two pairs in the same energy region, only separated by about 200 eV. This makes this approach less sensitive to non-linearities of the spectrometer.
A precise analysis of the γ decay pathways has to take into account also the inter-band decay branches between the lowest excited members of the two rotational bands and the band heads of the other band, respectively (indicated by the dashed lines in Fig. 1.6). First, there is a non-zero branching ratio from the 29.19 keV state to the ground state. This leads to a splitting of the 29.18 keV line, however, the detector energy resolution was not sufficient to resolve it. Therefore, the measured 29.18 keV line is the superposition of two transitions: ($E_{29\to is.}$) and ($E_{29\to g.s.}$). This means that the centroid of the measured line needs to be corrected for the admixture by subtracting a correction term $b_{29} \cdot E_I$ (where b_{29} is the branching ratio) from the measured transition energy. Altogether this leads to the following expression for the isomeric energy:

$$E_I = \frac{1}{1 - b_{29}} \Big(\big[\mathrm{E}(42.43) - \mathrm{E}(42.63)\big] + \big[\mathrm{E}(29.39) - \mathrm{E}(29.18)\big] \Big). \tag{1.2}$$

The branching ratio b is predicted by scaling the branching ratio from the interband transition 71.81 keV → 42.43 keV compared to the intraband transition 71.81 keV → 29.19 keV. b_{29} was predicted to be 1/13 with an 8% error (which is not included in the error budget of [30]). Based on these findings the value 7.6±0.5 eV was deduced for the isomeric energy.

In 2009, the interband transition from the 42.43 keV ($7/2^+$) state to the isomer was taken into account in the same manner as the 29 keV interband transition described above. This shifted the energy to 7.8±0.5 eV [31]. A recent measurement of the branching ratio b_{29} via synchrotron radiation revealed a modified value of $b_{29} = 1/(9.4\pm2.4)$ [20]. Plugging this new value in the above described analysis of the Livermore data results in the following updated value for the energy of the isomer

$$E_I = 8.0 \pm 0.5_{\text{stat.}}\ ^{+0.4}_{-0.2}\ \text{eV}, \tag{1.3}$$

where the asymmetric uncertainty results from the uncertainty in the branching ratio.

1.3 Direct detection of ^{229m}Th

Despite several experimental efforts, the direct detection of the ground-state decay of the thorium isomer kept pending until 2016, when the first successful direct detection was achieved by measuring internal conversion electrons [4].
These measurements were conducted with the experimental setup that is described in chapter 3 and also forms the basis for the measurements performed in this thesis. The isomer is populated in the 2% decay branch of the α decay of ^{233}U that ends in the thorium isomer. $^{229(m)}$Th recoil ions[2] are stopped in buffer gas, are guided to an extraction nozzle and injected into a segmented RF-quadrupole which forms a phase-space cooled ion beam. The $^{229(m)}$Th ion beam is purified from accompanying daughter nuclei from the ^{233}U decay chain. The mass-purified ion beam is then collected on the CsI-coated surface of a microchannel plate (MCP) detector in soft-landing (*i.e.* with a low kinetic energy). The MCP detector serves two purposes: First, ^{229m}Th ions are neutralized as they are collected on the surface of the detector. This enables the isomer to decay via internal conversion. Second, the emitted IC electrons are multiplied by and detected with the MCP detector.
In a series of comparative and exclusion measurements it could be shown that the measured signal must unambiguously result from the ground-state decay of ^{229m}Th. By storing the ions for a defined time in a linear Paul-trap before guiding them onto the MCP detector, it is possible to estimate the lifetime of ^{229m}Th in an ionic charge state. It was found that the lifetime of the isomer in doubly and triply charged ^{229m}Th$^{2+,3+}$ ions is longer than 60 s. This lower limit emerges from the limited storage time of the ^{229m}Th$^{2+,3+}$ ions in the Paul trap due to the vacuum quality. Additionally, it was found that the lifetime following the IC decay is shorter than 1 s. Although the purpose of this experiment was not an energy determination, it still allowed to set upper and lower bounds on the isomeric excitation energy. Due to the long isomeric lifetime in the 2+ charge state it could be concluded that the energy of the isomer is below the third ionization potential of thorium of 18.3 eV (IP($2+ \rightarrow 3+$) = 18.3 eV [33]). In turn, the short lifetime observed for ^{229m}Th ions collected on the CsI surface indicates that the energy lies above the work-function of CsI, given with 6.3 eV. It has been argued, however, that the presence of Th on the CsI surface may lead to a reduction of the work function to only 2.2 eV[34], which should instead be taken as the lower bound for the excitation energy of the thorium isomer.

[2]) $^{229(m)}$Th is used as a notation to express the fact that only a fraction of the ions (2%) are in the isomeric state ^{229m}Th.

1.4 Frequency standards

In general, clocks require two ingredients: a frequency standard, providing a stable and well defined frequency (ν), and a clockwork or counter, that counts the cycles of the frequency. The frequency standard can be active (providing oscillations itself) or passive (being probed by an oscillator). One example for a clock is the rotation of the earth (with $\nu \approx 1/24h \approx 12$ μHz) or a pendulum clock (with $\nu \approx 1$ Hz), where a mechanical clockwork counts the oscillations of a pendulum. A practical problem of these clocks is that the underlying frequency standards are not stable (earth's rotation, for example, is slowed down by the moon) or not universal (the frequency of the pendulum depends on the gravitational acceleration). Already in the late 19$^{\text{th}}$ century the use of atoms as natural standards was suggested by Thomson (Lord Kelvin) and Tait [35]. The advantage of using atoms is that all atoms of a given species are alike and should therefore provide a universal and easily reproducible standard. In the 1940s, first clocks based on atomic transitions were developed. In atomic clocks a transition in the electronic shell serves as a passive frequency standard that is resonantly excited with radiation whose frequency is measured. These clocks reach a relative frequency uncertainty below $\Delta\nu/\nu \approx 10^{-15}$ [36, 37]. Since 1967 the SI second is defined as „9 192 631 770 periods of the radiation corresponding to the transition between the two hyperfine levels of the ground state of the caesium 133 atom“ [38]. The frequency of this radiation (≈9.2 GHz) lies in the microwave region.
For clocks it is advantageous to go to even higher frequencies [39]: First, the quality factor (defined as $Q = \nu/\Delta\nu$, with $\Delta\nu$ as the (FWHM) width of the clock's transition lineshape) that determines the stability of the oscillator is proportional to the frequency. Second, with a higher frequency, relative frequency uncertainties can be detected much faster[3]. Until the late 1990s the measurement (*i.e.* the counting) of optical frequencies (in the THz = 10^{15} Hz regime) required the use of large frequency divider chains. With the advent of the optical frequency comb [40–42] it was possible to relate optical frequencies to easy-to-measure microwave frequencies. This directly paved the way for optical atomic clocks.
The accuracy of atomic clocks (in the optical as well as in the microwave regime) is affected by external perturbations which shift and broaden the transition frequency [3]. The temperature dependent velocity distribution of the ions or atoms leads to Doppler broadening of the transition frequency. Laser cooling techniques allow to cool down the temperature of the atomic sample in order to reduce these Doppler shifts. Moreover, in ion traps the stored ions are subject to AC and

[3]To detect a clock instability at a level of 10^{15} requires 10^{15} s for a 1 Hz oscillator, but only 10^{-15} s measurement time for a 10^{15} Hz oscillator [39].

DC electric fields, which cause excess micromotion of the ion that cannot be completely removed by laser cooling, but can be compensated by a proper trap design [43, 44]. Electric and magnetic fields (from stray fields, trapping fields or trapping lasers or black-body radiation) also introduce Stark and Zeeman shifts. A detailed description of the induced shifts can be found in Ref. [3]. By preparing the ion or the atom in a specific state and employing a suitable clock transition it is possible to minimize some of these shifts. The resulting frequency shift can be evaluated by a precise knowledge of the environmental conditions (like temperature, electric and magnetic fields, ion/atom motion, etc.). The resulting uncertainty of these frequency shifts then defines the systematic uncertainty of the optical clock under consideration. Today's most precise clock, an Al^+ quantum-logic clock, reaches a systematic frequency uncertainty of 9.5×10^{-19} [44]. The limiting factors for this clock are connected to excess micromotion, black-body radiation and quadratic Zeeman effect.

1.4.1 A nuclear frequency standard with ^{229m}Th

In 2003 Peik and Tamm proposed to use the ground-state transition of the isomeric state in ^{229}Th as a frequency standard [45]. As the nucleus is orders of magnitude smaller than the electronic shell, this also holds for the nuclear electric and magnetic moments. Since the frequency shifts related to electric and magnetic fields described above are proportional to the electric and magnetic moments, a nuclear optical clock should be less perturbed by external fields than an atomic optical clock.
Campbell et al. [46] performed a detailed analysis of effects that can be expected in a single-ion nuclear clock. In this case, the uncertainty from the black-body radiation shift, for example, is reduced to the 10^{-22} level. Summing up all the uncertainties, a single-ion nuclear optical clock could reach a systematic frequency uncertainty of 1.5×10^{-19}. The strongest contribution originates from excess micromotion of the ion in the trap and gravitational shifts. For the latter, a height difference experienced by the clock of 1 mm will result in a relative frequency shift of about $\Delta\nu_{\mathrm{grav}}/\nu \approx 10^{-19}$ ($\Delta\nu_{\mathrm{grav}}/\nu = g\Delta h/c^2 \approx \Delta h[\mathrm{m}] \times 10^{-16}$).

An alternative approach to realize a nuclear clock, instead of storing^{229}Th ions in an ion trap, is to embed many ^{229}Th nuclei in a VUV transparent crystal to operate a solid state nuclear optical clock. If ^{229}Th forms ionic bonds and occupies lattice sites in the host crystal, it could be possible to suppress non-radiative decay channels. This allows to probe the nuclear transition frequency in a solid crystal environment and represents an elegant novel approach for an optical clock. Such

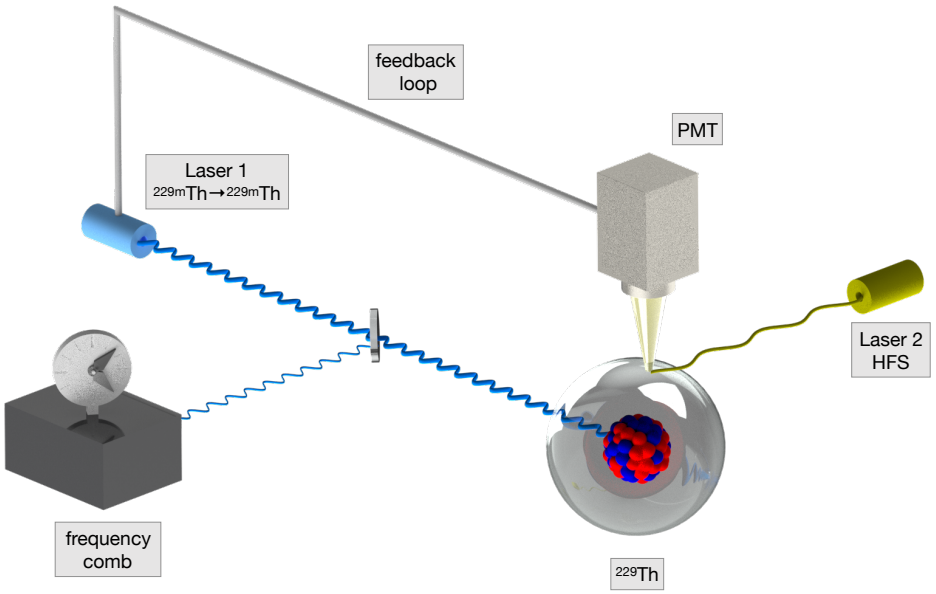

Figure 1.7: Possible realization of a nuclear optical clock based on $^{229\mathrm{m}}$Th. Laser 1 excites the nuclear transition. The nuclear state is probed with Laser 2 via the resulting hyperfine-structure (HFS) shift in the electronic shell [17]. The transition frequency is measured with a frequency comb.

a clock benefits from the large number of oscillators (10^{15} per cm^3) which can be interrogated at the same time. Kazakov et al. [47] as well as Rellergert et al. [48] thoroughly investigated the resulting possible clock frequency shifts and their uncertainties. It is found, that there are large shifts of the transition frequency due to molecular binding which are constant in time. As long as every ^{229}Th ion occupies the same lattice site and experiences the same lattice environment, the relative frequency uncertainty would mostly be influenced by temperature variations across the crystal: The nuclear transition frequency is influenced by its electronic environment, for example by electric monopole interaction with the electron cloud surrounding the nucleus. The electron density on the crystal lattice sites depends on the temperature which therefore directly influences the transition frequency. This leads to relative shifts and broadening with $5{\times}10^{-12}$ 1/K. Rellergert et al. conclude a long-term frequency accuracy of $\Delta\nu/\nu = 2 \times 10^{-16}$ and a short term resolution of $\Delta\nu/\nu = 2 \times 10^{-18}$ [48].
The challenge in this approach is the ultimate purity of the crystal which is needed in order to make the fluorescence of the isomeric decay (if the isomer has been excited by laser radiation) detectable. As it will be shown in chapter 5, the lifetime of the internal conversion decay channel strongly depends on the electronic environment of the nucleus and it can be assumed that every non-radiative decay channel, such as internal conversion, will be faster than the radiative decay ($\tau \approx 10^4$ s). Moreover, it can be shown as well that the isomeric lifetime can be influenced and eventually even be prolonged. If one could extend the internal conversion lifetime to a value such that the resulting linewidth would not limit the clock performance, one could even use internal conversion electrons (instead of fluorescence photon detection) in a solid-state clock. A possible experimental approach to measure internal conversion inside a solid-state environment is proposed in section 7.2.2.

1.4.2 Potential applications

Precision laser spectroscopy of the first excited state in ^{229m}Th can be exploited for a variety of applications such as satellite based navigation [49–51], geodesy [52, 53] or dark-matter research [54, 55]. A detailed overview can be found in [56]. In the following the sensitivity of ^{229m}Th to variations of fundamental constants will be detailed further.

^{229m}Th and variation of α

Many theories that aim at unifying gravity with other fundamental forces suggest temporal variations of fundamental constants in an expanding universe [57, 58]. Observations of optical spectra from distant quasars hint on an evolution of the fine-structure constant throughout the history of the universe [59] are controversially discussed [58]. Temporal variation of α was already put to test with optical atomic clocks yielding a value of $\dot{\alpha}/\alpha = (-0.7 \pm 2.1) \times 10^{-17}$ per year [60].
It was predicted that a nuclear optical clock based on ^{229m}Th can provide an enhanced sensitivity to the variation of the fine structure constant α [61, 62] (and the scale parameter of the strong interaction m_q/Λ_{QCD} [63]). In general, the energy difference between two (excited) states in a nucleus is the result of several different energy differences, where only the Coulomb-term is of interest for variations in α. Using the Hellmann-Feynman theorem, the sensitivity of the transition frequency on variations in α is given by $\delta\nu = \frac{\Delta V_C}{h}\frac{\delta\alpha}{\alpha}$ (as outlined in [61] and [62]). Alternatively, one finds $\delta\nu/\nu = \frac{\Delta V_C}{h\nu}\frac{\delta\alpha}{\alpha} = \frac{\Delta V_C}{\hbar\omega}\frac{\delta\alpha}{\alpha} = K\frac{\delta\alpha}{\alpha}$. Where $K = \frac{\Delta V_C}{\hbar\omega}$ is an enhancement factor. In case of a nuclear clock K can be derived as the ratio between the Coulomb energy difference and the energy of the respective clock transition. For nuclei, the difference of the Coulomb energy ΔV_C is typically in the range of keV to MeV. This means that the sensitivity to $\dot{\alpha}$ could be enhanced by several orders of magnitude in nuclear transitions compared to atomic transitions. The exact value of the Coulomb energy difference ΔV_C of the ground and first excited state in ^{229}Th can currently not be extracted from nuclear structure calculations. It is possible to deduce ΔV_C from measured data, such as the electrical quadrupole moment and the difference of the mean square charge radii of the ground and first excited state in ^{229}Th [64]. This motivated collinear laser spectroscopy studies, which were performed in a collaborative campaign led by a group from PTB, resulting in experimental values of the nuclear moments and charge radius for the ^{229}Th isomer. Despite reaching a precision of only 4% for the quadrupole moment, the similarity of the properties of the ground and isomeric state resulted in a value of $\Delta V_C = -0.29 \pm 0.43$ MeV[17], which is

still inconclusive with regard to a quantification of the enhancement factor K. Nevertheless, it leaves the possibility that $^{229\mathrm{m}}$Th will enhance the experimental sensitivity to temporal changes of fundamental constants by orders of magnitude.

1.5 Current experimental research on ^{229m}Th

In the following, an overview of experimental approaches either proposed or currently being pursued to excite the thorium isomer and to measure its energy or lifetime will be presented.

Microcalorimetric energy measurements of ^{229m}Th

First evidence for an isomeric state in ^{229}Th was already found while investigating the γ radiation that follows the α decay of ^{233}U [21] (for a detailed description see section 1.2). Additionally, the (until recently) accepted energy value of 7.8±0.5 eV also resulted from an indirect measurement. The precision of this result was limited by the detector resolution (≈26 eV) and an insufficient knowledge of the intra-band branching ratios. The use of metallic magnetic calorimeters (MMCs) [65, 66] developed at the University of Heidelberg, may overcome both problems and raise this technique to the next level. This type of detector reaches an energy resolution of only a few eV (at an energy of several keV) and therefore potentially allows to resolve the doublet of the 29 keV line (see Fig. 1.5) which populates both the ground-state and the isomeric state [67]. This makes the indirect measurement independent from branching ratios and may lead to a precision of 0.12 eV (0.04 eV) under the assumption of an instrumental energy resolution of 6 eV (3 eV) [67].

Energy determination with SNSPDs

Another novel approach to measure the isomer's energy is to employ **s**uperconducting **n**anowire **s**ingle **p**hoton **d**etectors (SNSPDs) [68]. In these detectors a current is sent through a (meander-shaped) superconducting nanowire. The superconductivity is broken when a certain amount of energy is deposited (by impinging photons, ions or electrons) and heats the wire. As soon as the superconductivity is broken, one can measure a voltage across the wire. The amount of energy that is needed to break the superconductivity depends on the applied current. This allows to determine the deposited energy by sweeping the applied current. There are two ideas how to employ SNSPDs for an energy determination of ^{229m}Th. The first one implants $^{229(m)}$Th nuclei from the ^{233}U α decay directly on the nanowire. The second approach implants $^{229(m)}$Th ions extracted from a buffer gas stopping cell with low kinetic energy on the nanowire. In both cases, the isomer will decay directly on the nanowire and the released energy (be it by internal conversion or γ decay) is deposited in the wire.

^{229m}Th in a VUV-transparent host crystal

Several groups worldwide search for γ rays emitted from the isomeric decay of $^{229(m)}$Th embedded in a VUV transparent host crystal (CaF_2, MgF_2 or LiSrF). If ^{229}Th undergoes an ionic bond in the crystal (placing it as $^{229}Th^{4+}$ on a lattice site), it is possible to suppress the internal conversion decay channel. Three approaches are followed to populate the nuclear isomer: one is to populate the isomer via the 2% decay branch in the α decay of ^{233}U. In this approach CaF_2, for example, is doped with ^{233}U. The other approach aims on a direct excitation of ^{229m}Th in the crystal. Here ^{229}Th doped crystals are employed. The goal is then to excite ^{229m}Th with VUV lasers, VUV lamps or synchrotron sources [69–71]. These measurements remained inconclusive so far.
Only recently, the second excited nuclear state in ^{229}Th has been successfully excited with resonant synchrotron radiation at the SPring8 facility in Japan [20]. This allows to populate the isomeric state in a Lambda scheme, since the second excited state predominantly decays to the isomeric state.
Alternatively, it is also possible to populate the isomer in the β decay of ^{229}Ac. For this reason, ^{229}Ac ions were implanted in CaF_2 crystal in a recent feasibility study performed at the ISOLDE facility at CERN [19]. This scenario has several advantages compared to ^{233}U doped crystals. First, in the β decay almost no recoil energy is transferred to the $^{229(m)}$Th ions, so that they securely remain on their lattice site. Additionally, ^{229}Ac feeds the isomeric state in ^{229}Th with a rather large branching ratio of >14 % in its radioactive decay.

Direct excitation of ^{229m}Th in a Paul trap

In yet another approach, ^{229}Th ions are stored in a Paul trap to excite the isomer via an electronic-bridge process. For this purpose a suitable electronic state needs to be excited in a ^{229}Th ion. During its decay, energy is transferred to the nucleus and excites the isomer. A thorough scan search with $^{229}Th^{1+}$ ions has been conducted by a group at PTB Braunschweig [72], where currently $^{229}Th^{2+}$ ions are investigated [73].

Direct excitation of ^{229m}Th on a solid surface

The lifetime of ^{229}Th on a solid surface, which is known to be in the range of microseconds (see chapter 5 and [11]), can be exploited to excite ^{229m}Th on a surface. In this approach [74] a solid sample of ^{229}Th is irradiated with a pulsed tunable VUV laser [75, 76]. The laser pulse length (and most importantly the falling edge of the laser pulse) is much shorter than the lifetime of the isomer on the surface. If the laser is in resonance with the nuclear transition energy, the iso-

mer is excited. In this case conversion electrons are emitted in subsequent decay via internal conversion and can be easily detected. This allows to determine the isomeric energy with a precision in the region of the laser linewidth (assuming a typical laser linewidth of 10 GHz, corresponding to ≈40 μeV).
It should be noted that such an experiment can already be performed with presently existing laser technology, without the need of an improved precision of the isomeric excitation energy. Thus, a proof-of-principle experiment for an optical nuclear excitation could be performed as an intermediate step towards the ultimately targeted optical excitation with a customized laser system and a linewidth in the Hz range.

Internal conversion electron spectroscopy

Instead of directly exciting the nucleus or measuring the γ radiation, another approach employs the internal conversion decay channel. In this decay channel the energy of the isomer is transferred to the electronic shell and ionizes the atom. The kinetic energy of the emitted electron is then correlated to the isomeric energy. Therefore, the precise measurement of the conversion electron's kinetic energy allows to deduce the isomeric energy [77, 78]. This approach forms the basis of the main part of this thesis, paving the road towards a first direct and improved determination of the thorium isomer's excitation energy (see chapter 6).

CHAPTER 2

Theoretical Background

This chapter provides the physical background that is needed to properly understand the motivation of the thesis. In the first part, different nuclear structure models are introduced that are used to describe ^{229}Th. The second and third section of this chapter provide a description of the decay channels of ^{229m}Th. This prepares the theoretical background for the lifetime and energy measurements presented in this thesis. The interaction of charged particles with solids is shortly outlined in sect. 2.4 In the last section of this chapter, the behaviour of charged particles in electromagnetic fields is outlined, which is needed to understand the magnetic-bottle spectrometer that is detailed in sect. 3.2 and employed for the energy determination of ^{229m}Th.

2.1 Nuclear structure of ^{229}Th

The structure of nuclei is governed by the fine interplay between several forces, such as for example electromagnetic forces between the protons or strong forces between the nucleons. There are many models that describe the structure of nuclei. Ranging from the early liquid drop model to nuclear shell models, nuclear structure theory was constantly refined to provide an adequate description of nuclear properties. In the following, both of these models are outlined to motivate the Nilsson model, which can be used to describe the properties of deformed nuclei such as ^{229}Th.

The macroscopic liquid drop model assumes that nuclei behave as incompressible drops of liquid matter. The volume of such a drop is assumed to be proportional to the total number of nucleons A (with $A = N + Z$, with N as the number of neutrons and Z the number of protons), consequently, the radius of the drop is

proportional to $A^{1/3}$. The underlying assumption is a uniform distribution of the nucleons in the phase-space. This gave rise to a first semi-empirical formula: the Bethe-Weizsäcker mass formula [79] that first allowed to calculate the binding energy of nuclei. In the formula, the binding energy (E_B) is the sum of five different terms (following Ref. 80):

$$E_B = b_{\mathrm{vol}}A + b_{\mathrm{surf}}A^{2/3} - \frac{1}{2}b_{\mathrm{sym}}\frac{N-Z}{A} - b_C\frac{Z^2}{A^{1/3}} + \delta(A). \tag{2.1}$$

The terms include: the nearest-neighbour interaction of the nucleons, represented by the volume term (proportional to A) and a surface term (proportional to $A^{2/3}$), the Pauli principle (symmetry term), Coulomb interaction of the protons (Coulomb term) and additionally a pairing term ($\delta(A)$) is added that introduces observed differences in binding energies of even-odd, odd-odd or even-even nuclei. The corresponding constants, b_{vol}, b_{surf}, b_{sym} and b_{C} are determined by experiment.

Nuclear Shell Model

The liquid drop model gives a good description for the bulk properties of nuclear matter, like the mass, size of nuclei and nucleon binding energies. It lacks, however, the ability to explain other properties that are found in nuclei, such as the appearance of magic numbers (2, 8, 20, 28, 50, 82,..): when comparing the stability of isotones or isotopes, one finds that for neutron or proton numbers equal to magic numbers, these nuclei are more strongly bound than others. Additionally, the nucleon separation energy increases up to the same neutron or proton numbers and shows a sharp decrease when the neutron or proton number lies just beyond a magic number.
This behaviour is reminiscent of the electronic shell structure of atoms, which results from an interplay of the Pauli principle and the electrons' confinement in a common potential.
In order to construct a model in which the observed nuclear shell structure manifests itself, one needs to find a common potential that confines the nucleons. Infinite square well potentials as well as harmonic potentials already result in the formation of the first magic numbers (2, 8 and 20). In order, to explain all magic numbers, however, it is required to use a refined potential and to include the spin-orbit coupling (however with inverse sign compared to atomic physics). Electron scattering [81] or nucleon scattering [82] experiments that investigate nuclear form factors suggest that the nucleons are confined in a Woods-Saxon type potential

$$V_{\mathrm{W.S.}}(r) = \frac{V_0}{1+\exp\left((r-R)/a\right)}, \tag{2.2}$$

where R is connected to the spatial extent of the nucleus and a defines the sharpness of the potential. The correct sequence of the magic numbers can be reproduced by a Hamiltonian of the form

$$\mathcal{H} = -\frac{\hbar^2}{2M_N}\Delta + V_{\text{W.S.}}(r) + \nu(\hat{l}\cdot\hat{s}). \tag{2.3}$$

Here M_N is the mass of the nucleus, Δ is the Laplace operator (equivalent to the momentum operator $\frac{\hat{p}^2}{2M_N} = -\frac{\hbar^2}{2M_N}\Delta$), $V_{\text{W.S.}}(r)$ is the Woods-Saxon potential given above and $\nu(\hat{l}\cdot\hat{s})$ describes the coupling of the nucleon spin (connected to $\hat{s}$) with its orbital angular momentum (connected to $\hat{l}$). The above Hamiltonian is given here as an illustrative example which allows to successfully predict the magic numbers. It should be pointed out, that there are many models and possibilities to predict and describe nuclear properties. As will be shown in the following, also (deformed) harmonic oscillator potentials provide the magic numbers and do even allow to predict further nuclear properties.

Nilsson Model

The nuclear shell model in its simplified form described above fails for a quantitative description of the level structure in deformed nuclei. The reason is, that the above given Woods-Saxon potential that is confining the nucleons still contains spherical symmetry. The goal, however, is to apply the nuclear shell model also to deformed nuclei and to calculate the resulting level energies in dependence of the shape (*i.e.* the deformation) of the nucleus. To apply the nuclear shell model to deformed nuclei, the following Hamiltonian with an anisotropic potential was introduced by Nilsson [83]:

$$\mathcal{H} = -\frac{\hbar^2}{2M_N}\Delta + \frac{M_N}{2}\omega_\perp^2(x^2+y^2) + \frac{M_N}{2}\omega_z^2 z^2 + C(\hat{l}\cdot\hat{s}) + D\hat{l}^2, \tag{2.4}$$

where C is a constant that defines the strength of the spin-orbit coupling. The orbital angular momentum $\hat{l}^2$ (proportional to a constant D) is included to flatten the harmonic oscillator potential in order to give it a more realistic (Woods-Saxon type) shape. The anisotropic potential of the Hamiltonian is comprised of a harmonic oscillator potential with eigenfrequencies ω_z (along the symmetry axis) and $\omega_\perp$ (perpendicular to the symmetry axis). As the eigenfrequencies are correlated with the spatial extent of the potential, these are related to the dimensions and thus the deformation of the nucleus. For the harmonic oscillator the following energy eigenvalues can be found:

$$E_{n_x,n_y,n_z} = \hbar\omega_\perp(n_x+1/2) + \hbar\omega_\perp(n_y+1/2) + \hbar\omega_z(n_z+1/2), \tag{2.5}$$

where $n_{x,y,z}$ are the principle quantum numbers of the harmonic oscillator potentials. The energy eigenstates of the above Hamiltonian can be described by a set of quantum numbers

$$\Omega^{\pi}\ [N\ n_z\ \Lambda], \tag{2.6}$$

where Ω is the projection of the total angular momentum $(\vec{\Lambda} + \vec{s})$ of the valence nucleon on the symmetry axis of the nucleus. N denotes the principle quantum number ($N = n_x + n_y + n_z$), n_z is the principle quantum number of the harmonic oscillator potential along the symmetry axis and Λ is the projection of the angular momentum of the valence nucleon $\vec{\Lambda}$ on the symmetry axis. The goal is to calculate energy levels as a function of the nuclear deformation. The deformation of spheroids is usually parametrized with the deformation parameter δ:

$$\delta = 2\frac{b-a}{b+a}, \tag{2.7}$$

where b is the length of the rotational ellipsoid along the symmetry axis and a denotes the extent along the axis perpendicular to the symmetry axis. From the incompressibility of nuclear matter it follows that the volume of the spheroid ($V \propto b * a^2$) is constant. Consequently, as the harmonic oscillator potential introduced above defines the mean field of the nucleus which is connected to its spatial extent, it follows that $\omega_x\omega_y\omega_z = \omega_\perp^2\omega_z = \omega_0^3 = const.$. These relations then allow to calculate a deformation dependent eigenenergy of the Hamiltonian.

Nilsson Model and ^{229m}Th

For deformed nuclei, rotations perpendicular to the symmetry axis can occur. In case of axial and reflection symmetry, the rotational energy of the nucleus is given as

$$E_{\text{rot}} = \frac{\hbar}{2\theta_\perp} I(I+1), \tag{2.8}$$

where $\theta_\perp$ is a measure for the moment of inertia of the nucleus (strongly connected to its shape) and I is the total angular momentum of the rotation. Series of rotational states with common $\theta_\perp$ are called rotational bands and the lowest energy state of each rotational band is its band head.
The ground- and first excited isomeric state in ^{229}Th are characterized as two rotational band-heads with the Nilsson numbers

Ground State:	$5/2^+[633]$
Isomeric State:	$3/2^+[631]$.

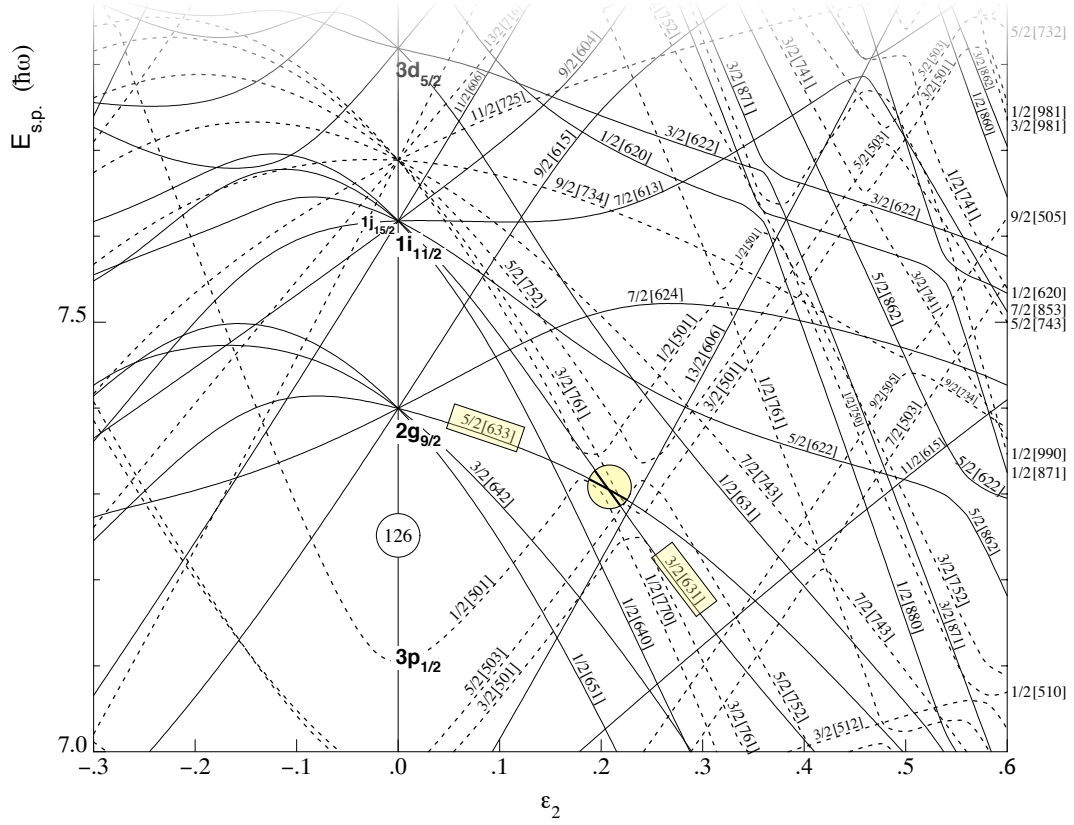

Figure 2.1: Single-particle Nilsson orbitals taken from Ref. [84]. The crossing of the 5/2[633] (ground) and 3/2[631] isomeric state is shown and highlighted in yellow. The x-axis represents the deformation given by $\epsilon_2 = \delta + \frac{1}{6}\delta^2 + \frac{5}{18}\delta^3 + ...$

The crossing of the two Nilsson states (representing the near degeneracy of the two orbitals) is shown in Fig. 2.1 at $\epsilon_2 \approx 0.2$, which corresponds to a prolate deformation of the ^{229}Th nucleus.

2.1.1 Recent nuclear structure calculations

Although the Nilsson model provides already a reasonable description of basic nuclear properties, it cannot explain the low energy isomer found in ^{229}Th. Additionally, it fails to quantitatively describe the magnetic dipole moment of $^{229\mathrm{m}}$Th [7, 17, 85]. A recent nuclear structure model specifically addressing ^{229}Th includes the collective motion of the nucleus (*i.e.* its quadrupole-octupole coupling), single particle motion of the unpaired nucleon and the Coriolis interaction (*i.e.* the

interaction of the angular momentum of the unpaired nucleon with the even-even core angular momentum) [6]. Applying this model to the low-energy spectrum of ^{229}Th allows to refine the model parameters and to calculate the (still not yet measured) reduced electric quadrupole and magnetic dipole transition probabilities $B(E2)$ and $B(M1)$, respectively, which can be used to predict the lifetime of the isomeric state in ^{229}Th (see next section). Additionally, this model allows to predict the magnetic dipole moment of $^{229\mathrm{m}}$Th to -0.35 μ_N [7]. This is in good agreement with the measured value of -0.37 ± 0.06 μ_N [17] (where μ_N is the nuclear magneton) and creates further confidence that this model allows to adequately describe ^{229}Th.

2.2 Nuclear electromagnetic transitions

The interaction of nuclei with electromagnetic fields allows them to decay (or to be excited) from an initial state $|I_i, m_i\rangle$ to a final state $|I_f, m_f\rangle$. In the following section the underlying physical mechanisms are shortly described, following closely Ref. [80]. The ground-state decay of $^{229\mathrm{m}}$Th will be described at the end of this section.
Consider a nucleus that is described by nuclear charge and current densities $\rho(\mathbf{r})$ and $\mathbf{j}(\mathbf{r})$, respectively. This nucleus can interact with an electromagnetic field represented by the electric scalar potential $\phi(\mathbf{r}, t)$ and the electromagnetic vector potential $\mathbf{A}(\mathbf{r}, t)$ (such that $\mathbf{B}(\mathbf{r}, t) = \nabla \times \mathbf{A}(\mathbf{r}, t)$). The interaction between the nucleus and the field can be described by the Hamiltonian

$$H_{\mathrm{int}} = \int \rho(\mathbf{r})\phi(\mathbf{r}, t) - \frac{1}{c}\mathbf{j}(\mathbf{r})\mathbf{A}(\mathbf{r}, t) \quad d\mathbf{r}. \tag{2.9}$$

It is possible to calculate the transition probability from an initial nuclear state $|i\rangle$ to a final nuclear state $|f\rangle$ by using Fermi's Golden Rule:

$$\Gamma = \frac{2\pi}{\hbar} \left|\langle I_f, m_f \,|\, H_{\mathrm{int}} \,|\, I_i, m_i\rangle\right|^2 D(E_f). \tag{2.10}$$

Here $D(E_f)$ is the density of final states. Following Ref. [80] (p. 205) and expanding $\mathbf{A}$ in multipoles (with multipolarity L), the rate can be expressed as

$$\Gamma(\lambda, kL\sigma) = \frac{8\pi(L+1)}{\hbar L[(2L+1)!!]^2}\left(\frac{E_\gamma}{\hbar c}\right)^{2L+1} \left|\langle I_f, m_f \,|\, \mathcal{M}(\lambda, kL\sigma) \,|\, I_i, m_i\rangle\right|^2. \tag{2.11}$$

Here $\mathcal{M}(\lambda, kL\sigma)$ denotes the multipole transition operator, with λ referring to the type of transition (electric E or magnetic M), k being the wave vector ($k = E_\gamma/(\hbar c)$) and σ being the orientation (polarization) of the electromagnetic wave. In the long wavelength approximation (which is valid for $E_\gamma R \ll \hbar c$ with R being the nuclear radius) the multipole operator can be expressed as

$$\mathcal{M}(E, kL\sigma) = \int \rho r^L Y_{L\sigma} d\mathbf{r} = \hat{\mathcal{Q}}_{L\sigma} \tag{2.12}$$

$$\mathcal{M}(M, kL\sigma) = \frac{1}{c(L+1)} \int (\mathbf{r} \times \mathbf{j})\nabla(r^L Y_{L\sigma}) d\mathbf{r} = \hat{\mathcal{M}}_{L\sigma} \tag{2.13}$$

for electric and magnetic transitions, respectively. As the orientation of the nuclei (characterized by m_i and m_f), as well as the polarization of the radiation (characterized by σ) is normally not of interest, Eq. (2.11) can be simplified by

averaging over the initial m_i (which introduces a sum and a factor of $\frac{1}{2I_i+1}$) and summing over all final states (m_f).

$$\Gamma(\lambda, kL\sigma) = \frac{8\pi(L+1)}{\hbar L[(2L+1)!!]^2}\Big(\frac{E_\gamma}{\hbar c}\Big)^{2L+1}\frac{1}{2I_i+1}\sum_{m_i,m_f,\sigma}|\langle I_f, m_f \,|\, \mathcal{M}(\lambda, kL\sigma) \,|\, I_i, m_i\rangle|^2 \,. \tag{2.14}$$

Using the Wigner-Eckart theorem (as defined in [80]) and the 3j-symbol representation of the Clebsch-Gordan coefficients, we can reduce the matrix element in the above equation:

$$\begin{aligned}\langle I_f, m_f \,|\, \mathcal{M}(\lambda, kL\sigma) \,|\, I_i, m_i\rangle &= \frac{1}{\sqrt{2I_f+1}}\langle I_i, m_i, L, \sigma \,|\, I_f, m_f\rangle \\ &\quad\times \langle I_f \,\|\, \mathcal{M}(\lambda, kL) \,\|\, I_i\rangle \end{aligned} \tag{2.15}$$

$$\begin{aligned}&= (-1)^{L-I_i-m_f}\begin{pmatrix} I_i & L & I_f \\ m_i & \sigma & -m_f\end{pmatrix} \\ &\quad\times \langle I_f \,\|\, \mathcal{M}(\lambda, kL) \,\|\, I_i\rangle \,. \end{aligned} \tag{2.16}$$

The property of the 3j symbol

$$\sum_{m_i,m_f,\sigma}\begin{pmatrix} I_i & L & I_f \\ m_i & \sigma & -m_f\end{pmatrix}\begin{pmatrix} I_i & L & I_f \\ m_i & \sigma & -m_f\end{pmatrix} = \sum_{m_f}\frac{\delta_{I_fI_f}\delta_{m_fm_f}}{2I_f+1} = 1 \tag{2.17}$$

allows to evaluate Eq. (2.14) to

$$\Gamma(\lambda, L) = \frac{8\pi(L+1)}{\hbar L[(2L+1)!!]^2}\Big(\frac{E_\gamma}{\hbar c}\Big)^{2L+1}B(\lambda L; i\to f), \tag{2.18}$$

where $B(\lambda L; i \to f)$ denotes the reduced transition probability that carries information on the nuclear charge and current density:

$$B(ML; i\to f) = \frac{1}{2I_i+1}|\,\langle I_f \,\|\, M_L \,\|\, I_i\rangle\,|^2 \tag{2.19}$$

$$B(EL; i\to f) = \frac{1}{2I_i+1}|\,\langle I_f \,\|\, \mathcal{Q}_L \,\|\, I_i\rangle\,|^2. \tag{2.20}$$

It can be seen from the 3j symbols in Eq. (2.16) that I_i, I_f and L must satisfy the triangle condition: From the 3j symbols the selection rules follow

$$|I_i - I_f| \le L \le I_i + I_f \tag{2.21}$$

$$m_f - m_i = \sigma. \tag{2.22}$$

Additionally, also the parity must be considered:

$$\Pi_i \Pi_f \Pi_{\lambda L} = 1, \tag{2.23}$$

with $\Pi_{EL} = (-1)^L$ and $\Pi_{ML} = (-1)^{L+1}$.
These selection rules will be applied to the $^{229\mathrm{m}}$Th to ground-state decay in the following section.

2.2.1 γ decay of $^{229\mathrm{m}}$Th

In the case of the isomeric decay in $^{229\mathrm{m}}$Th there are two states involved, characterized with $(I_i, \Pi_i) = (3/2, +)$ and $(I_f, \Pi_f) = (5/2, +)$, so that according to the above selection rules $L = \{1, 2, 3, 4\}$ is possible. From parity conservation it follows that the isomer can decay via E2, E4 and M1, M3 transitions. We only consider the lowest possible multipolarities for the transition: E2 and M1. The reduced transition probabilities are calculated in [6] and can be expressed in Weisskopf units (W.u.) [86]:

$$B(M1) = 0.0076 \text{ W.u.} \tag{2.24}$$
$$B(E2) = 29 \text{ W.u.} \tag{2.25}$$

The Weisskopf unit is a theoretical value for the reduced transition probability calculated in the single-particle nuclear shell model.
For ^{229}Th and the given types of transitions the Weisskopf units amount to

$$\text{W.u. (M1, 229)} = 3.18 \ \mu_N^2 \tag{2.26}$$
$$\text{W.u. (E2, 229)} = 130.04 \ e^2\text{fm}^2, \tag{2.27}$$

where μ_N is the nuclear magneton. Eq. (2.18) can be partially evaluated and expressed with the given reduced transition probabilities in Weisskopf units:

$$\Gamma(M, 1) = 1.779 \times 10^{13} E_\gamma^3 \ B(M1), \tag{2.28}$$
$$\Gamma(E, 2) = 1.223 \times 10^{9} \ E_\gamma^5 \ B(E2), \tag{2.29}$$

where E_γ is the transition energy in MeV, and B(M1) and B(E2) are given in the respective Weisskopf units. The evaluation of the above equation, with $E_\gamma = 8.3$ eV, leads to the following decay rates:

$$\Gamma(M, 1) = 2.46 \times 10^{-4} \ 1/\text{s} \tag{2.30}$$
$$\Gamma(E, 2) = 1.82 \times 10^{-13} \ 1/\text{s}. \tag{2.31}$$

The M1 transition leads to the lifetime of $\tau = 1/\Gamma(M,1) \approx 4 \times 10^3$ s. The decay rate of the E2 component is so low that it has no strong influence on the radiative lifetime of the isomeric state in ^{229}Th. However, as described in the next section, the electric quadrupole decay channel can play a significant role in the internal conversion decay of $^{229\mathrm{m}}$Th.

2.3 Internal conversion

Internal conversion (IC) is a decay modality of excited nuclear states. In this process the nuclear decay energy is transferred to the electronic shell, which is thereby (further) ionized. A prerequisite for the occurrence of internal conversion is that the ionization energy of the atom (or ion) has to be smaller than the energy released in the nuclear decay. IC is the dominant decay channel for ^{229m}Th atoms with an ionization potential of ≈6.31 eV [10]. For ^{229m}Th ions (the ionization potential of Th^{1+} already amounts to 11.2 eV [33]) internal conversion is forbidden. For the energy determination of the thorium isomer as presented in chapter 6, it is essential to precisely determine the kinetic energy spectrum of the emitted electrons. The kinetic energy E_e of an IC electron emitted from an atom in an electronic excited state is given by

$$E_e = E_I - IP + E_i - E_f. \tag{2.32}$$

In the above equation E_I is the excitation energy of the decaying nucleus, IP is the ionization potential of the atom, E_i is the excitation energy of the electronic excited state and E_f is the excitation energy of the ion that is generated in the IC process. The kinetic energy spectrum for internal conversion from a specific excited electronic state is given by:

$$S_{(E_I,E_i)}(E) = \sum_{E_f} \Gamma_{if}\ \delta\big(E - [E_I - IP + E_i - E_f]\big), \tag{2.33}$$

where Γ_{if} is the rate specific to the (E_i, E_f) pair and $\delta(...)$ is the Dirac delta function.
The furtheron presented calculations of Γ_{if} follow Ref. [87] and will be briefly summarized here in order to present a consistent picture of the internal conversion process. Normally, IC rates are given in terms of internal conversion coefficients $\alpha_{\mathrm{ICC}} = \Gamma_{\mathrm{IC}}/\Gamma_{\mathrm{rad}}$. These relate the IC rate (given by $\Gamma_{\mathrm{IC}} = \sum_f \Gamma_{if}$[1]) to the radiative decay rate (Γ_{rad}, see Eq (2.18)). In our experiment, however, we are interested in the decay rates Γ_{if} (and not in the total decay rate represented by the sum over all final states), therefore corresponding calculations were carried out at the Max-Planck-Institut für Kernphysik in Heidelberg and are detailed in [87]. The internal conversion decay rate can be calculated starting from an Hamiltonian that represents the interaction between the nuclear electromagnetic

[1]Note that the initial excited electronic state is normally not taken into account in IC calculations, as its excitation energy can be considered to be small compared to nuclear excitation energies in the keV-MeV region.

field and the electronic shell, and calculating the transition rates using Fermi's Golden Rule. The following Hamiltonian is used [87]

$$\hat{H}_{\text{int}} = \int \frac{\rho(\mathbf{r}')}{|\mathbf{r}-\mathbf{r}'|} d\mathbf{r}' - \frac{\boldsymbol{\alpha}}{c} \int \frac{\mathbf{j}(\mathbf{r}')}{|\mathbf{r}-\mathbf{r}'|} d\mathbf{r}', \tag{2.34}$$

which represents the Coulomb interaction of the nuclear charge (represented by $\rho(\mathbf{r}')$) and the magnetic interaction of the nuclear current ($\mathbf{j}(\mathbf{r}')$) with the atomic electrons (at coordinates $\mathbf{r}$). $\boldsymbol{\alpha}$ denotes Dirac matrices. Following [88], one finally obtains

$$\Gamma_{\text{IC}}^{\text{M1}} = \frac{8\pi^2}{9} \Lambda B(\text{M1}) \sum_{\kappa} (2j+1)(\kappa+\kappa_i)^2 \begin{pmatrix} j_i & j & 1 \\ 1/2 & -1/2 & 0 \end{pmatrix}^2 |R_{\epsilon\kappa}^{\text{M1}}|^2 \tag{2.35}$$

$$\Gamma_{\text{IC}}^{\text{E2}} = \frac{8\pi^2}{25} \Lambda B(\text{E2}) \sum_{\kappa} (2j+1) \begin{pmatrix} j_i & j & 1 \\ 1/2 & -1/2 & 0 \end{pmatrix}^2 |R_{\epsilon\kappa}^{\text{E2}}|^2, \tag{2.36}$$

for M1 and E2 transitions, respectively. In the above equations Λ takes the angular momentum coupling of the outer electrons into account and is defined in Refs [87–89]. j_i and j denote the electrons total angular momentum quantum numbers of the initial and final state, respectively. κ_i and κ are the relativistic quantum numbers (defined as $\kappa = l$, if $j = l - 1/2$ and $\kappa = -l-1$, if $j = l+1/2$). The internal conversion decay rate depends on the spatial overlap of the electron wave function with the nucleus: $R_{\epsilon\kappa}^{\text{M1/E2}}$ are radial integrals, which are defined in [87–89] and require the bound and continuum radial wave functions of the IC electron. In order to predict the IC electron spectra (as used in chapter 6), the radial integrals are evaluated with the Grasp2K package [90] and the Xphoto program from the RATIP package [91]. Due to their large spatial overlap with the nucleus, IC proceeds predominantly via s-electrons [89]. Although the electric quadrupole channel significantly contributes to the IC decay of $^{229\text{m}}$Th for p, d and f orbitals, it can be shown that the IC decay channel in $^{229\text{m}}$Th is dominated by M1 transition for $7s$ orbitals [89][2].

2.3.1 IC decay rate in solids

The internal conversion decay rate is influenced by the electronic environment. Therefore, especially for low energy nuclear isomers, it is possible to tune the lifetime by implanting the nuclei in different solid-state environments. This was already demonstrated with the isomeric state in ^{235}U (with an energy of 76.74

[2] It holds $\mathcal{O}(\Gamma_{M1}(7s)) \gg \mathcal{O}(\Gamma_{E2}(7s)) \approx \mathcal{O}(\Gamma_{M1}(7p, 6d, 5f)) \approx \mathcal{O}((\Gamma_{E2}(7p, 6d, 5f))$. [89]

eV [92] and a lifetime of ≈ 26 min [93]). ^{235m}U shows a clear dependence of the lifetime on the chemical environment [93–95]: In Ref. [94] it was found that the lifetime of ^{235m}U depends on the free-electron concentration of the material. In these measurements the ^{235}U isomer lifetime was influenced by implanting the isomer in different metals. The lifetime of the isomer is in the range of 26 minutes and could be influenced at a level of 5%. The lifetime is influenced by the valency of the host metal and a clear linear dependence on the free electron density for a given group of metals (*e.g.* noble metals, bi-valent Ni & Pt, or tri-valent Co & Ir) could be shown. It should be pointed out, however, that not only valence electrons can interact in the IC decay of ^{235m}U, but also electrons which are stronger bound. The IC decay of ^{229m}Th processes mainly via valence electrons, therefore it can be expected that the influence of the chemical environment on its lifetime is stronger than for the ^{235m}U lifetime.

2.4 Interaction of ions with solids

In the following section the interaction of charged particles with solids is briefly explained. In the experiments performed in this thesis multiply charged ions (2+ or 3+) are sent through carbon foils (a bi-layer of graphene) for neutralization. The underlying physical principles are qualitatively described in the following.

Ion surface interactions have already been studied in the 1930s [97]. Homer D. Hagstrum performed detailed studies with noble gas ions incident on clean metal surfaces starting from the 1950s [98, 99]. Electrons can be transferred from the surface of a solid to a multiply charged ion (and vice versa) in several ways [96]:
(*i*) Resonant neutralization (RN) (Fig. 2.2a) proceeds when an empty level of the ion comes into resonance with the solid's conduction band. It is possible to set an upper limit on the recombination/binding energy of the resulting electronic states that can be populated through RN. RN is only possible of the binding energy of the excited state is below the work function: $W_i < W$. As will be shown later, this will be used to estimate the range of excited states which need to be considered as initial states for IC electron spectra determination (see chapter 6). There also exists the inverse process of RN which is called resonant ionization, where an electron is transferred resonantly from the ion to the surface conduction band.
(*ii*) Auger-neutralization (AN) or Auger-deexcitation (AD) (Fig. 2.2b) is a two-electron process. In the AN, an electron from the solids conduction band is captured into an energetically lower lying level of the ion (with a binding energy W_i). The excess energy of this decay is transferred to an electron bound in the surface, which is thereby ejected into vacuum. The maximum kinetic energy of this electron is given with $E_{\max} = W_i - 2W$, with W as the surface's work-function. This sets a fixed energetic limit for the levels in the ion that can be populated in this process with $W_i \geq 2W$.
The AD process occurs, if an excited state (with a binding energy $W_i' < W$) is already populated in the ion. In this case, if an electron from the solid's conduction band is captured into a lower level of the ion, the energy is transferred to the excited electron of the ion which is ejected.
(*iii*) Auto-ionization can be understood as an intra-projectile Auger deexcitation [96]. Consider a multiply excited projectile, then the energy which is released when the one state decays is transferred to an other excited electron, which is then emitted into vacuum.
(*iv*) Radiative deexcitation is the deexcitation of an excited state by photon emission. It can be considered highly improbable compared to the other processes

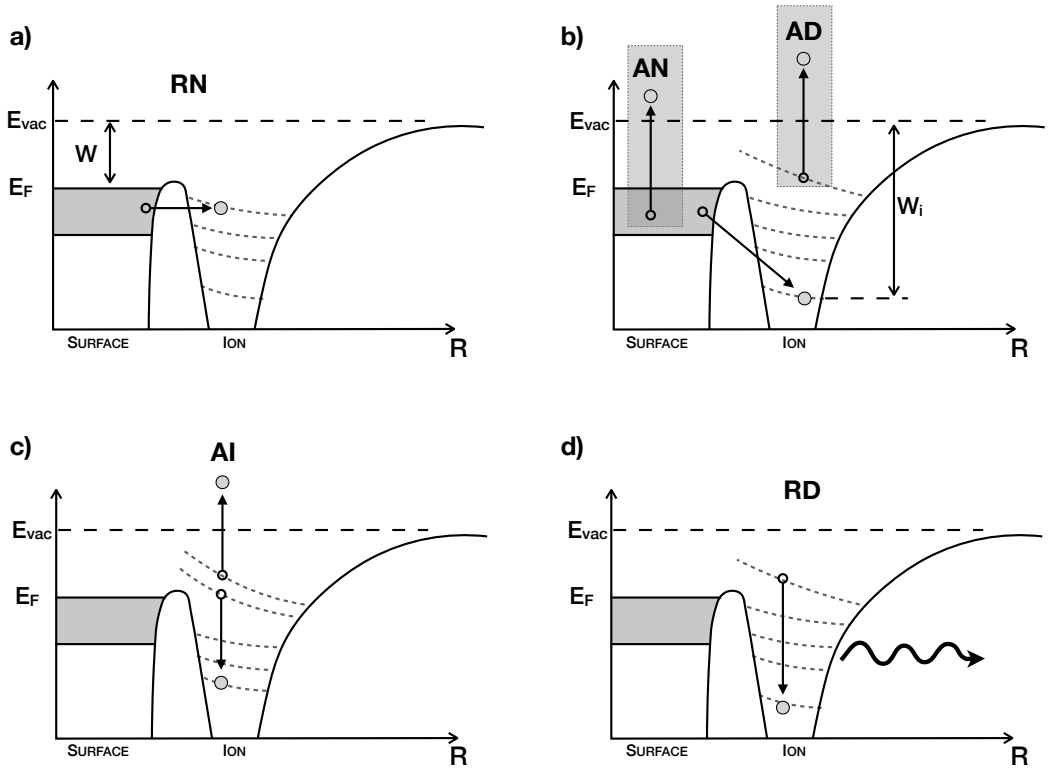

Figure 2.2: Energy diagram and possible electron transition of an ion in the vicinity to a solid surface: a) resonant neutralization (RN), b) Auger-neutralization (AN) and Auger-deexcitation (AD), c) auto-ionization (AI), and d) radiative deexcitation (RD). W labels the work function of the surface, E_F the Fermi level and E_{vac} the vacuum energy level. W_i is the binding-energy/recombination energy of the electronic level of the ion. For a detailed description of the electronic transitions see text. The figure is adapted from Ref. [96].

described above, as the transition rates are assumed to be 10^6 times smaller than the radiationless decays [96].

Assume further that a slow ion with positive charge q and kinetic energy E_{kin} approaches a solid. Slow refers to velocities comparable to velocities of bound electrons in atoms, $\alpha \cdot c \approx 2.2 \times 10^6$ m/s [3].
Already in close vicinity to the surface electrons are transferred to the ion. In this way ions of lower charge states are produced in excited states. The population of these excited states predominantly occurs via resonant neutralization. Due to image potentials, which build up on the surface as the ion approaches the surface, its electronic levels are subject to strong Stark shifts. In highly charged ions "hollow atoms" [100] are generated, *i.e.* highly excited atoms with filled outer shells but empty inner shells. These states are short-lived with lifetimes typically in the range of 100 fs [100] and decay by Auger transitions (which ultimately leads to electron emission) or soft X-ray emission. They do not play a role for the neutralization of thorium ions in the doubly or triply charged states that are used in the experiment. Even if AN, AD or AI processes ionize the atom it can be assumed that RN proceeds until the ion is fully neutralized. As the ions penetrate the solid quasi-molecular states are formed inside the target. For sufficiently slow ions incident on the target enough electrons will remain in the projectile after separation from the target to form a fully neutralized atom. Measurements that confirm the neutralization of slow Th ions incident on thin carbon foils are described in Ref. [101] and in section 4.3.

The atoms generated in such neutralization processes can be in excited states, due to RN. In order to determine which excited states one can expect, it is essential to understand which excited states have become resonant with the valence band of the target. As the excited states are subject to various shifts due to image charge, but also due to shielding of the ionic core by target electrons as they pass through the solid. Density functional theory (DFT) calculations have been carried out by the theory group from the Technical University of Vienna to understand which states of ^{229}Th become resonant as it is neutralized in graphene.

2.4.1 Neutralization of Th in graphene

As stated above, in order to know what kind of excited states to expect after neutralization of Th ions in graphene, one needs to understand how the electronic levels of Th shift in the presence of graphene. A convenient way to investigate the

[3] For ^{229}Th this corresponds to kinetic energies below 5.8 MeV.

properties of such many-body systems is to use density functional theory (DFT) calculations, which, for the sake of completeness, will be briefly explained to give a general idea of the underlying principle. The theory is based on the Hohenberg-Kohn theorem[102]: Assume an interacting system of electrons which are bound by an external potential. The goal is to find the ground-state energy E_0 of this system (so that $\mathcal{H}\Psi_0 = E_0\Psi_0$). The Hohenberg-Kohn theorem states that the ground-state energy is the minimum of an energy functional of the electron density $E[n(\mathbf{r})]$: $E_0 = E[n_0(\mathbf{r})]$, where $n_0(\mathbf{r}) = N \int d\mathbf{r}_2 ....d\mathbf{r}_N |\Psi_0(\mathbf{r}, \mathbf{r}_2, ...\mathbf{r}_N)|^2$ is the electron density of the ground state. E_0 is the unique minimum of this functional. This reduces the many-body problem to the minimization of a functional. The problem, however, is that generally the complete functional $E[n(\mathbf{r})]$ is not known and only the external potential can be expressed in terms of $n(\mathbf{r})$. There are established techniques that allow to obtain ground-state energies, such as the Kohn-Sham approach [103] (which is not detailed further in this thesis).

For the purpose of an energy determination of ^{229m}Th (chapter 6), DFT calculations have been carried out that investigate the energy of electronic levels of neutral Th traversing the graphene (for a detailed description of the computational methods that were used, see the "Methods" section of Ref. [1]). It is assumed that the Th ion moves perpendicular to the graphene sheet through the center of a graphene hexagon. It is found that orbitals with 7s and 6d characteristic come into resonance with the graphene conduction band at larger distances from the graphene surface ($\approx$ 2 Å), while for lower distances these orbitals are shifted up in energy and states connected to f orbitals become resonant. It is thus possible that excited electronic states containing f orbitals are favoured during the neutralization of Th ions in graphene. The calculations also allow to estimate the maximum accessible excited state energy of the neutralized Th atoms to be 2.5 eV. As will be shown in chapter 6, all excited states up to this excitation energy are taken into account to interpret the energy measurements and conservatively estimate the uncertainty of the experimental results.

2.5 Electrons in electromagnetic fields

Within the scope of this thesis spectroscopy of electrons emitted in the internal conversion decay of ^{229m}Th is performed. For this purpose a magnetic-bottle-type spectrometer is used, where electrons are collected in magnetic fields and guided towards a retarding field spectrometer (for experimental details see section 3.2). In the following section the behaviour of charged particles in electromagnetic fields is shortly explained, focusing on the magnetic bottle effect which is used to collect and collimate electrons in magnetic fields.

The motion of a non-relativistic electron (with mass m and charge e) in an electromagnetic field can be described by the following differential equation:

$$m\frac{\mathrm{d}^2\vec{x}}{\mathrm{d}t^2} = e\Big[\vec{E}(\vec{x}) + \frac{\mathrm{d}\vec{x}}{\mathrm{d}t} \times \vec{B}(\vec{x})\Big] \tag{2.37}$$

where $\vec{E}$ and $\vec{B}$ are electric and magnetic fields, respectively. For simplicity, $\frac{\mathrm{d}\vec{x}}{\mathrm{d}t} = \vec{v}$ is split into a component parallel to the magnetic field $\vec{v}_\parallel$ and perpendicular to the magnetic field $\vec{v}_\perp$: $\vec{v} = \vec{v}_\parallel + \vec{v}_\perp$. Eq. (2.37) then reads

$$\frac{m}{e}\frac{\mathrm{d}\vec{v}_\parallel}{\mathrm{d}t} - \vec{E}_\parallel = 0 \tag{2.38}$$

$$\frac{m}{e}\frac{\mathrm{d}\vec{v}_\perp}{\mathrm{d}t} - \vec{v}_\perp \times \vec{B} - \vec{E}_\perp = 0. \tag{2.39}$$

In the absence of an electric field (*i.e.* $\vec{E} = 0$) the above equations reduce to

$$\frac{m}{e}\dot{\vec{v}}_\perp = \vec{v}_\perp \times \vec{B}. \tag{2.40}$$

Without loss of generality we define $|\vec{B}| = B_z = B$ so that $\vec{v}_\perp = v_x + v_y$ and Eq. (2.40) separates to

$$\dot{v_x} = -\frac{q}{m}B_z v_x, \tag{2.41}$$

$$\dot{v_y} = \frac{q}{m}B_z v_y. \tag{2.42}$$

Solving these differential equations results in a circular motion in the x-y plane with an angular velocity $\omega = \frac{q}{m}B$ (and velocity $v = \sqrt{v_x^2 + v_y^2}$). The so-called gyromagnetic radius of these electrons is obtained by equating the Lorentz force

with the centripetal force:

$$qvB = \frac{mv^2}{r} \tag{2.43}$$

$$\rightarrow \; r = \frac{mv}{qB}. \tag{2.44}$$

Such an electron moving around a central point generates a magnetic moment μ that is calculated via

$$\mu = \frac{1}{2}\int \mathrm{d}^3\vec{x}[\vec{x} \times \vec{j}(\vec{x})] = AI, \tag{2.45}$$

where A is the area surrounded by the current I. In our case, the current is given by $I = q\frac{v}{2\pi r}$ and the area is given by $A = \pi r^2$, leading to the magnetic moment

$$\mu = q\frac{v}{2\pi r}\pi r^2 = \frac{qvr}{2} = \frac{mv^2}{2B}. \tag{2.46}$$

It can be shown that μ is invariant (see for example [104]), which gives rise to the magnetic bottle effect that is detailed in the following section.

2.5.1 Magnetic bottle effect

As a starting point, the z component of a magnetic field is considered to be increasing in z direction: $\frac{\partial B_z}{\partial z} > 0$. An electron being emitted at point $\vec{x_i}$ with energy E and velocity $\vec{v_i} = (v_{ix}, v_{iy}, v_{iz})$ ($|\vec{v_i}| = \sqrt{2E/m}$) inherently has a magnetic moment of

$$\mu = \frac{v_{i_\perp}^2 m}{2B_i}, \tag{2.47}$$

where $v_{i_\perp}^2 = |\vec{v}_\perp(\vec{x}_i)|^2 = v_x^2(\vec{x}_i) + v_y^2(\vec{x}_i)$ and $B_i = B_z(\vec{x_i})$. Assuming $v_z \neq 0$, the strength of the magnetic field along the electron's trajectory changes: an electron, for example, moving from point x_i with a magnetic field B_i moving to x_f with a magnetic field $B_f (\neq B_i)$. However, since μ must be invariant, $v_\perp$ must change accordingly in order to satisfy Eq. (2.46). The following equation holds for $v_\perp(\vec{x_f})$, the velocity of the electron at position x_f:

$$\frac{v_{i_\perp}^2 m}{2B_i} = \frac{v_{f_\perp}^2 m}{2B_f} \tag{2.48}$$

$$\Rightarrow v_{f_\perp} = v_{i_\perp}\sqrt{\frac{B_f}{B_i}}. \tag{2.49}$$

In the absence of electric fields, energy must be conserved, which leads to

$$\frac{m}{2}(v_{i_\perp}^2 + v_{iz}^2) \stackrel{!}{=} \frac{m}{2}(v_{f_\perp}^2 + v_{fz}^2) \tag{2.50}$$

$$\Rightarrow v_{fz}^2 = v_{iz}^2 + v_{i\perp}^2\Big(1 - \frac{B_f}{B_i}\Big), \tag{2.51}$$

with $B_f = B_z(\vec{x_f})$. This means that for decreasing magnetic fields and in the absence of electric fields, the velocity component perpendicular to the magnetic field is reduced and transferred to motion parallel to the magnetic field. We now consider two cases:
(i) $v_{iz} < 0$, which means that the electrons are initially emitted towards the lower magnetic field and $B_i > B_f$. In this case the electrons are collimated and in the extreme case $B_i >> B_f$ the velocity component perpendicular to the magnetic field ($v_{f_\perp}$) vanishes:

$$v_{fz}^2 \approx v_{iz}^2 + v_{i_\perp}^2 = \frac{2E_{\text{kin}}}{m}. \tag{2.52}$$

(ii) $v_{iz} > 0$, here the electrons are emitted against the direction of the magnetic field gradient and $B_i < B_f$ holds. If this is the case, there is the possibility that Eq. (2.51) equals to 0, which holds if the initial velocities satisfy

$$v_{iz}^2 = v_{i\perp}^2\Big(\frac{B_f}{B_i} - 1\Big). \tag{2.53}$$

In this case, the electron is reflected, such that $v_{iz} < 0$ and the first case that has been considered applies, which leads to the collimation of the electron.
The field lines of such an inhomgeneous magnetic field describe the form of a bottle, being largely separated in the region of the low magnetic field and close in the region of the strong magnetic field as a bottle neck. Therefore, this magnetic field configuration is often referred to as a magnetic bottle.

2.5.2 Magnetic bottle and electron spectroscopy

The adiabatic collection and collimation of electrons in a magnetic field can be used to measure the kinetic energy of electrons. The idea is to place the source of electrons in a strong magnetic field and to measure the electrons' kinetic energy in the region of the lower magnetic field, either via a time-of-flight (TOF) measurement or with a retarding field analyzer (RFA). No matter which approach is used, TOF or RFA, both measure v_{fz}^2. Therefore it is of major interest to

investigate how v_{fz}^2 behaves under different conditions.
Assuming that electrons with kinetic energy $E_0 = (1/2)mv_0^2$ are emitted under a pitch angle θ_i (with respect to the symmetry axis of the magnetic field, z) in a magnetic field with strength B_i

$$v_{i_\perp} = v_0 \sin(\theta_i) \tag{2.54}$$
$$v_{iz} = v_0 \cos(\theta_i). \tag{2.55}$$

Assuming $v_f = v_0 \cos(\theta_f)$ and using Eq. (2.51) leads to

$$v_{fz}^2 = v_0^2 \Big[1 - \sin^2(\theta_i)\frac{B_f}{B_i}\Big], \tag{2.56}$$
$$\theta_f = \arcsin\left(\sqrt{\frac{B_f}{B_i}}\sin(\theta_i)\right), \tag{2.57}$$

for the velocity in the z direction and the pitch angle in the presence of a magnetic field B_f. This makes it possible to calculate the maximum angle that can be achieved in the collimation. By using $\theta_i = \pi/2 \rightarrow \sin(\theta_i) = 1$ and assuming $B_f \ll B_i$, we find

$$\theta_f^{\max} \approx \sqrt{\frac{B_f}{B_i}}. \tag{2.58}$$

Using Eq. (2.51) and assuming that the electrons are emitted isotropically in 4π, it is possible to calculate how well the electrons are collimated, which is directly connected to the energy resolution of a spectrometer based on the magnetic bottle effect. If the particles are emitted isotropically, the number of particles initially emitted under an angle θ_i is given by

$$\frac{dN}{d\theta_i} = 2\pi \sin(\theta_i). \tag{2.59}$$

Making use of Eq. (2.57) allows to calculate

$$\frac{dN}{d\theta_f} = \frac{dN}{d\theta_i}\frac{d\theta_i}{d\theta_f} = 2\pi\frac{B_i}{B_f}\frac{\sin(\theta_f)\cos(\theta_f)}{\sqrt{1 - \frac{B_i}{B_f}\sin^2(\theta_f)}}, \tag{2.60}$$

which quantifies the number of electrons with a pitch angle of θ_f (in the region of the low magnetic field B_f), under the assumption of isotropic emission in 4π (in the region of B_i). The influence of different magnetic field ratios (B_i/B_f) on the relative energy resolution (*i.e.* $(v_{fz}/v_0)^2$) is plotted in Fig. 2.3. It is clearly

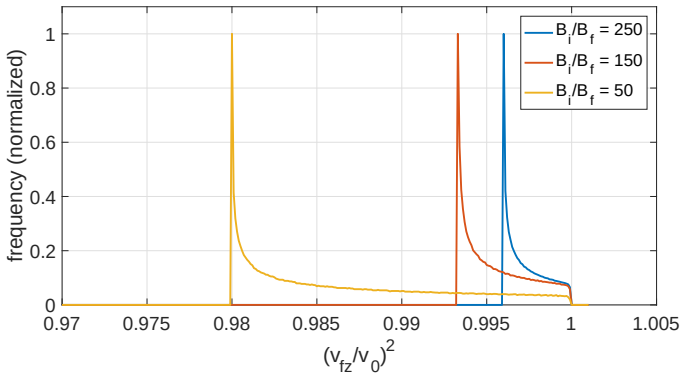

Figure 2.3: The resulting distribution of $(v_{fz}/v_0)^2$ according to Eqs. (2.56) and (2.60). It is assumed that electrons are emitted isotropically in 4π with a kinetic energy of $1/2mv_0^2$ in a strong magnetic field B_i. Different ratios of the strong (B_i) and weak (B_f) magnetic field are plotted.

visible that $(v_{fz}/v_0)^2$ is spread within $(v_{fz}/v_0)^2 \times [(1 - B_f/B_i), 1]$. This means that the spread of electron energies as measured in the weak magnetic field of the magnetic bottle, *i.e.* the energy resolution of such an instrument, depends strongly on the ratio of (B_f/B_i). In the experimental setup that is used for the energy measurements (see sections 3.2 and 4.2 and chapter 6) the ratio typically amounts to 1/100, which allows to estimate the relative energy resolution to be 1%.

CHAPTER 3

Experimental Setup

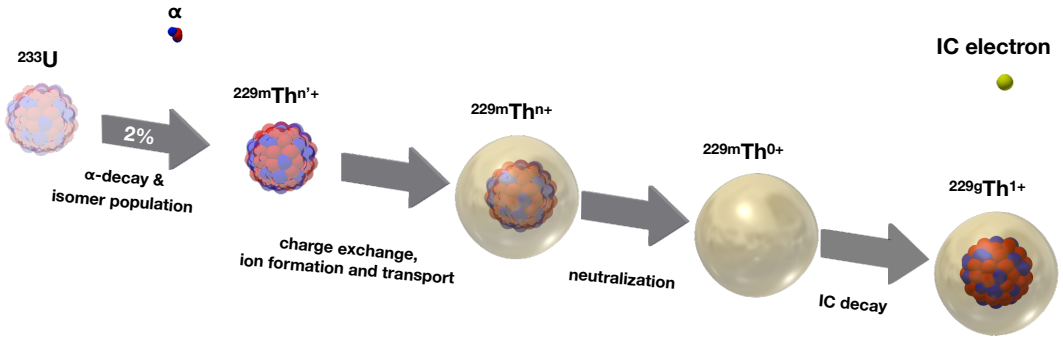

Figure 3.1: The physical principle of the experiment. ^{229m}Th is populated by a 2% decay branch in the α decay of ^{233}U. Afterwards, a $^{229(m)}$Th ion beam is formed to spatially separate the ^{229m}Th ions from ^{233}U. In a next step, the ions are neutralized, which opens the internal conversion (IC) decay channel.

The experimental setup is designed for the measurement of the ^{229}Th isomer lifetime and excitation energy using electrons that are emitted in the internal conversion ground-state decay. The underlying concept of the experiment can be broken down into four parts:
First, the isomer is populated by a 2% decay branch in the ^{233}U α decay (as outlined in chapter 1). A ^{233}U α-recoil source is used, where the $^{229(m)}$Th ions are able to leave the source material due to the kinetic recoil energy (≈84 keV) which is gained in the ^{233}U α decay.
Second, ^{229m}Th α-recoil ions are spatially separated from the ^{233}U source. This is done in order to reduce parasitic prompt background originating from the α

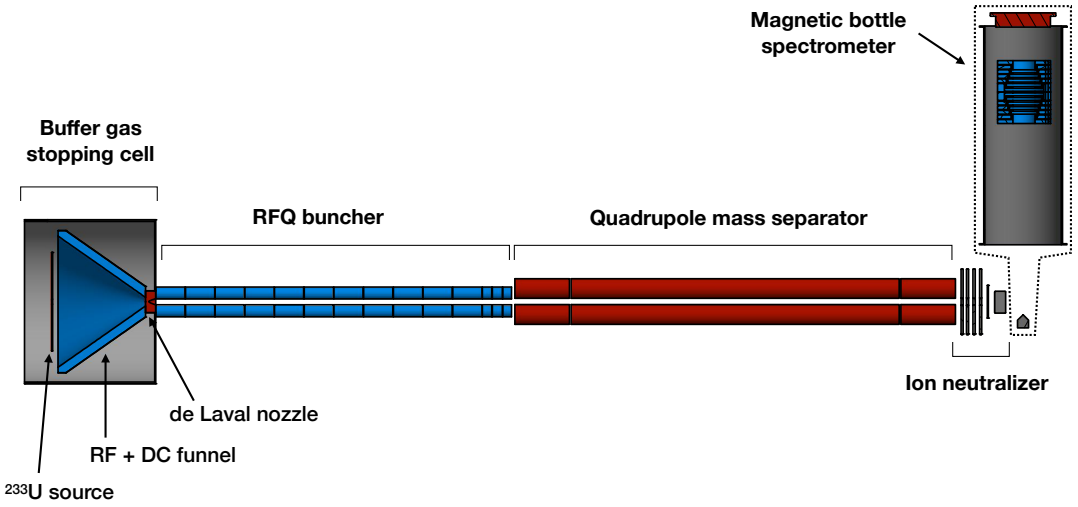

Figure 3.2: Overview of the experimental setup that is used to extract $^{229(m)}$Th from a ^{233}U α recoil source that is used to characterize the properties of ^{229m}Th. $^{229(m)}$Th ions are neutralized in an an ion neutralizer and the kinetic energy of subsequently emitted internal conversion electrons is measured with a magnetic bottle spectrometer. Details are given in the text.

decay that is accompanying the generation of the isomer. Therefore, $^{229(m)}$Th ions emerging from the ^{233}U source are thermalized in ultra-pure He buffer gas and then guided with electric fields (RF+DC funnel and RF-quadrupole ion buncher in Fig. 3.2). This also allows to select ions with a specific mass-to-charge ratio in a subsequent quadrupole mass separator (see Fig. 3.2). The expected lifetime of the isomer in ^{229m}Th ions is in the range of minutes to hours [4–7], which prevents strong depletion of the isomer content in the ion beam.
In a third step, the ^{229m}Th ions are neutralized, which opens the internal conversion decay channel. Finally, the conversion electrons are detected. The temporal decay behaviour is measured in order to determine the isomer's lifetime and their kinetic energy is measured with an electron spectrometer in order to deduce the excitation energy of the isomer.

Parts of the experimental setup (shown in Fig. 3.2) are based on previous works [74, 105]. In this work, the electronics of the setup was extended in order to allow for the bunching of ions (detailed in section 3.1.2). Additionally, the experiment was extended by an electron spectrometer (section 3.2) and a setup to neutralize

the ^{229m}Th ions (see section 3.3).
The bunching of ions serves two purposes: first it allows to perform lifetime measurements of the ^{229}Th isomer (see chapter 5). Second, it increases the signal-to-noise ratio, which is essential for the energy determination.
The spectrometer is a magnetic-bottle-type retarding field spectrometer, which is described and characterized in sect. 3.2 and used in the energy measurements presented in chapter 6.

3.1 Extraction of $^{229(m)}$Th

The following section describes the extraction and formation of $^{229(m)}$Th ion bunches from a ^{233}U α-recoil source. A detailed description of the buffer gas stopping cell can be found in [105, 106] and the extraction efficiency of $^{229(m)}$Th from the buffer gas stopping cell is given in [107].
The extraction setup consists of three differentially pumped vacuum chambers: A buffer-gas stopping cell to thermalize the energetic recoil ions, a vacuum chamber that houses an axially segmented radio-frequency quadrupole ion guide to generate a buffer-gas cooled ion beam (or ion bunches), and a vacuum chamber that contains a quadrupole mass separator for mass purification of the ion beam (or ion bunches). The vacuum chambers are pumped by three turbo-molecular pumps which share one oil-free scroll roughing pump (Oerlikon, Screwline SP 250, with 250 m^3/h pumping capacity).

3.1.1 Buffer-gas stopping cell

The $^{229(m)}$Th ions that are produced in the ^{233}U α-decay have kinetic energies of 84 keV. Due to their large kinetic energies a large fraction of the ions is able to leave the ^{233}U source (see the description of the uranium source below). Due to charge exchange processes in the source material, the recoil ions will be highly charged [108, 109]. These ions are thermalized in collisions with helium (He) buffer gas. Therefore the uranium source is placed in a buffer-gas stopping cell which comprises a cylindrical vacuum chamber (length 480 mm, diameter 250 mm) filled with 32 mbar ultra-pure He (He 6.0, *i.e.* purity of 99.99990 %.). In order to prevent neutralization (due to charge exchange with impurities) or molecule formation of the recoil nuclei, all contaminants need to be removed from the buffer gas. To ensure highest purity of the buffer gas, the buffer-gas stopping cell was designed to meet ultra-high vacuum (UHV) requirements: all

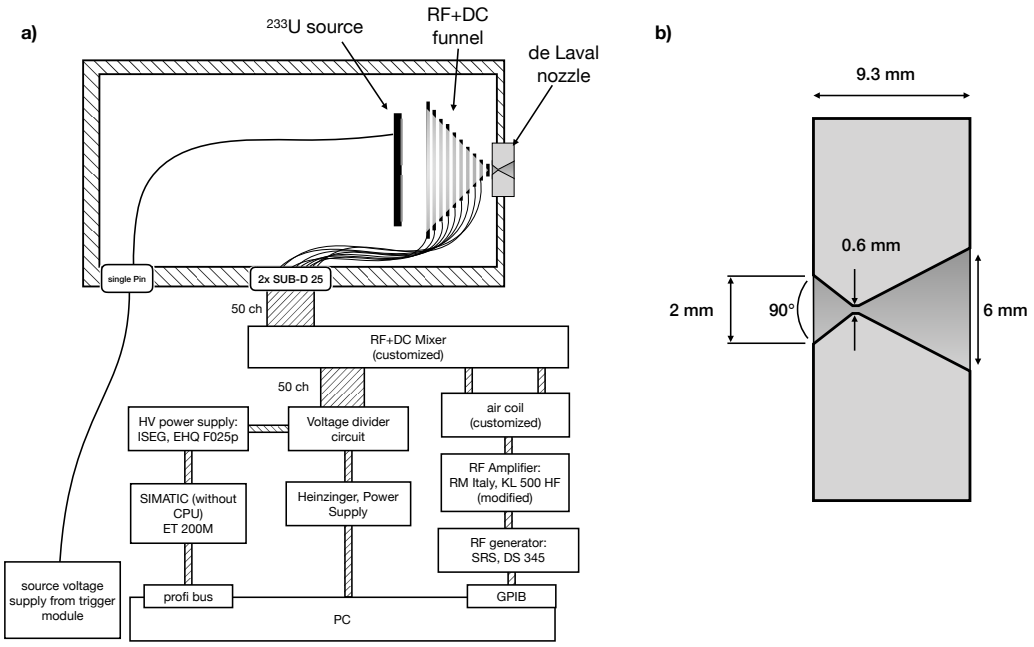

Figure 3.3: The left panel shows a scheme of the buffer gas stopping cell together with the electronics that is used to operate the cell. The geometry and dimensions of the extraction nozzle are shown in the right panel.

components forming the buffer-gas stopping cell are made from stainless steel or ceramics, are bakeable and have low outgassing rates. Before operation the cell is baked out for several days (at a temperature of T= 130° C) and the base pressure (without the buffer gas supplied) is in the lower 10^{-10} mbar region.

Pumping: The buffer-gas stopping cell is pumped by a turbo molecular pump (Pfeiffer TMU 400 M, 400 l/s, combined with a Pfeiffer TCM 1601 controller). During extraction (when the cell is filled with the helium buffer-gas) the turbo pump is decoupled from the cell with a DN160CF all-metal shutter valve (VAT type 4820-CE74).

Helium Supply: The supply of pure helium is a prerequisite for the efficient extraction of recoil ions. A helium gas cylinder (AirLiquide, 200 l, He 6.0) is attached via a pressure reducer (Druva, FMD 502-16) to a gas purifier (SAES Getter Systems, MonoTorr, PS4-MT3-R-2). The helium flow can be controlled with a gas flow controller (AERA FC-780CHT). The gas tubing consists of electro-

polished stainless steel tubes (1/2"Ø) that are fed through a cryo-trap that can optionally be filled with liquid nitrogen for a further purification of the helium. The gas flow is adjusted such that in equilibrium a pressure of 32 mbar is reached in the buffer-gas stopping cell. The gas pressure is monitored with two pressure gauges, one for the UHV regime (Pfeiffer PBR 261) and a capacitance gauge for the operation with buffer gas (Pfeiffer CMR 261).

Uranium Source: The uranium source consists of 290 kBq of metallic ^{233}U electro-deposited on a mirror-polished and titanium sputtered (with a thickness of 100 nm) silicon waver. The ≈7 nm thick uranium layer is deposited over a diameter of 90 mm with a central hole of Ø12 mm, resulting in an effective area of 62.5 cm^2. For comparative measurements a ^{234}U source with identical geometry and comparable activity (260 kBq for ^{234}U) is used. In preparatory measurements recoil rates of 100 000 1/s and 78 000 1/s have been found [106]. During extraction or loading of the RFQ-buncher the source is typically set to an offset of +80 V.

RF & DC Funnel: The thermalized ions are guided by 50 concentric ring electrodes, which are placed in front of the source, towards the exit of the buffer-gas stopping cell. The ring electrodes are arranged in a funnel-like structure with decreasing inner diameter, starting from ≈ 115 mm to 5 mm. The total length of the funnel is 80 mm, thus a cone with an opening angle of 70° is formed. The distance (along the beam axis) between the first 30 ring electrode centers is 2 mm and 1 mm between the last 20 ring electrode's centers. Each ring electrode can be set to an individual DC offset. This allows to generate a potential gradient and drag the ions towards the exit of the buffer-gas stopping cell. A voltage gradient of 4 V/cm is applied in all measurements. Additionally, an RF voltage is applied to the ring electrodes. The RF voltages of neighboring ring electrodes differ in phase by 180° and prevent the ions from colliding with the electrodes and being lost for further extraction. Typically, RF voltages with 120 V_{pp} at 850 kHz are applied.

De-Laval Nozzle: The efficient transport of the ions from the buffer-gas stopping cell to the extraction-RFQ chamber is achieved with a supersonic gas jet that is generated in a de-Laval nozzle. Its geometry is shown in Fig. 3.3b. The nozzle with a Ø0.6 mm nozzle throat connects the buffer-gas stopping cell, which is typically at a pressure of 32 mbar, with the subsequent vacuum chamber which is pumped to a pressure in the range of 10^{-4} mbar. The large pressure difference generates a supersonic gas jet which drags the ions off the electric field lines and injects them into the subsequent vacuum chamber. The dimensions of the nozzle are shown in Fig. 3.3b. The nozzle is manufactured from stainless steel and embedded by a metal-ceramic soldering into an electrically isolating environment,

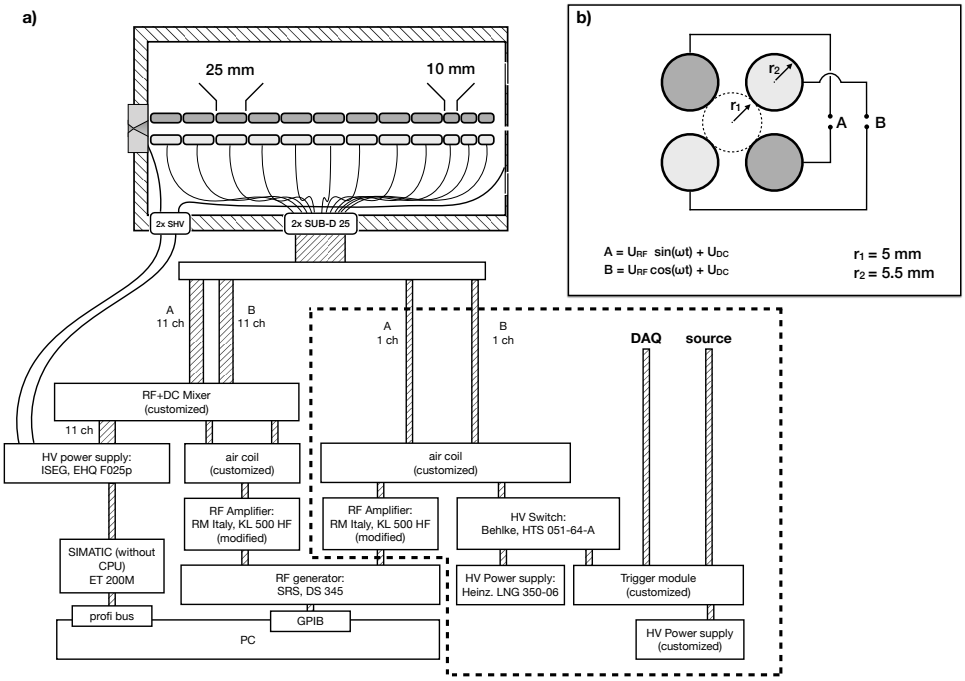

Figure 3.4: Scheme of the electronics that is used to operate the radio-frequency quadrupole (RFQ) ion buncher. Additionally, the offset supplied to the extraction nozzle, as well as an offset applied to a ring electrode which is separating the RFQ from the subsequent QMS is shown. The electronics used for the bunch generation is framed by dashed lines. Further details are given in the text and in Fig. 3.5. The inset (b) shows the geometry of the RFQ as well as its electrical connections.

thus allowing to operate it as the last buffer-gas cell electrode. It is typically held at an offset voltage of 22 V (see Appendix table C.1).

3.1.2 RFQ ion buncher

The radio-frequency quadrupole (RFQ) ion buncher consists of four axially segmented rods (see Fig. 3.4). The first 9 segments have a length of ≈25 mm, while the last 3 segments have a length of ≈10 mm. A sectional view as well as a block diagram of the electronics of the RFQ ion buncher is shown in Fig. 3.4a. A cross-sectional view of the 4-rod arrangement together with the corresponding dimensions is depicted in Fig. 3.4b. The two channels (A and B) represent two

phases (with a phase difference of 180°) of the RF voltage which are supplied to neighbouring rods. The ambient buffer-gas pressure in the RFQ is in the range of 10^{-4} mbar. The ion beam is phase-space cooled due to collisions with the background gas. The RFQ chamber is baked (at $T = 130°$ C for several days) in order to reach a pressure of 10^{-10} mbar before starting operation by supplying helium to the buffer-gas stopping cell. The buffer-gas pressure requires a voltage gradient along the RFQ to drag the ions through the remaining buffer gas. Each segment can be set to an individual DC offset, which provides the DC gradient along the beam axis.
To enhance the peak flux of ^{229m}Th ions and to allow for lifetime measurements of ^{229m}Th (see chapter 5), the RFQ is operated as an ion buncher (in the form of linear Paul trap). For ion bunch generation, the DC-potential curve along the beam axis is set such that a potential well is generated that allows to collect ions in the next-to-last segment of the RFQ. Therefore, the DC voltage of the last RFQ segment is raised above all other segments (typically $\approx +34$ V). The segment next to the last segment is lowered and defines the potential minimum in the RFQ. As the ions are cooled by the remaining buffer gas, they are collected and trapped in the potential minimum of the RFQ. After a short cooling period (typically in the range of some tens of milliseconds), the DC voltage of the last segment is set to 0 V within a fraction of a μs to release the bunch (depicted by the red dashed line in Fig. 4.1). During the cooling period no ions are loaded into the trap. This is achieved by setting the DC offset of the ^{233}U source to 0 V, so that the ions are repelled by the RF & DC funnel.
The electronics used to operate the extraction RFQ is schematically shown in Fig. 3.4: RF voltages are generated by an RF generator that is controlled with a personal computer. The RF generator output is amplified in an RF amplifier and then fed to an air coil that generates two high RF voltages (whose phase is shifted by 180°). RF voltages with 120 V_{pp} at a frequency of 880 kHz are supplied. The two signals are fed to an RF and DC mixer (detailed in Fig. 3.5). In the RF+DC mixer, the RF-voltage is mixed with the DC offset that is generated from a HV power supply which is controlled by the PC via a SIMATIC controller. Typically, a gradient of -0.2 V per segment is applied, starting with a DC offset of 21.8 V applied to the first segment. The circuit that drives the last RFQ segment is detailed in Fig. 3.5. The switching of the last electrode is controlled with a customized trigger module, which also applies the voltage to the ^{233}U source. The fast switching of the last electrode is a key element for the generation of short ion bunches and required a modification of the setup described in [105]: Previously, the offset voltage was applied via the RF-DC mixer which acts as a low-pass filter for the applied DC voltage, thereby inherently preventing the fast

switching of DC voltages. The electronics of the RF-DC mixer (for one segment) is shown in Fig. 3.5a. Therefore, the electronics of the last RFQ segment was decoupled from the one supplying the other RFQ segments (shown in Fig. 3.5). The DC voltage for the fast switchable segment is applied directly to the center of the two counter-wound coils. In this way the low-pass filter that decouples the RF voltage from the DC voltage and also prevents fast DC-voltage switching, is circumvented and fast DC-voltage switching becomes possible. A scheme of the electronics is shown in Fig. 3.5b. The voltage is switched with a fast high voltage switch (Behlke, HTS 051-64-A).

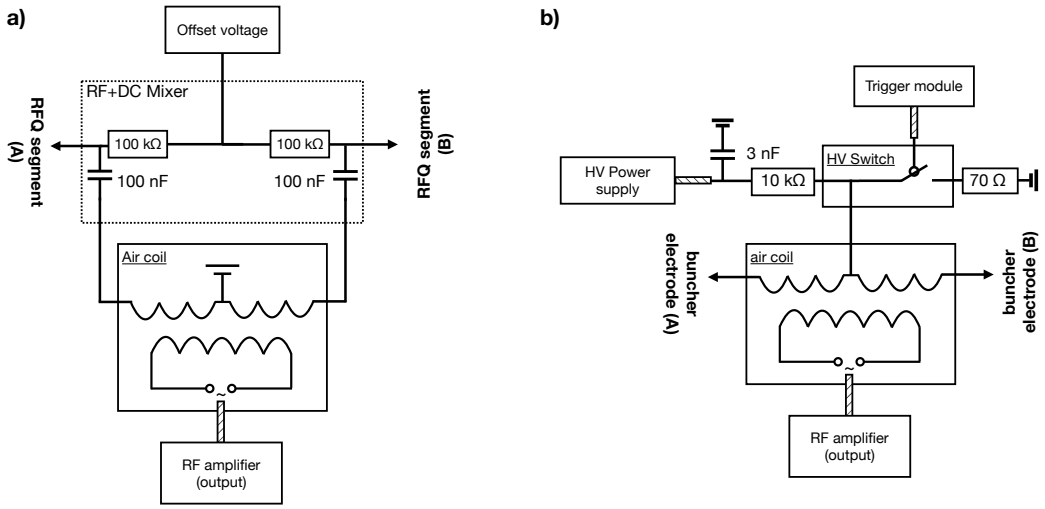

Figure 3.5: The electronics of the RF+DC mixer designed to supply one segment with a DC offset voltage (the two channels A and B represent the phase-shifted RF voltages) is shown in the left panel (a). The right panel (b) shows the central structure of the bunching unit. The DC voltage of the buncher electrodes is applied to the center of a counter-wound coil. When the fast high-voltage switch is on, the voltage is set to ground.

3.1.3 Quadrupole mass separator

At this point of the extraction process still all isotopes of the ^{233}U decay chain are contained in the ion bunches. Therefore, to purify the ion beam and select a specific charge state, a quadrupole mass separator (QMS) can be employed. The QMS consists of three quadrupole segments. The central segment has a

length of 300 mm and is placed inbetween two 50 mm long segments (known as Brubaker lenses [110], to reduce stray fields). The rods have diameters of 18 mm and are separated by 15.96 mm (the design parameters were taken from [111]). From the Mathieu equations that describe the behaviour of charged particles in AC-multipole fields, it follows that an RF quadrupole serves as a high-pass mass[1] filter. The cut-off mass depends on the applied RF frequency and RF voltage V_{pp} and the geometry of the quadrupole (defined by the radii of the rods and the spacing of the rods). Typically, RF voltages from 600 V_{pp} (for Th^{2+}) to 900 V_{pp} (for Th^{3+}) at 926 kHz are applied (see table C.1). Low-pass mass filter properties can be generated by additionally setting a DC potential between neighbouring rods. DC voltages range from 50 V to 70 V, depending on the selected mass and the desired mass resolution.
The use of high- and low-pass filter properties of the QMS allows to select a specific mass-to-charge ratio region $[m/q, m/q + \Delta m/q]$. The QMS that was used in the experiements reaches a mass resolution of $m/\delta m = 150$ with a transmission of 80%. This can only be achieved with an active stabilization of the RF voltages and putting high requirements on the manufacturing tolerances of the rods (of only 40 μm). The QMS is set to an offset of -2 V.
During the energy measurements presented in chapter 6, the QMS is used as an ion guide. This means that only the high-pass properties of the QMS are employed by setting the mass selecting DC-voltage to 0 V.

3.1.4 Particle detection and data acquisition

For ion and electron detection a multi-channel plate (MCP) detector [112] in chevron geometry is used. A Hamamatsu type F-2223 serves as a base for two different types of multi-channel plates (Hamamatsu, Type F1552 and GIDS, Type MCP-25-10-40-Image) both with a diameter of 27 mm. In the experiments no dependency on the type of MCP plates was found.
The working principle of an MCP detector is briefly discussed in the following: An MCP plate consists of a coated substrate with microchannel holes of 12 μm diameter (arranged on a grid with 15 μm pitch size). A voltage gradient is created along the microchannels, which is due to DC voltages applied to the front- and backside of such an MCP plate. When a particle impinges on the MCP surface it generates secondary electrons. If these electrons enter a microchannel, they are accelerated by the voltage gradient generated along the channel. When such an electron hits a channel wall, again secondary electrons are released and also

[1] RFQs serve as filter for selectable mass to charge ratios, for simplification only the mass is mentioned.

accelerated in the channel. In this way an electron cascade is generated which produces a measurable signal on the anode that can be read out.
The MCP detection efficiency is energy dependent. For electrons it peaks at ≈300 to 500 eV, for ions (and atoms) the detection efficiency saturates with energies larger than ≈ 1 keV to 1.5 keV [113]. The maximum detection efficiency (typically around 60 %) is defined by the open area ratio (*i.e.* the ratio of the open channel area to the total area of the MCP plate) [113].
For operation (*i.e.* for the acceleration of secondary electrons to the anode) the gradient inside the MCP ($\Delta U = U_{\text{anode}}$-$U_{\text{front}}$) needs to be positive. ΔU is typically in the range of 1.8 kV to 2 kV. For ion detection, the front (surface) of the MCP is set to a negative potential.

The electronics to operate and read out the MCP is shown in Fig. 3.6. The signal from the MCP anode is fed into a customized fast pre-amplifier (ORTEC, VT120 customized). The customization allows to apply a bias voltage of up to 2.4 kV to the anode. Pre-amplified signals are forwarded to an amplifier (ORTEC, 572A) and subsequently to a custom made Constant Fraction Discriminator (CFD). The CFD output is then fed via a connection block (National Instruments, BNC 2121) into a data acquisition PCI card (National Instruments, PCI 6602). The data is recorded in a scaler mode (*i.e.* counts are recorded in time bins of selectable width) after receiving a trigger pulse from the customized buncher trigger module. This trigger pulse starts a function generator, which serves as an external clock for the time bins in the scaler. Data is typically recorded in time bins of 1 μs.
During the lifetime measurements presented in chapter 5, the (Amplifier + CFD + PCI card) based acquisition is replaced by a commercial multichannel scaler that combines amplifier and discriminator (Stanford Research, SR 430) which allows to collect data in shorter time bins of typically 160 ns.

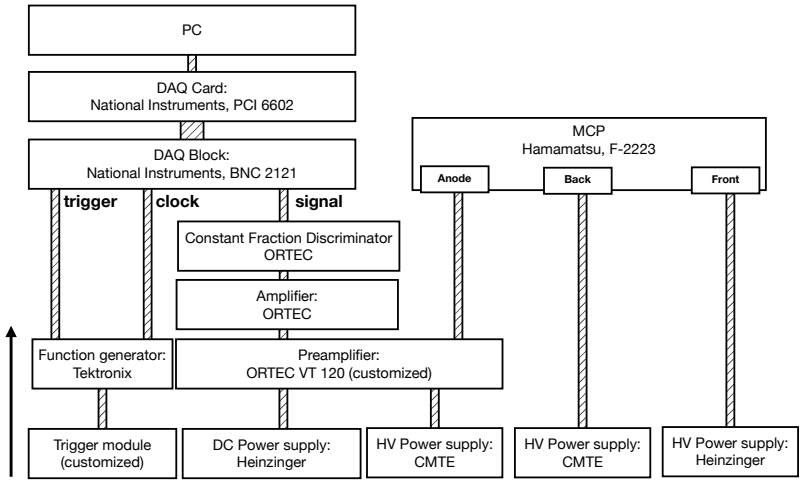

Figure 3.6: Data acquisition setup for the bunched ions. The data acquisition is started by a trigger module, which is also triggering the release of the ion bunches. A function generator is used to generate a clock signal for the time bins which is fed to a personal computer via a PCI DAQ card. The MCP signal (coming from the MCP anode) is fed through a pre-amplifier, amplifier and a Constant Fraction Discriminator to the DAQ card. The customized pre-amplifier allows to apply an offset to the MCP anode, which is required for electron detection.

3.2 Magnetic bottle spectrometer

A magnetic-bottle type retarding field spectrometer is used to measure the kinetic energies of the internal conversion electrons. This type of spectrometer uses an inhomogeneous magnetic field to collect and collimate electrons. The underlying physical principle is detailed in chapter 2.5.2 and depicted in Fig. 3.7. As the magnetic field strength decreases, the electrons velocity is adiabatically aligned with the magnetic field lines.
The spectrometer consists of a strong permanent magnet which generates a strongly inhomogeneous collection field and a solenoid that generates a weak homogeneous transport field. Electrons are collected in a volume above a strong permanent magnet and are redirected adiabatically towards the coil. In this way a collimated electron beam is generated (see chapter 2.5.2). The kinetic energy of the electrons is then analyzed by applying an electrical retarding field. Electrons

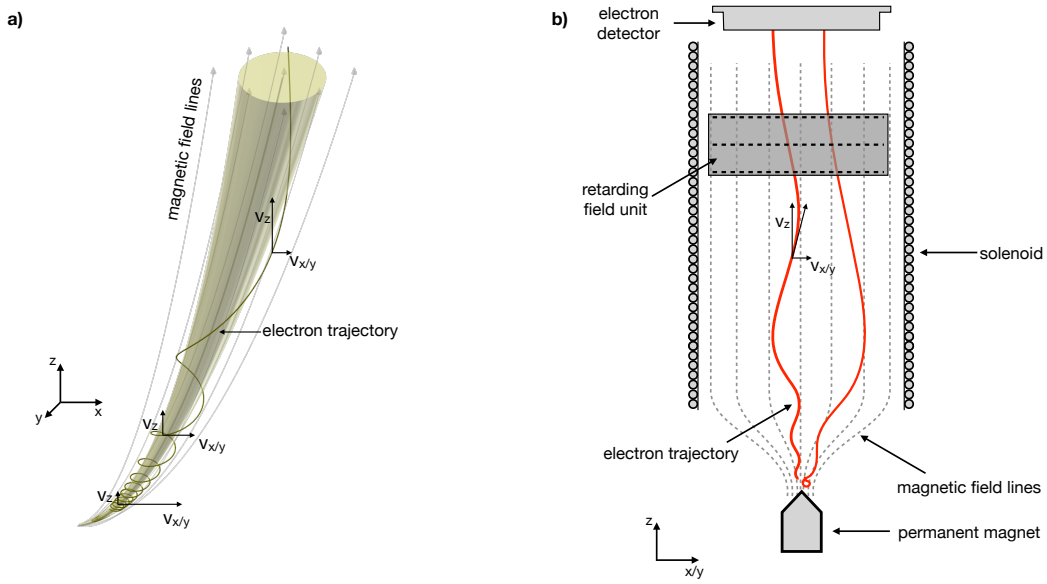

Figure 3.7: Visualization of an electron trajectory in an inhomogeneous magnetic field (the left panel a). The electron spirals along the magnetic field lines. As the magnetic field strength decreases along the z axis, the velocity component perpendicular to the z axis is redirected onto the z axis. The right panel (b) shows the technical realization of a magnetic bottle spectrometer that uses inhomogeneous magnetic fields to generate a collimated electron beam. This allows to determine the electron energy via an electric retarding field which is applied to the central grid in the retarding field unit. Sufficiently energetic electrons surpass the retarding field and are detected with an electron detector.

whose energy is sufficient to overcome the applied potential are counted with an MCP detector. A technical drawing is shown in Fig. 3.8. The coil is attached directly on a DN CF150 to DN CF100 adapter flange that also holds two single pin electrical feedthroughs (not shown in Fig. 3.8) to supply the coil. The MCP detector as well as the retarding field units are mounted on a DN CF100 to DN CF40 adapter flange. Electrical connections of the MCP detector and the retarding field unit are provided via 4 SHV electrical feedthroughs on a DN CF 40 flange[2].
The magnetic bottle spectrometer components and its performance are detailed in the following sections and also described in [114].

[2]Allectra GmbH, custom made.

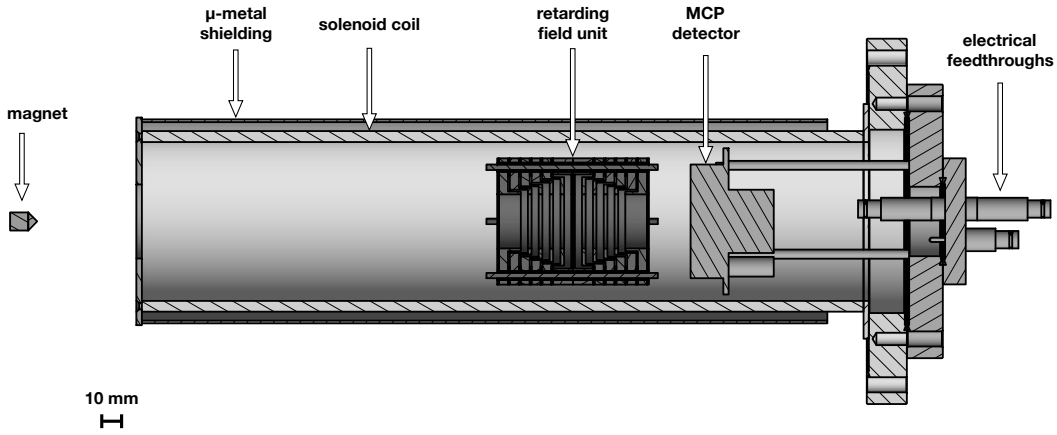

Figure 3.8: Sectional view of the magnetic bottle spectrometer. A detailed description is given in the text.

3.2.1 Magnetic fields

The strong magnetic field is generated by a permanent magnet[3] to which a soft iron cone is attached. The field strength of the magnet ≈3 mm above the soft iron cone tip has been measured to be ≈200 mT. Measurements of the magnetic fields were performed with an axial hall probe[4].
The solenoid consists of 328 windings of Kapton-insulated copper wire around an aluminum body (height: 400 mm, inner diameter: 90 mm, outer diameter: 100 mm). The radial and axial magnetic field of the coil with a current of 2 A are shown in Fig. 3.9 and amounts to 2 mT. The findings serve as an estimate for the achievable energy resolution and the homogeneity of the magnetic fields. The relative energy resolution $\Delta E/E$ of the spectrometer is given by

$$\frac{\Delta E}{E} > \frac{B_f}{B_i} = \frac{2\ \mathrm{mT}}{200\ \mathrm{mT}} = 1\%. \tag{3.1}$$

For a proper shielding of disturbing magnetic fields, the coil is shielded by a 1.5 mm thick μ-metal cylinder[5].

[3]Vacuumschmelze, VACODYM® 722 HR Ø 10 mm × H 10 mm.
[4]LakeShore Cryotronics Inc., MSA-2204-410 Hall Probe, read out with a LakeShore Model 410 Hand-held Gaussmeter.
[5]Marchandise Technologie GmbH, custom made.

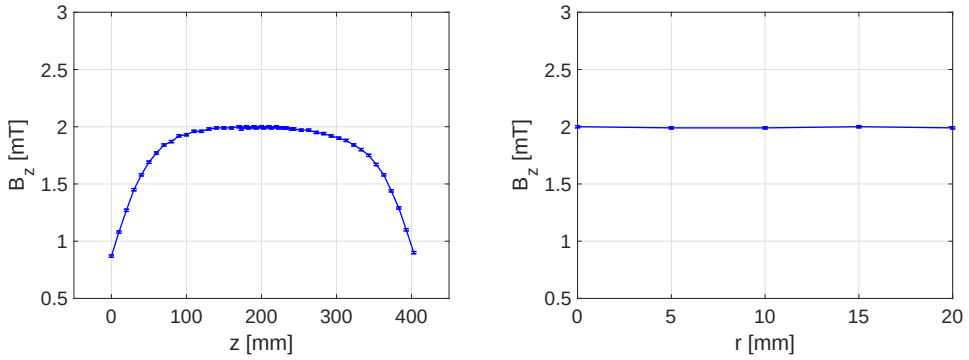

Figure 3.9: Result of the magnetic transport field measurement in axial (left) and radial (right) direction. Error bars indicate the error estimated as 1% of the measured value.

Moreover, it is assumed that the electrons are emitted from a spherical volume with radius r. As the electrons are following the magnetic field lines, the source area is magnified by a factor

$$\mathcal{M} = \sqrt{\frac{B_i}{B_f}} \approx 10. \tag{3.2}$$

Therefore, assuming an emission volume of radius 1.5 mm leads to a collimated electron beam with a radius of 15 mm. As the open area of the retarding field unit is fixed to r =15 mm, a magnification larger than $\mathcal{M}$ =10 (*e.g.* by using a lower magnetic field in the coil) leads to a reduction in count rate, since the electron beam will be shadowed.

3.2.2 Electric retarding fields

The electric retarding fields are applied with an electrode structure that consists of ring electrodes made from aluminum. Figure 3.10a shows a sectional view of the whole retarding field unit. The electrodes are radially fixed by ceramic bushings[6] and are held in place by titanium M3 threaded rods, which also serve as a mounting structure. Spatial separation and electrical insulation of the electrodes is ensured by ceramic washers[6]. The outermost and central electrodes are terminated with electrocasted gold grids[7]. DC voltages are applied symmetrically

[6]Vitron Spezialwerkstoffe GmbH, VITRONIT®.
[7]precision e forming: MG20, 90 Lines per inch, 90% transmission.

around the central electrode, via a voltage divider (R = 5 MΩ). The ring electrodes ensure a smooth slope of the electrical field towards the blocking voltage, which is defined by the central grid. In a magnetic bottle spectrometer, the electron source area is imaged and magnified as the electrons are guided by magnetic fields. The central open area (r = 15 mm) of the retarding field analyzer has been adapted to the theoretically expected source size (spherical volume with r < 1.5 mm) and magnification ($\mathcal{M}$ =10).

The electrical field from the grounded gold grids penetrates through the retarding field grid and the electrical potential in the center between its grid bars is lower (by ΔV) than the actual applied voltage. This might influence the energy resolution of the spectrometer. ΔV can be calculated via [115]

$$\frac{\Delta V}{V} = \frac{2\pi d/a - \ln(4)}{2\pi d/a - 2\ln(2\sin(\pi r/a))}, \tag{3.3}$$

with r being the radius (or half the width) of the grid bars, a as the distance between two grid bars and d the distance between the potential mesh and the grounded mesh. For the grid that is used in the experiment (r = 7 μm, a = 270 μm, and d = 41 mm) one finds a value of

$$\frac{\Delta V}{V} \approx 0.5\%. \tag{3.4}$$

Since $\Delta V/V$ is directly proportional to $\Delta E/E$, this gives a lower limit of the achievable energy resolution.
The performance of the retarding field unit was examined in simulations using the SIMION ion optics simulator [116]. In these simulations the influence of inhomogeneities of the electric field on the energy resolution was investigated. Electrons with two different kinetic energies (1.4 eV and 1.5 eV) are used and a homogeneous magnetic field (with strength 2 mT) was assumed. The electrons are initially emitted under pitch angles of 0° and 5°. This range of pitch angles can be expected from the magnetic field configurations (see section 2.5.2 and the previous section). The number of electrons, whose energy is sufficient to surpass the retarding field analyzer at different blocking voltages is plotted in Fig. 3.10b. It is clearly visible that blocking voltage dependent edges are broadened for electrons which are emitted with a non-zero pitch angle. The broadening is due to inhomogeneities of the electric fields inside the retarding field analyzer.

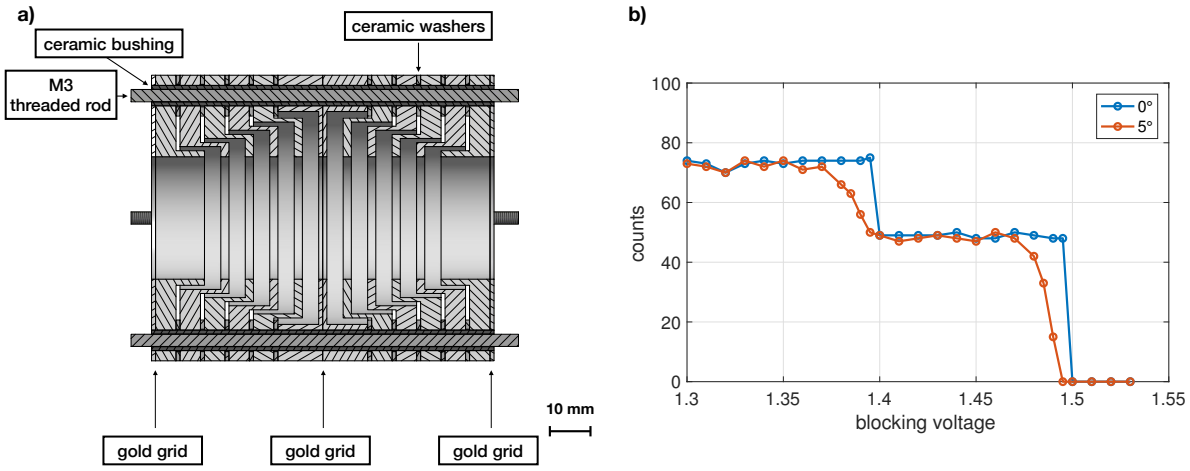

Figure 3.10: A sectional view of the retarding field unit is displayed in the left panel. The right panel shows the result from SIMION simulations (electrons with kinetic energies of 1.4 eV and 1.5 eV, respectively, were simulated). Details are given in the text. Figures are taken from [114].

3.3 Ion neutralizer

In order to allow for the internal conversion decay of the isomeric state in ^{229}Th, ^{229m}Th ions need to be neutralized. This can be achieved in several ways: a simple method is to collect the ^{229m}Th ions on a metal surface [4, 11, 74]. For an energy determination via internal conversion electrons, however, the metal surface (and possible surface contaminations) may introduce systematic effects which makes a precise energy determination cumbersome.
For this reason the aim was to neutralize ^{229m}Th ions in flight and to measure the internal conversion decay from free ^{229m}Th atoms. There exist several methods to neutralize ions in flight, either by charge exchange in a metal vapor [117], reflecting charged particles from metal surfaces under grazing incidence [118] or by charge exchange in thin carbon foils [119]. As the technical realization of charge-exchange in carbon foils is simple, it was decided to use this scheme for the neutralization of ^{229m}Th ions.

Two types of foils were used in the experiments: a bi-layer of graphene[8] (used

[8]MicroToNano, V.O.F Amsterdam.

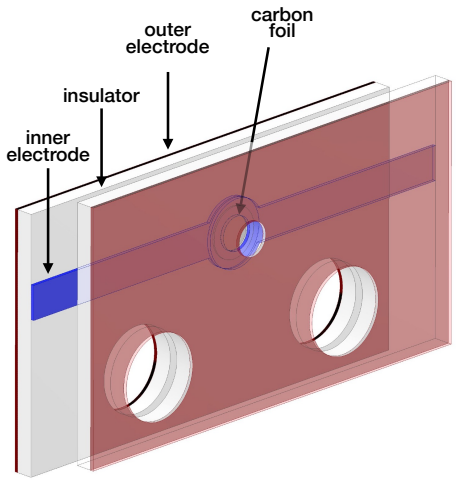

Figure 3.11: Schematics of the PCB electrodes that are used to sandwich the carbon foil. The different color of the inner and outer electrodes serves only to distinguish them in the figure. The foil is sandwiched between the inner electrodes of the two PCB's, which are then set to an attractive potential. One of the outer electrodes serves as an additional focusing/collimation electrode. The two drillings on the lower part are used to mount the electrodes on ceramic bushings.

for the energy determination) and carbon-nano-membranes[9] (mainly used for preparatory mesurements). Both foil types are supported by a TEM grid (made from gold or copper). The kinetic energy of the ion bunches, typically around $q \cdot 15$ eV (q being the charge state of the ion), is not sufficient for the ions to transit the carbon foils. Therefore the ions are accelerated onto the foil with typically -300 V, which leads to a kinetic energy of $q \cdot 315$ eV as the ions transit the foil.

The foil is sandwiched between two double-sided Cu cladded printed circuit boards (PCB), each with a thickness of 0.5 mm. The front side of the PCB (facing the incoming ions) serves as an electrode and provides additional control over the ion beam as it is accelerated towards the foil. The setup is shown in Fig. 3.11.

The PCB boards are placed between the ion extraction part and the spectrometer part of the experimental setup. The PCB boards are held in place by ceramic bushings[10], which are directly mounted to the lower part of the magnetic bottle

[9] CNM technologies Bielefeld GmbH.

[10] Vitronit supplied from Vitron GmbH.

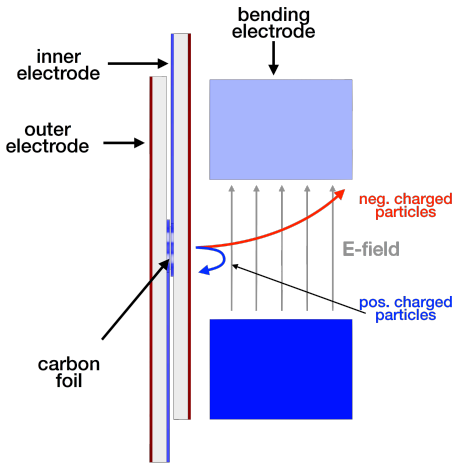

Figure 3.12: Schematics of the PCB electrodes that are used to sandwich the carbon foil. The foil is sandwiched between the inner electrodes of the two PCB boards which are then set to an attractive potential. One of the outer electrodes serves as an additional focusing/collimation electrode.

spectrometer.
In order to prevent charged particles from entering the electron spectrometer, bending electrodes are placed between the carbon foil and the spectrometer entrance. The bending electrodes are typically set to +300 V and +1000 V. These voltages are selected for several reasons: First, the voltage gradient is approximately 1 kV/cm, which additionally leads to a deflection of charged particles. Secondly, the potential in the center between the two electrodes is at +650 V (= (300 + 1000)/2 V). This leads to a repelling force on positively charged particles that leave the carbon foil (either sputtered ions or not fully neutralized $^{229(m)}$Th ions). Third, low-energy secondary electrons that are potentially generated by the impact of particles on the bending electrodes are energetically not able to enter the spectrometer (which is connected to ground).

3.4 IC electron collection region

The atoms that are generated in the ion neutralizer (see section 3.3) continue their flight towards the magnetic bottle electron spectrometer. As discussed in section 3.2, only electrons that are emitted in a small volume (a sphere with radius ≈1.5 mm) above a strong permanent magnet are guided towards the retarding field

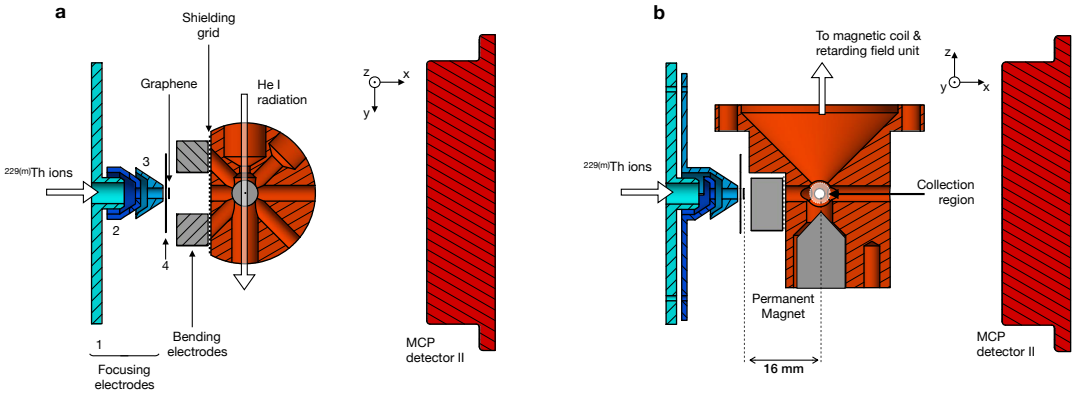

Figure 3.13: Detailed view of the electrode arrangement of the neutralization region and the electron collection region of the magnetic bottle spectrometer. **a** shows the sectional view in the x-y plane (with x being the beam direction). **b** shows the x-z plane (with the magnetic bottle spectrometer oriented in the z-direction). Figure is taken from [1].

analyzer and can thus be measured with the magnetic bottle spectrometer.
In order to achieve a high energy resolution electric stray fields and surface potential differences need to be minimized. Therefore the electron collection region has been designed as shown in Fig. 3.13. The manufacturing process and the motivation for this design will be detailed in the following. The collection region is manufactured from two cylinders of aluminum, which are connected by precision dowel pins throughout the whole manufacturing process and operation of the spectrometer. After manufacturing of the internal structure of the cylinders (see below), the two parts were separated and the surfaces that face the electrons were gold-coated for a proper reduction of surface potential differences.
There are four through-going drilled channels in the horizontal (x-y) plane, centered at the contact point of the two aluminum cylinders and one in the vertical (x-z) plane. The four horizontal channels create eight access ports to the collection region: the atoms can enter through one port and exit through another. Two ports are used for calibration: one port allows the deep ultra-violet (DUV) radiation to enter and exit the collection region. The drill hole at the exit port for the DUV radiation is larger in diameter in order to reduce stray electrons. One port was intended to supply the calibrant gas. It was found, however, that the mere

leaking of calibrant gas into the vacuum chamber was already sufficient to create a reasonable photoelectron signal for calibration. The ports were also intended for a proper venting of the collection region in order to prevent accumulation of calibrant gas.
The vertical drill holes serve two purposes. One marks the entrance to the retarding field analyzer and the solenoid. The other serves as a mount for the strong permanent magnet. Special care was taken that the magnet is completely "out-of-sight" for the DUV radiation and atoms making their way through the electron spectrometer.
The channels generate a fairly large "material free" volume above the permanent magnet. This reduces secondary electrons generated from atoms hitting walls and be able to enter the spectrometer to a negligible fraction (see Sect. 6.2.1).
It has been found that the electric field generated by the bending electrodes (see section 3.3) influences the energy resolution of the spectrometer. Therefore, the atom entrance port (facing the bending electrodes) was additionally terminated with a copper mesh (denoted as 'Shielding grid' in Fig. 3.13).

CHAPTER 4

Preparatory Measurements

This chapter discusses preparatory measurements that were performed to characterize and validate the experimental setup that was used throughout this thesis.

4.1 Performance of the RFQ buncher

The performance (*i.e.* the time-of-flight width and the number of particles per bunch) of the RFQ buncher has been tested in several measurements. One bunch cycle is made up of four phases. The voltage settings for the RFQ for the different phases are shown in Fig. 4.1. Note that the source voltage as well as the DC-slope of the RF and DC funnel are not shown in this figure in order to put the focus on the RFQ DC-voltages. The flow cycle phases are:
(i) ions are loaded into the trap. The source voltage is set to extraction and the last RFQ segment is set to trapping (left panel of Fig. 4.1). Typically they are set to +34 V.
(ii) ions are cooled in the trap region. The source offset voltage is switched to a voltage where ion extraction is stopped (0 V).
(iii) ions are released from the trap region. The last RFQ segment is switched within a microsecond to 0 V (right panel of Fig. 4.1).
(iv) In a final step, the last RFQ segment is ramped to the trapping voltage, while the source is still switched off.
Each state is held for a defined time (t_{load}, t_{cool}, t_{rel} and t_{rest}), respectively.

The operational parameters of the RFQ buncher have to be chosen such that a large number of ions is obtained within a short time window. Typical ion bunch shapes are shown in Fig. 4.2.
The number of ions per bunch is affected by the loading rate and loading time, as

well as by the ion trapping capacity of the ion trap that is generated in the last RFQ segments. The trapping capacity is defined by the interplay of the RF voltage amplitude, which confines the ions radially, and the DC potential difference of the trapping segments, which is used for axial confinement. A measurement of the number of particles as a function of the loading time is shown in the left panel of Fig. 4.3. It is clearly visible that the trap is already saturated after a loading time of 300 to 400 ms. As there is no mass purification prior to loading, all charge states and daughter nuclei of the ^{233}U source are loaded into the trap at a rate of ≈20 000 ions per second (ca. 10 000 $^{229}Th^{3+}$, 5 000 $^{229}Th^{2+}$ and 5 000 $^{233}U^{2+}$ [106]). Therefore, the maximum trapping capacity is reached very fast.
The width of the temporal bunch profile is influenced by several factors:
First, the spatial extent of the ion cloud needs to be as small as possible. Second, the ion bunch needs to be cooled before it is ejected in order to reduce the relative velocity of the ions in the bunch. Third, in the ejection phase, the last RFQ segment needs to be ramped to a low voltage as fast as possible.

At first the cooling time, trapping voltages and buffer-gas pressure in the RFQ were adjusted, reaching a time-of-flight width of ≈10 μs which was used in the lifetime measurements. In a second step, the electronics of the buncher unit was optimized leading to a time-of-flight width of ≈6 μs (used in the energy measurements). A comparison of optimized (width ≈ 6 μs) and non-optimized (width ≈ 10 μs) bunch shapes is shown in Fig. 4.4. This was achieved by adapting the resistors in the RFQ buncher circuit shown in Fig. 3.5. By additionally including a kicking electrode (*i.e.* raising the offset voltage of the 10$^{\text{th}}$ segment shortly before releasing the ion bunch) bunch widths of 600 ns (FWHM) were achieved (as shown in the right panel of Fig. 4.3). These short ion bunches were, however, only achieved at the cost of a low number of ions per bunch. Therefore, for the measurements presented in the following bunches were generated with widths of 10 μs (for the lifetime measurements presented in chapter 5) or 6 μs (for the energy measurements discussed in chapter 6).
During all measurements, the loading time was set to 70 ms, which results in the optimum number of extracted ions per second.

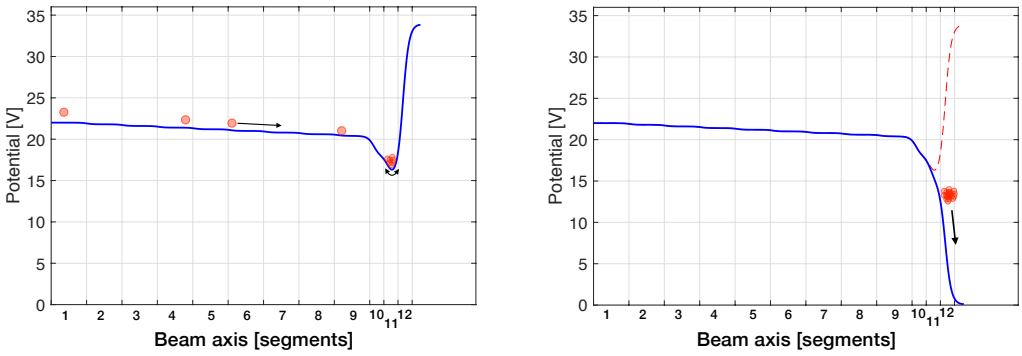

Figure 4.1: DC potentials along the central axis of the RFQ (blue lines). The potential values were calculated with SIMION. The applied voltages are given for an offset of 21.8 V and a trapping voltage of 15 V (as listed in Table C.1). The left panel shows the DC slope for loading and cooling of the ion bunch. The DC potentials for the release of the ions is shown in the right panel (the red dashed line displays the trapping potential in contrast to the release phase). Prototypical ions are shown as red circles.

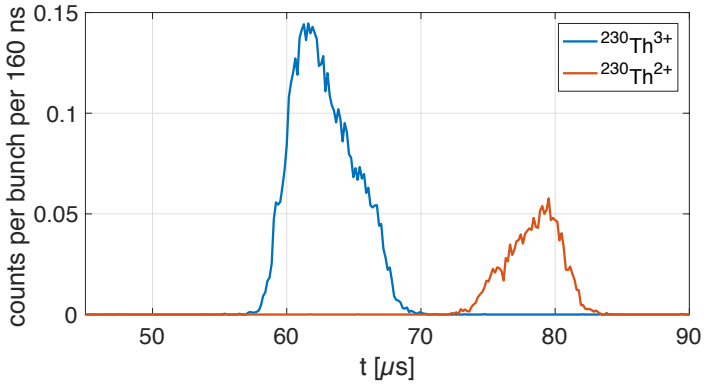

Figure 4.2: Typical bunch shapes. Measurements were performed with ^{230}Th ions. A clear separation in the time of flight between the two charge states can be obtained.

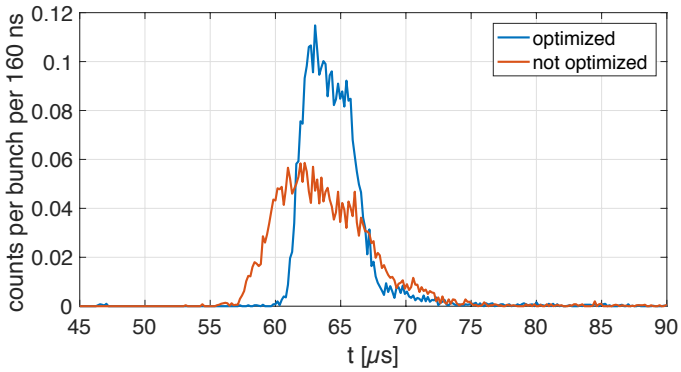

Figure 4.4: Comparison of the bunch shapes before (red) and after optimization (blue) of the buncher electronics. Measurements were performed with $^{229m}Th^{3+}$ ions.

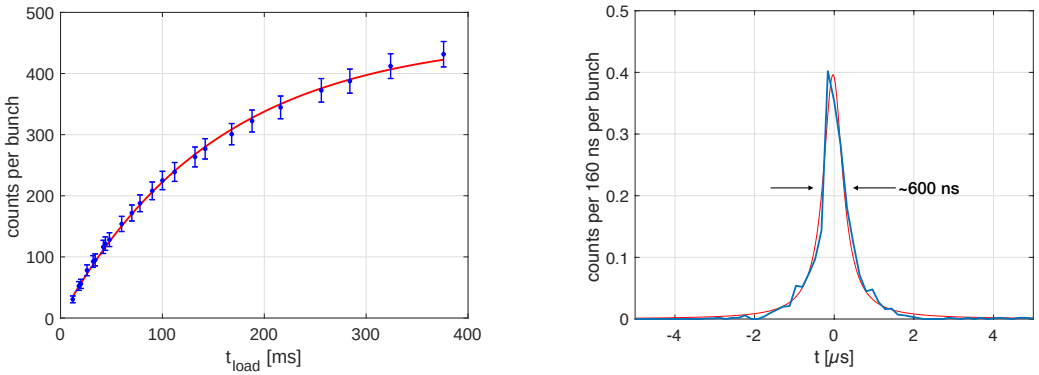

Figure 4.3: Left: the number of counts per ion bunch as a function of the loading time t_{load} with $t_{\mathrm{cool}} = t_{\mathrm{rel}} = t_{\mathrm{rest}} = 10$ ms. The red line serves to guide the eye. Right: Measured bunch with a time-width of 600 ns (FWHM). The red line is a Lorentzian which was fitted to the measured bunch shape.

Calibrant	Ionizing radiation	Final state		Kinetic energy [eV]
Ar	He Iα	$^2P_{3/2}$		5.459
		$^2P_{1/2}$		5.281
Ne	He Iβ	$^2P_{3/2}$		1.522
		$^2P_{1/2}$		1.425
N_2	He Iα	X $^2\Sigma_g^+$	$v = 0$	5.64
		A $^2\Pi_u$	$v = 0$	4.51
			$v = 1$	4.28
			$v = 2$	4.05
			$v = 3$	3.83
			$v = 4$	3.61
		B $^2\Sigma_u^+$	$v = 0$	2.47

Table 4.1: List of the photoelectron lines generated with a He discharge lamp and different calibrant gases. These lines were used for the calibration and characterization of the magnetic bottle spectrometer.

4.2 Performance & calibration of the magnetic bottle spectrometer

The electron spectrometer is calibrated with a sample gas and a helium discharge lamp[1]. Calibration of the spectrometer is needed in order to correct for surface potential differences. These lead to systematic shifts (*i.e.* the applied blocking voltage does not correspond to the potential which is experienced by the electrons) which need to be quantified and corrected for in the analysis. In all the measurements that are shown, the blocking voltage is directly corrected for surface potential shifts which typically amount to -0.5 V. For calibration, the calibrant gas is fed into the vacuum chamber via a piezo valve. Measurements are typically performed at a gas pressure of 3×10^{-5} mbar. The mainly used calibrant gas is argon (Ar). When He Iα radiation is used ($E_\gamma = 21.22$ eV), the photoionization process in the argon atom leads to the emission of electrons with two kinetic energies (5.29 eV and 5.46 eV, see Table 4.1), which serve as calibration points.
As the kinetic energies of the internal conversion electrons are expected to lie in

[1]Specs GmbH, UVS 10/35.

the region around E_I−IP= 1.5 eV (under the assumption of E_I = 7.8 eV [31]), the spectrometer is also calibrated with neon as a calibrant providing photoelectrons in the relevant energy range. The lines that were used with neon can be found in Table 4.1. Neon can only be ionized by He Iβ (E_γ = 23.09) radiation, which is emitted with only 1.5% of the He Iα intensity. Therefore, a considerable background due to stray light and secondary electrons is visible in the right panel of Fig. 4.6, which displays the corresponding calibration measurements.
For these measurements the retarding (or blocking-) voltage is ramped continuously between two fixed values (in a time period of about 2 s to 4 s). Photoelectron counts are measured in time bins of typically 1 ms to 2 ms. The time bins are then translated to voltage bins (for details see [114]). Data is re-binned and smoothed with a moving average filter (averaging over 3 bins). The raw data is shown with red dots, the re-binned and averaged data is shown in solid red (note that the raw data coincide with the processed data in the argon measurement). Because only electrons are counted which have sufficient energy to overcome the applied blocking potential, an "integrated' spectrum is generated, where lines appear as edges. In order to generate demonstrative plots which make it easier to assess the energy resolution, the derivative ($-\frac{N_{i+1}-N_i}{V_{i+1}-V_i}$, where N_i is the number of counts in the i'th bin at a blocking voltage V_i) is formed from the smoothed data. The derivative as well as a fit to the derivative data is shown in black.
Measurements with air leaked in the spectrometer chamber have also been performed. The spectra are dominated by nitrogen (N_2). The corresponding spectra are shown in Fig. 4.7. The vibrational spectrum of the N_2^+ $A^2\Pi_u$ state (with kinetic energies between 3.83 eV and 4.51 eV, see Table 4.1) has been resolved. The vibrational frequency has been measured to 0.227±0.017 eV, which is in good agreement with the value 0.229 eV that is calculated with the Dunham coefficients found in [120].
The nitrogen spectrum clearly demonstrates the linearity of the spectrometer over a wide range of energies (from 2.5 eV to 5.6 eV) [114].

4.2.1 Energy resolution

As shown above and in section 2.5.2, the energy resolution depends on the ratio of the magnetic fields in the region of the electron collection (B_i) and in the solenoid (B_f). The behaviour of the spectrometer operated with different magnetic field ratios is demonstrated using the neon lines. While the magnetic field in the collection region ($B_i \approx 200$ mT) stays constant, the magnetic field strength in the coil can be controlled via the applied current. A corresponding measurement series with $B_f = [1, 2, 3, 4]$ mT is shown in Fig. 4.8. A clear influence on the

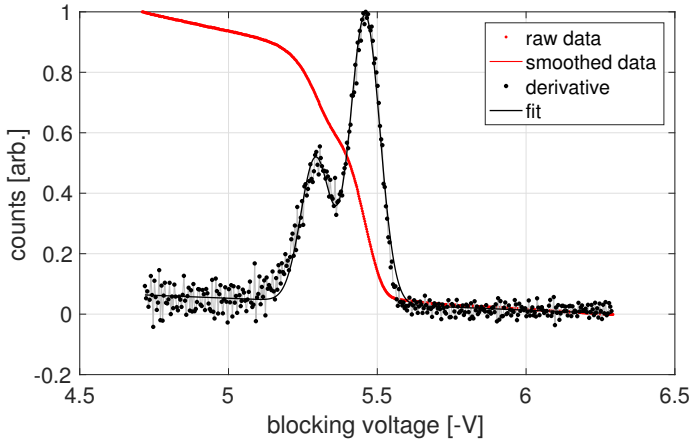

Figure 4.5: Calibration measurements performed with argon. The raw data is shown with red dots and the smoothed and rebinned data in solid red. Note, that the raw data and smoothed data are nearly indistinguishable. The derivative of the smoothed data (black dots) is used to fit two gaussians (shown as black lines). Data is normalized to its respective maximum and the blocking voltage is already corrected for surface potential differences. Figure is taken from [114].

energy resolution has been measured. Additionally, it is found that the electron count rate increases with B_f and reaches a plateau at $B_f \approx 1.5$ mT.

The relative energy resolution of the spectrometer is found to be better than 3% (FWHM). This value results from measurements that were performed with argon and neon.

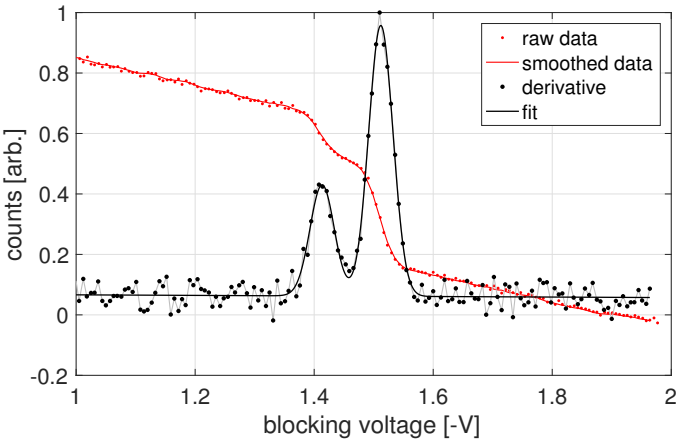

Figure 4.6: Calibration measurements performed with neon. The figure is labeled and generated as Fig. 4.5. Figure is taken from [114].

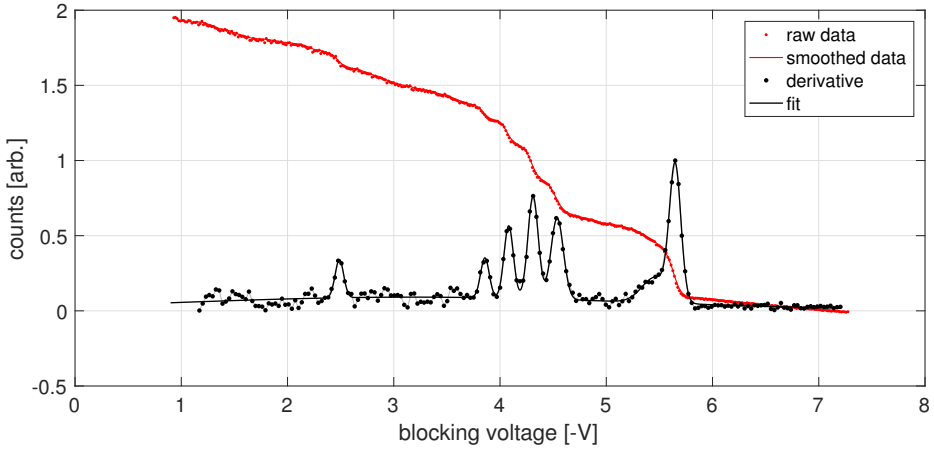

Figure 4.7: Calibration measurements with nitrogen as calibrant gas. The raw data is shown with red dots. The smoothed and rebinned data is is plotted as a red line. Derivatives are again shown in black. Figure is taken from [114].

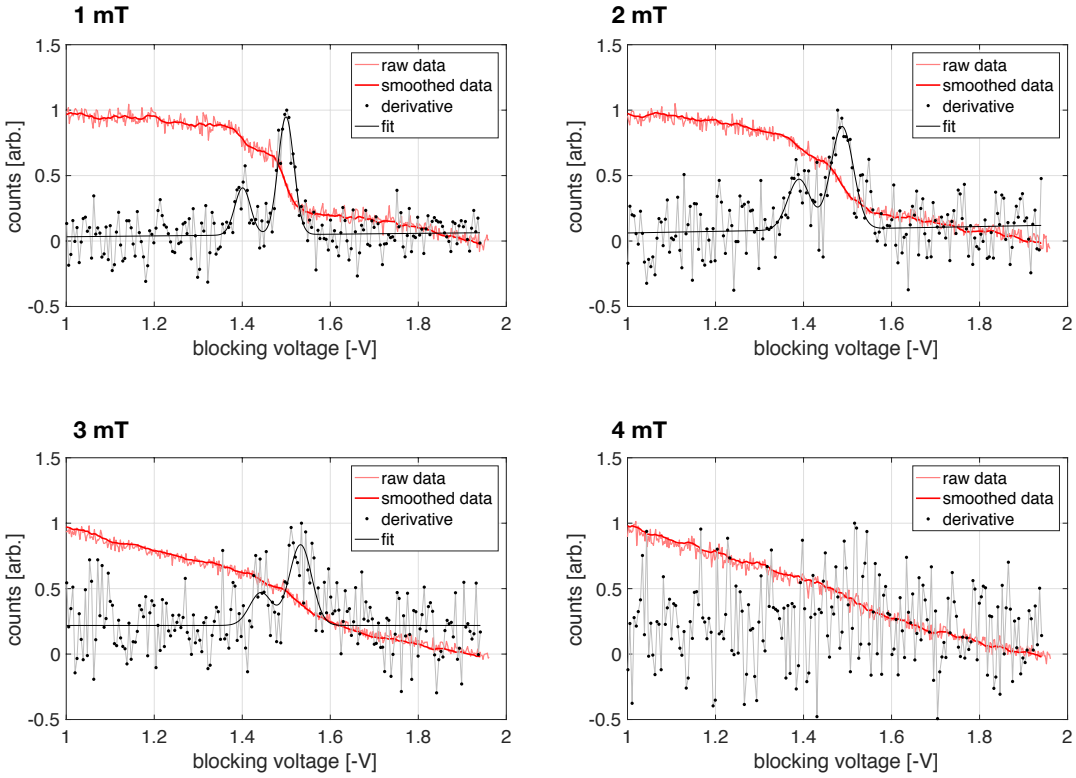

Figure 4.8: Electron spectra recorded with different magnetic field strengths in the transport coil of the electron spectrometer. The light red curves show the raw data, the dark red curve shows the smoothed and re-binned data. The black dots show the derivative of the smoothed data and the black curves show the gaussian fits. The FWHM (full width at half maximum) of the peaks increases from 42±1 meV (at $B_f = 1$ mT) to 70±20 meV (at $B_f = 3$ mT). The measurements that were performed with 4 mT do not show any resolvable lines.

4.3 Neutralization of ions

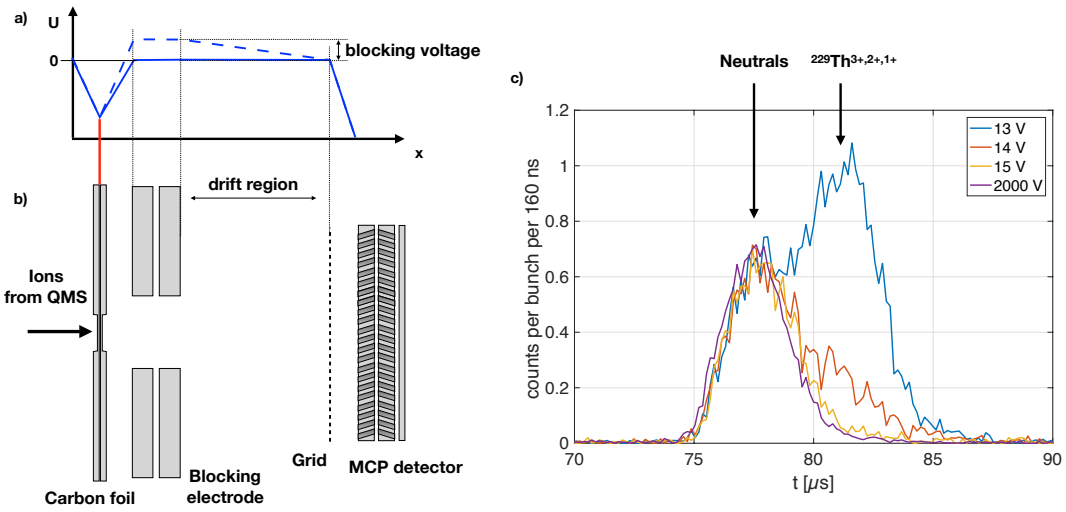

Figure 4.9: a) Potential slope of the experimental setup which is sketched in b). Ions are accelerated onto a carbon foil where some of them neutralize. The (neutralized) atoms keep the velocity they have at the point of neutralization, while the ions are slowed down by electric potentials. A blocking voltage applied to a ring electrode allows to completely suppress ions, while neutrals are unaffected. c) Time-of-flight spectra of ions and atoms produced from $^{229(m)}Th^{3+}$ ions incident on a carbon foil for different applied blocking voltages.

An efficient way to neutralize slow ions is by charge exchange in an ultra-thin carbon foil (a bi-layer of graphene or carbon nano membranes supported on a TEM grid were used). As the ions transit the foil they grab electrons. The exiting charge state distribution depends on the ion's velocity.
The charge state distribution can be obtained by considering electron capture and electron loss cross sections. These are, however, difficult to obtain for which reason there are several semi-empirical models which allow to calculate equilibrium charge states of ions traversing matter. An overview of different models and their limitations can be found for example in Ref. [121]. The equilibrium exit charge state q_{exit} can be estimated by Bohr's velocity criterion:

$$q_{\text{exit}} = Z^{\frac{1}{3}} \cdot \frac{v}{v_0}, \tag{4.1}$$

where Z is the proton number of the ion passing the foil and v_0 Bohr's velocity (given with $\alpha \cdot c = (299792458/137)\ \frac{m}{s} = 2.2 \times 10^6 \frac{m}{s}$). For ion velocities which are slow compared to v_0, it can be expected that the majority of the ions exits the foil as neutrals. Measurements of the charge state distribution are presented in the following. In the measurements the carbon foil is set to an attractive potential U_{foil} and ions extracted from the buffer-gas stopping cell are guided and accelerated towards the foil. The kinetic energy at the point of neutralization is

$$E_{\text{foil}} = q_{\text{in}} \cdot U_{\text{foil}} + E_0, \tag{4.2}$$

with q_{in} as the charge state of the incoming ion and E_0 the initial kinetic energy of the ions (in the experiments E_0 is typically $q \cdot 15$ V, as the ion bunches are stored at +15 V). Therefore, when the ions are decelerated by a potential U_{del} after charge exchange, they lose kinetic energy (ΔE) depending on their outgoing charge state (q_{out})

$$\Delta E = q_{\text{out}} \cdot U_{\text{del}}. \tag{4.3}$$

Ions that enter a drift region or a spectrometer (after charge exchange) which is set to ground (*i.e.* $U_{\text{del}} = U_{\text{foil}}$) have a kinetic energy of

$$E_{\text{kin}}(q_{\text{in}}, q_{\text{out}}) = (q_{\text{in}} - q_{\text{out}}) \cdot U_{\text{foil}} + E_0. \tag{4.4}$$

This allows to measure the charge state distribution of the exiting ions in two different ways (which are detailed in [101]).
In a first setup an MCP detector was placed in the beam axis behind the carbon foil as shown in Fig. 4.9. In order to prevent charged particles from reaching the MCP, two blocking electrodes (which are kept on the same potential) were placed between the foil and the MCP. In order to achieve a high detection efficiency for positively charged ions, the MCP surface was set to an attractive negative potential (-2 kV). The MCP surface was shielded with a gold grid which was kept on ground potential. In this way, a nearly field-free drift region is established. The potential along the beam axis is shown qualitatively in Fig. 4.9a. The solid blue line shows no applied blocking voltage and the dashed blue line shows the situation with a blocking voltage applied to the blocking electrodes. While the atoms keep the velocity of the ions during charge exchange, the charged particles are decelerated by the blocking voltage and therefore enter the drift region with lower kinetic energy. This allows to separate the charged particles from the neutralized particles by their time-of-flight, as shown in Fig. 4.9c. For different blocking voltages, the ions can be hindered from entering the drift region and reaching the detector depending on their kinetic energy. A measurement series performed with different blocking voltages, shown in Fig. 4.9c, demonstrates the complete

suppression of charged particles. In these measurements it could be concluded that the ions can be efficiently neutralized. The large fraction of 3+→3+ (and also 2+→2+, not shown in Fig. 4.9c) is due to holes in the carbon foil (*i.e.* ions that do not interact with the foil and therefore do not undergo charge exchange). The charge exchange from (3+→2+ or 3+→1+) cannot be unambiguously identified with this setup.

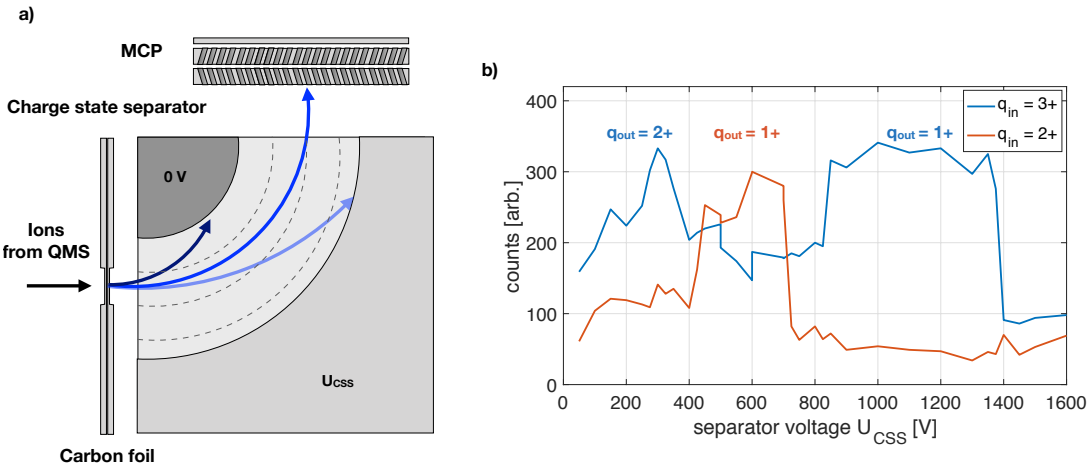

Figure 4.10: The charge state separator that was used to analyze the charge state distribution of $^{229(m)}$Th ions after transiting a carbon foil is shown in the left panel (a). A corresponding measurement is shown in the right panel (b). The charge states can be assigned by comparing the measurement with SIMION simulations.

In order to measure a full exit charge state distribution, a setup based on a charge state separator (CSS) was used. The CSS is comprised of a curved capacitor and was placed behind the carbon foil, as visualized in Fig. 4.10a. The trajectory of the ions in the CSS depends on the voltage that is applied between the two plates, so that only ions with a certain kinetic energy can reach the MCP detector. In the measurements presented in Fig. 4.10b, one plate was kept on ground, while the voltage applied to the other plate was varied. These measurements clearly show distinct peaks which can be attributed to $(q_{\mathrm{in}}, q_{\mathrm{out}})$-pairs in comparison with SIMION simulations. Further details can be found in [101].
It was possible to measure charge exchange to lower charge states (3+→2+, 3+→1+ and 2+→1+). It was found that only a minor fraction of the ions that

undergo charge exchange exits the foil in the charge states 1+ or 2+. The $q_{\mathrm{out}} =$ 1+ charged state is only populated with 0.10±0.04 % .

In a combined analysis of both measurements (charge state separator and time-of-flight separation) [101] it could be shown that 63±10 % of the ions exit the foil as neutral atoms, thus proving efficient neutralization in the carbon foil.

CHAPTER 5

Lifetime Measurements

In the following chapter lifetime measurements of ^{229m}Th undergoing internal conversion decay are described. The general concept of the lifetime measurements is to exploit the expected huge difference in the lifetime between the radiative and the internal conversion decay channel: while the lifetime of the radiative decay channel is expected in the order of 10^3 to 10^4 s [5–7], the internal conversion decay channel was expected to be reduced by about 9 orders of magnitude, thus ending up in the microsecond range. Due to the low energy of the isomeric excitation excitation, internal conversion is forbidden in charged ^{229m}Th (since the first ionization potential of Th^{1+}[33] is larger than the isomeric energy) and therefore the isomer stays long-lived as long as it is in a charged state. This in turn makes it possible to trigger the internal conversion decay by neutralizing the ion. The corresponding experimental setup is described in detail in chapter 3 and again shown in Fig. 5.1: A 2% decay branch in the ^{233}U α decay populates ^{229m}Th. A fraction of the energy, which is set free in this α decay, is converted to kinetic energy and $^{229(m)}$Th is emitted from the solid source as a multiply charged ion. The ions are thermalized in He buffer gas in a buffer-gas stopping cell and an ion beam is formed, which is subsequently converted into ion bunches in an RFQ cooler and buncher. These ion bunches are then mass-purified in a quadrupole mass separator. Subsequently, the ion bunches are collected directly on the surface of an MCP detector, where they neutralize. After neutralization, it is energetically allowed for ^{229m}Th to decay via internal conversion and the thereby emitted IC electron can be detected with the MCP detector.

The internal conversion electron activity can generally be described with

$$A_{\mathrm{IC}}(t) = \lambda_{\mathrm{IC}} N_0 \exp\Big[\sum_i \lambda_i t\Big], \tag{5.1}$$

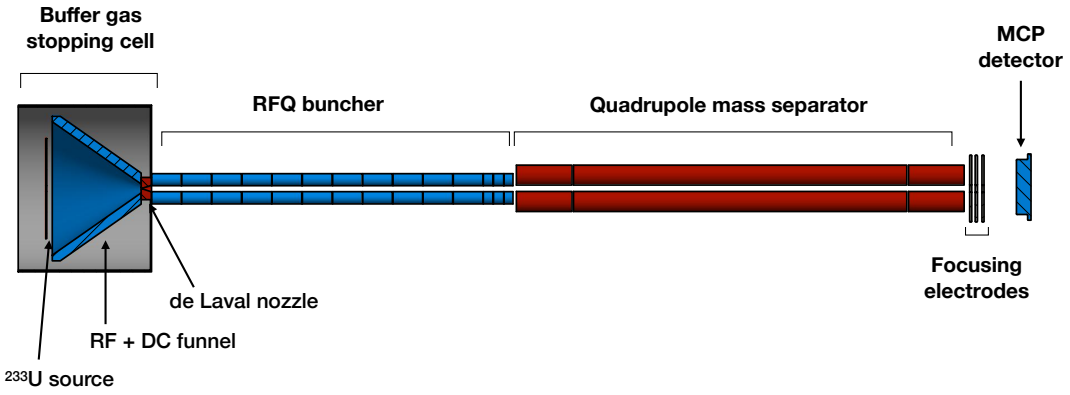

Figure 5.1: Schematic of the experimental setup that is used in the lifetime measurements (as detailed in chapter 3). $^{229(m)}$Th ions are extracted from a ^{233}U source in a buffer-gas stopping cell. Ion bunches are formed in an RFQ buncher and mass purified in a quadrupole mass separator. The ion bunches are collected directly on an MCP detector, where they neutralize and the subsequently emitted IC electron is detected.

where λ_{IC} is the decay constant for the IC decay, N_0 is the number of excited Th nuclei under investigation and λ_i denotes all decay constants of all possible decay channels (including γ decay, internal conversion, or other decay channels that may lead to a depletion of the isomer). For neutral $^{229\mathrm{m}}$Th it can be expected that $\sum_i \lambda_i \approx \lambda_{\mathrm{IC}}$, since the IC decay channel can be expected to be by far the strongest. This leads to

$$A_{\mathrm{IC}}(t) \approx \lambda_{\mathrm{IC}} N_0 \exp\left[\lambda_{\mathrm{IC}} t\right] \tag{5.2}$$

for the IC electron activity. This means that performing a time-resolved measurement of the IC electron activity of neutral $^{229\mathrm{m}}$Th allows to determine λ_{IC} and thus the lifetime of the internal conversion decay channel of the isomeric state in ^{229}Th.

This chapter is organized as follows: In order to get a first idea what types of signal to expect, simulations have been performed, which are described in section 5.1. Here also the sensitivity of the approach is investigated. The final measurements together with comparative measurements are shown in section 5.2.

In a last section (section 5.3) the influence of the electronic environment on the lifetime of ^{229m}Th is investigated qualitatively, which can serve as a starting point for future studies in this direction.

Isomer lifetime:	variable
Branching ratio (BR):	2%
Detection efficiency for IC electrons (ϵ_e):	1%
Detection efficiency for ions (ϵ_i):	0.1%
Number of ions per bunch (N_{bunch}):	200
Repetition rate (R):	variable
Dark count rate (D):	10 cts/s
Measurement time (T):	variable
Bin size (t_{bin}):	variable

Table 5.1: List of input parameters that are used in the simulations. The parameters are described in detail in the text.

5.1 Simulations: expected signal and limitations

The feasibility of lifetime measurements in the internal conversion channel of $^{229\text{m}}$Th was studied with MatLab based simulations (the central code is listed in Appendix A). In these simulations it was possible to input an arbitrary bunch shape and study the strength of the isomeric decay with different lifetimes and detection efficiencies. The parameters that influence the measured IC count-rate and are used as input parameters for the simulations are shown in Table 5.1. A goal of the simulations was not only to get an idea of the signal shape that can be expected, but also to explore the limits of this approach with our setup. Therefore different lifetimes were simulated. In Fig. 5.2 the expected signals for two different exemplary lifetimes are shown ($t_{1/2} = 1$ μs and $t_{1/2} =$ 100 ms) together with the bunch shapes that served as input. The plots in Fig. 5.2 illustrate the limiting factors of the approach: For long lifetimes the IC electron rate is very low[1] and the measurement is limited by detector noise, the extraction rate and the detection efficiency. On the other hand, high count rates can be expected for short lifetimes, and in this case a lifetime measurement is only limited by the bunch shape.

[1]The IC electron rate is proportional to $\lambda_{IC} = \ln(2)/t_{1/2}$.

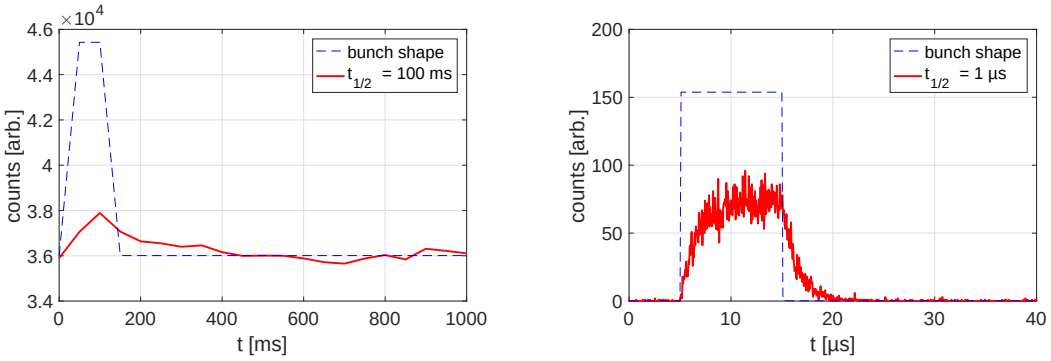

Figure 5.2: Simulation of two different lifetimes $t_{1/2} = 100$ ms (left) and $t_{1/2} = 1$ μs (right). The simulated IC electron activity is plotted in red. In both simulations the measurement time was chosen as 10 h. The repetition rate has been adapted to the lifetime and was set to 10 Hz for $t_{1/2} = 1$ μs and 1 Hz for $t_{1/2} = 100$ ms (bin size 50 ms). Since reducing the repetition rate allows for longer loading times which leads to a higher number of ions per bunch (as shown in sect. 4.1), the number of ions per bunch for the long lifetime has been set to 400 (instead of 200 ions per bunch for the 10 Hz repetition rate).

5.1.1 Upper limit of the approach

For long lifetimes the limiting factors are the detector noise, the extraction rate and the detection efficiency. The maximum number of measured IC electrons in a time bin of length t_{bin} is given by

$$S = \epsilon_e \cdot \frac{\ln(2)}{t_{1/2}} \cdot \mathrm{BR} \cdot N_{\mathrm{bunch}} \cdot R \cdot T \cdot t_{\mathrm{bin}}, \tag{5.3}$$

where ϵ_e is the detector's electron detection efficiency, $t_{1/2}$ is the isomer IC half-life, BR the branching ratio of the ^{233}U α decay to the isomeric state, N_{bunch} is the total number of ions per bunch (making BR$\cdot N_{\mathrm{bunch}}$ the number of isomers per bunch). R is the repetition rate of the ion buncher and T is the total measurement time (this makes $R \cdot T$ the total number of collected ion bunches). Typical values are given in Table 5.1. This count rate competes with the dark counts per time bin given by

$$B = D_R \cdot R \cdot T \cdot t_{\mathrm{bin}}, \tag{5.4}$$

where D_R is the dark-count rate. With the above equations it is possible to estimate the maximum measurable lifetime with the considered setup. Considering a bin size equal to one half of the half-life ($t_{\mathrm{bin}} = 0.5 t_{1/2}$) and the repetition rate

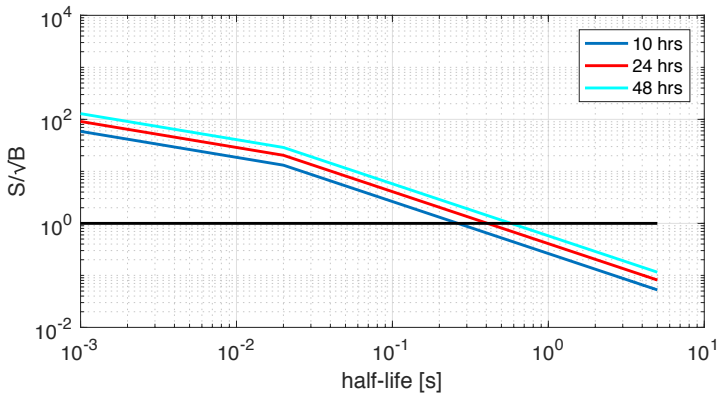

Figure 5.3: Signal-to-noise ratio plotted against the half-life for different measurement times. The kink visible at $t_{1/2} = 0.02$ s results from the fact that the maximum buncher repetition rate is chosen to be $R = 10$ Hz (resulting in an optimum number of ions per bunch, see chapter 3). If the lifetime is longer than one buncher cycle, that rate is chosen to be at least the inverse of 5 half-lives: $R = 1/(5t_{1/2})$.

being equal to the inverse of 5 half-lives ($R = 1/(5t_{1/2})$), it is possible to calculate the signal-to-background ratio:

$$\frac{S}{\sqrt{B}} = \epsilon_e \cdot \mathrm{BR} \cdot \ln(2) \cdot N_{\mathrm{bunch}} \cdot \sqrt{\frac{0.1 \cdot T}{D t_{1/2}}}. \tag{5.5}$$

In order to properly measure the half-life, it is useful to measure over a period of at least two half-lives. Therefore, also a quarter of the maximum signal should be measurable. According to Eq. (5.5) a quarter of the signal-to-noise ratio is plotted against the half-life in Fig. 5.3 for different measurement times. It can be shown that for the given count rates, efficiencies and branching ratios half-lives of up to ≈0.5 s are measurable within a reasonable measurement time of 48 h.

5.1.2 Lower limit of the approach

For short lifetimes the shape of the ion bunch poses the limit, since signals originating from the impact of the ions cannot be completely suppressed. A rectangular shape as used in the simulations cannot be expected in the measurements, and the falling edge of the bunch may overlap with the isomeric decay signal. In order to further study such a behavior, a measured bunch shape (of ^{233}U ions)

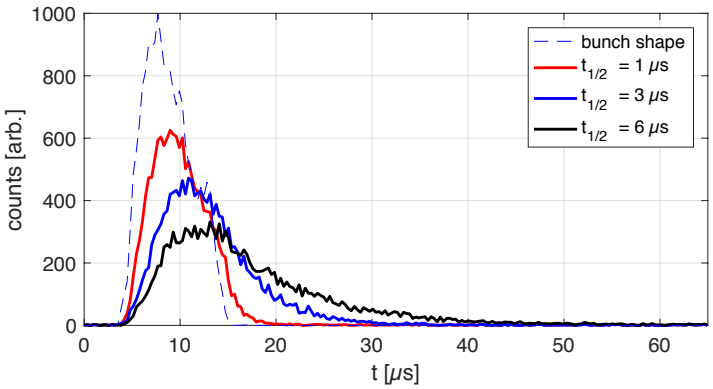

Figure 5.4: Simulation of a signal with different half-lives. Also the shape of the bunch is indicated. The total measurement time was 10 hours and the bin size was taken to be 320 ns.

was used and different half-lives (1 μs, 3 μs and 6 μs) were simulated. These simulations are shown in Fig. 5.4. From the simulations it becomes clear that whenever the half-life of the isomer is larger than ≈ 3 μs it can be easily separated from the bunch. In the real measurement it is not possible to distinguish between a signal originating from the ionic impact or a signal which is generated by the isomeric decay. It is possible, however, to reduce the detection efficiency for ions by reducing the kinetic energy of the ions. This allows to identify signals that originate from ionic impact (see section 5.2.1).

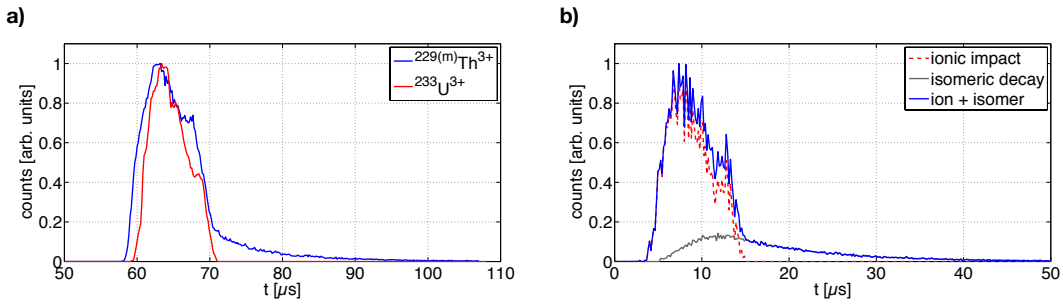

Figure 5.5: Measured data (a) compared to an adapted simulation of triply charged ions (b). The measurements also show bunches that were recorded using ^{233}U ions (red curve, left panel). In the simulation, the ratio between the detection efficiencies is set to be $\epsilon_e/\epsilon_i = 25$ and the half-life was chosen as $t_{1/2} = 7$ μs.

5.2 Lifetime measurements of ^{229m}Th

In the following section the lifetime measurements of the internal conversion decay of ^{229m}Th are described [11]. For the lifetime measurements ion bunches of $^{229(m)}$Th were collected on an MCP detector (see chapter 3). An exemplary measurement with $^{229(m)}Th^{3+}$ and $^{233}U^{3+}$ ion bunches and an adapted simulation is shown in Fig. 5.5. In Fig. 5.5a) a clear signal from the accumulation of the ion bunches can be seen for both $^{229(m)}Th^{3+}$ and $^{233}U^{3+}$. For $^{229(m)}Th^{3+}$, however, also a signal remains after ion accumulation, whose origin can be unambiguously attributed to the isomeric decay (as shown in the next section). The ion bunches were generated at a trapping potential of +25 V. Therefore, when they impact onto the MCP surface, the ions have a kinetic energy of $(25 - U_{\text{front}}) \cdot q$ eV (where q is the charge state of the ion and U_{front} denotes the attractive MCP front surface potential). For these measurements the MCP surface voltage was set to -70 V, leading to an impact kinetic energy of 285 eV.

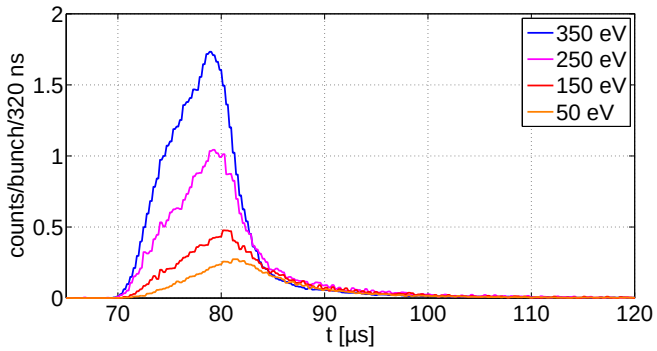

Figure 5.6: The measured counts for different kinetic energies of the ions. The counts are normalized to the number of bunches. The ionic impact signal can be clearly reduced by reducing the ion's kinetic energy, while the IC electrons signal remains constant.

5.2.1 Investigation of signal origin

The signal origin was investigated in several different ways, which are presented in the following. Since electrons resulting from the isomeric decay are produced on the MCP front plate, a variation of its potential should not affect the IC electron detection efficiency. The detection efficiency of the ions, however, depends drastically on their kinetic energy which is proportional to the potential applied to the MCP front surface U_{front}. To investigate the origin of the signal, the MCP front potential was varied while keeping the internal voltage gradients in the MCP detector constant. The corresponding measurement series is shown in Fig. 5.6, where U_{front} was varied between 0 V and −150 V (in steps of −50 V). The measurements were performed with $^{229(m)}Th^{2+}$, which leads to kinetic energies between 50 eV and 350 eV (in steps of 100 eV). While the signal that is attributed to the ionic impact can be reduced by a factor of ≈4, the signal strength from the decay signal stays constant.

Comparative measurements with ^{230}Th ion bunches have been performed to rule out a chemical origin of the decay signal. Data is shown in Fig. 5.7. In these measurements the ^{234}U source (described in chapter 3) replaced the ^{233}U source which is used for $^{229(m)}$Th extraction. The sources have comparable extraction rates for $^{229/230}$Th ions. Data for both sources was taken under identical extraction conditions. The MCP surface voltage was set to $U_{\text{front}} = -100$ V. The number of recorded bunches of $^{229(m)}Th^{2+/3+}$ and $^{230}Th^{2+/3+}$ was 20,000 and 10,000, respectively. Comparing the $^{229(m)}$Th with the ^{230}Th data, it becomes clear that a decay

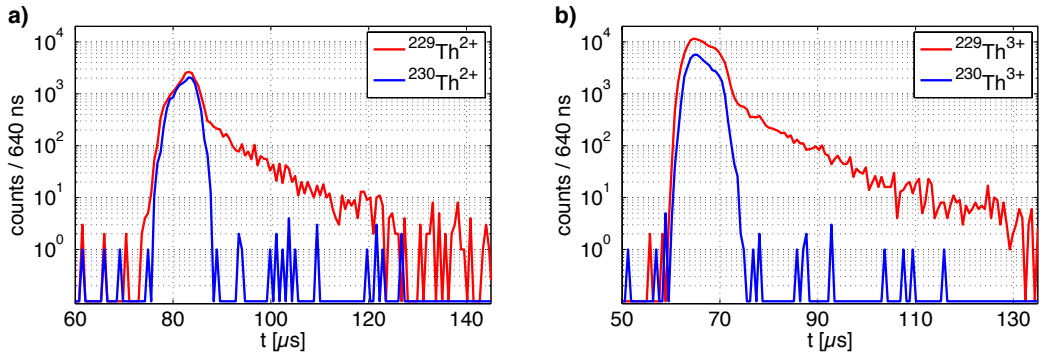

Figure 5.7: Comparative measurements that were performed with $^{230}Th^{2+,3+}$ ions (blue lines) and $^{229(m)}Th^{2+,3+}$ (red data). In order to visualize the baseline, bins containing zero counts were set to a value of 0.1 in the plots.

signal only remains for $^{229(m)}$Th.

The measurements shown in Figs. 5.5, 5.6 and 5.7, respectively, give unambiguous evidence that the decay signal which remains after ion accumulation must be attributed to the decay of $^{229(m)}$Th.

5.2.2 Lifetime determination

For the lifetime determination a linear function of the form $f(t) = -(1/\tau)t + c$ is fitted to the logarithm of the number of counts $N(t)$ which are detected after ion accumulation. The half-life can then be obtained via $t_{1/2} = \ln(2)\tau$. The data points were weighted according to the inverse of their relative error σ_{rel}, which is given by (under the assumption that the counts follow a Poisson distribution) $1/\sigma_{\mathrm{rel}} = N/\sqrt{N} = \sqrt{N}$. Fitting is performed for measurements that were conducted with $^{229(m)}Th^{2+}$ and $^{229(m)}Th^{3+}$ ion bunches and shown in Fig. 5.8. To obtain conclusive results, undistorted by any remaining ionic impact signal, the range for the fit was chosen to start ≈5 μs after the falling edge of the ionic signal. The fit range is indicated in Fig. 5.8. This results in half-lives of $t_{1/2} = 6.9 \pm 1.0$ μs and $t_{1/2} = 7.0 \pm 1.0$ μs for the measurements performed with $^{229(m)}Th^{2+}$ and $^{229(m)}Th^{3+}$ ion bunches, respectively. The uncertainty of ± 1.0 μs takes possible influences of the chemical environment into account, which was estimated to account to ≈ 10%.

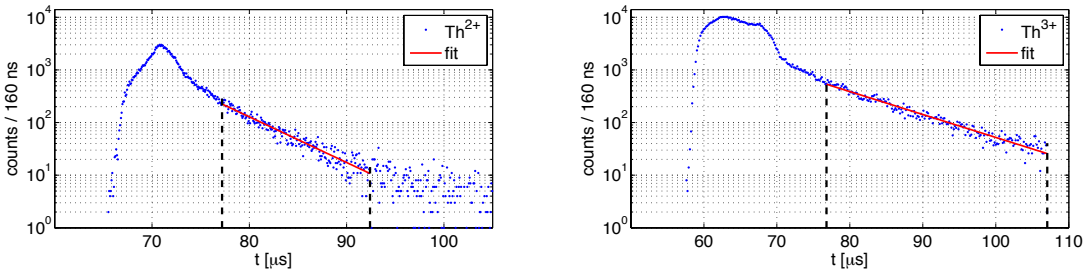

Figure 5.8: Data points as well as the fit function for $^{229(m)}$Th^{2+} (left) and $^{229(m)}$Th^{3+} (right) ion bunches. The fit range is indicated with vertical black dashed lines.

5.2.3 The absence of an isomeric decay in the singly charged state

Measurements were also performed with $^{229(m)}$Th^{1+} ions. In these measurements $^{229(m)}$Th^{1+} ion bunches with kinetic energies of 300 eV were collected on the MCP detector. No isomeric decay signal could be measured. For further investigation of the absence of an isomeric signal in the singly charged state, the measured bunch was used as an input for the simulations described in sect. 5.1. In this way it is possible to decide if an isomeric decay would be visible if it existed in the singly charged state. An unknown variable in the simulation is the exact value of the detection efficiencies of ions (ϵ_i) and electrons (ϵ_e) in the respective energy region. From the measurements performed with $^{229(m)}$Th^{2+} and $^{229(m)}$Th^{3+} ion bunches in the same energy range, the ratio between the electron and ion detection efficiencies, ϵ_e and ϵ_i, respectively, can be estimated to be $\epsilon_e/\epsilon_i = 25$. It is assumed that the detection efficiency for electrons stays constant and that the one for the ions does only depend on the ion's kinetic energy and not on its charge state. Scenarios of two different detection efficiency ratios ϵ_e/ϵ_i are studied. Fig. 5.9a shows the pessimistic case with $\epsilon_e/\epsilon_i = 1$, while Fig. 5.9b displays a realistic case with $\epsilon_e/\epsilon_i = 25$. In Fig. 5.9b the values were used which were found to fit well for ions with this kinetic energy (used and shown in Fig. 5.5).
The absence of an isomeric decay in the singly charged state can only be explained by the isomeric lifetime in singly-charged ^{229m}Th being shorter than the extraction

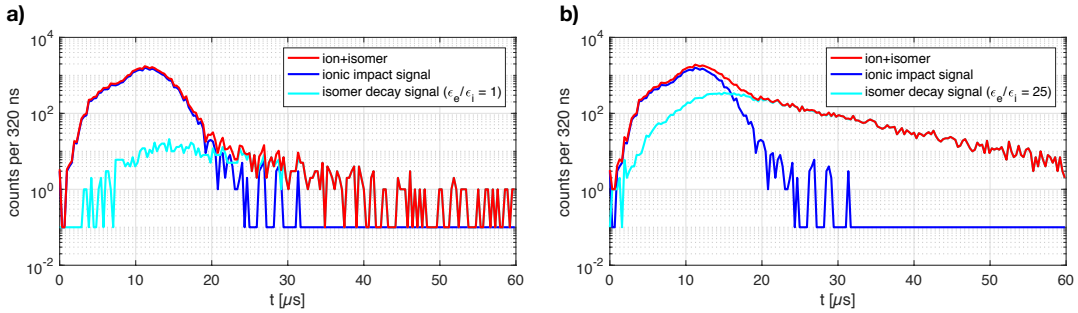

Figure 5.9: Simulation performed with a bunch input from a measurement of ≈13,000 $^{229(m)}Th^{1+}$ bunches. Panel a) shows the pessimistic case of $\epsilon_e/\epsilon_i = 1$ and panel b) a realistic case with $\epsilon_e/\epsilon_i = 25$. The ionic impact signal (blue) shown in both figures is the measured signal, without any scaling. Bins that contain no counts are subsequently set to 0.1 counts for a better visualization of the baseline.

time, which is in the range of several ms [105]. For an isomer with a transition energy below the second ionization potential, such a short lifetime in the singly charged state can be explained by quenching of the isomer in the buffer gas or by a bound internal conversion decay of the isomer in the 1+ charge state [122]. A possible way to investigate the lifetime of the isomer in the 1+ charge state is by generating this charge state from $^{229m}Th^{2+}$ or $^{229m}Th^{3+}$ ions by charge exchange in carbon foils (see sect. 4.3 and [101]). This could allow to shorten the time between generation of the 1+ charge state and the isomer detection. The efficient generation of ions in the 1+ charge state, however, requires 2+ or 3+ ions with high kinetic energies of several 100 keV. The resulting 1+ ions have kinetic energies in the same energy range, which makes it experimentally challenging to control the 1+ ions after generation.

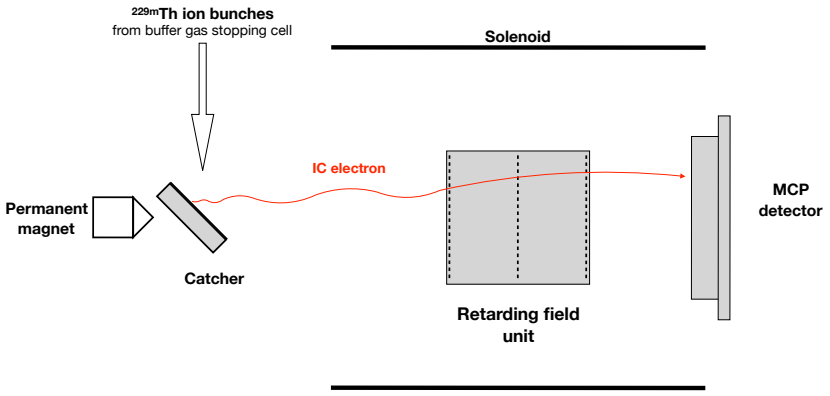

Figure 5.10: Sketch of the experimental setup that was used to measure the decay properties of ^{229m}Th in different host materials. ^{229m}Th ion bunches are collected on the surface of a catcher which is placed in the collection region of a magnetic bottle spectrometer (see section 3.2).

5.3 Influence of the electronic environment

It was predicted that the lifetime of the internal conversion decay channel of ^{229m}Th depends strongly on the electronic environment of the nucleus [12]. In lifetime measurements of the nuclear isomer in ^{235}U [93, 94] (which is the energetically second lowest nuclear excited state after ^{229m}Th) it is found that the lifetime of the internal conversion decay channel on a catcher surface is influenced by the host material.
In case a suitable prolongation of the lifetime of the IC channel could be realized for bound Th, the development of a solid-state nuclear clock would come into reach.
The influence of the electronic environment on the lifetime on ^{229m}Th is studied qualitatively in the next sections. The experimental setup that was used for these measurements is shown in Fig. 5.10. $^{229(m)}$Th ion bunches are collected on the surface of a catcher plate which is placed in a magnetic bottle spectrometer. This allows to efficiently collect IC electrons with the magnetic fields and additionally measure the kinetic energy of the emitted electrons.
By measuring the kinetic energy of the internal conversion electrons emitted from the surface, the qualitative dependence of the lifetime on the implantation depth can be measured.
The presented measurements confirm a strong dependence of the internal conver-

sion decay properties on the electronic environment.
A measurement series was conducted, where in addition to the temporal behaviour also the energy of the emitted electrons was investigated with a magnetic bottle spectrometer. The measurements are shown in Fig. 5.12 and the resulting half-life from an exponential fit is shown in Fig. 5.11. The measurements were performed with $^{229}Th^{2+}$ ions which were collected on a platinum surface with a kinetic energy of 60 eV: the 2+ ions start at a potential of +15 V in the RFQ-buncher and are collected on the catcher by an attractive potential of −15 V. It is found that the measured lifetime depends on the applied blocking voltage. Additionally, it turns out that for larger blocking voltages the lifetime decreases. Furthermore, in comparative measurements performed with ^{230}Th no decay signal was measured.
This is evidence that the decay of the isomer is governed by more than one decay constant. Such behaviour cannot be explained from a decay constant that depends on the kinetic energy of the emitted electron. If this would be the case, the isomer's activity would still result in a decay curve with a single decay constant. Therefore, the findings can be interpreted such that the different decay constants result from different electronic environments. In this case, the ^{229m}Th activity can be described as

$$A(t) = N_0 \sum w_i \lambda_i \exp(-\lambda_i t), \tag{5.6}$$

where N_0 is the number of ^{229m}Th atoms that initially decay, λ_i is the decay constant for electronic environment i and w_i is the relative number of ^{229m}Th atoms in this electronic environment. Note the difference to Eq. (5.2), which only assumes a single electronic environment.

There are two possible explanations for the measured behaviour: First, as no cleaning procedure has been applied to the platinum surface, it is possible (and even very likely) that there are monolayers of water or hydrocarbons deposited on the surface. Therefore it can be expected that different lifetimes result from different regions on the surface which are covered with different monolayers. This, however, does not explain the decrease of the lifetime with increasing kinetic energy of the electrons.
Another (and more plausible) way to interpret the data is to explain the behaviour with the penetration depth of the ^{229m}Th ions into the platinum material. The ion's kinetic energy of 60 eV results in an implantation depth of ≈ 5 Å. Electrons that are emitted deeper in the material lose kinetic energy in inelastic collisions with the catcher material. These electrons (that underwent inelastic scattering) can be suppressed more easily by increasing the blocking voltage of the magnetic

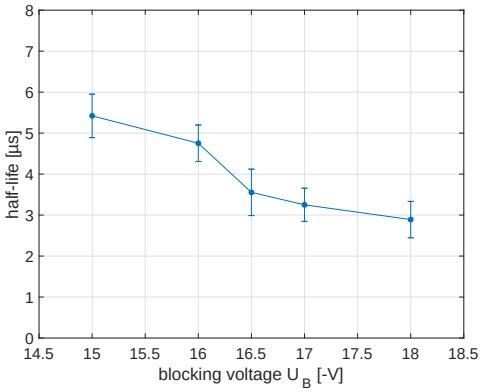

Figure 5.11: The measured half-life versus the applied blocking voltage in the magnetic-bottle electron spectrometer. With increasing blocking voltage electrons originating from deeper surface layers are hindered from reaching the detector. There is a clear decrease in the lifetime with decreasing depth of emission. The lifetime can almost be reduced by a factor of 2.

bottle spectrometer. Electrons with higher kinetic energies (*i.e.* electrons that are not suppressed so easily by the blocking voltage) are more likely to originate from the surface, while the low-energy electrons are mostly due to scattered electrons originating deeper from the catcher. With this interpretation it is possible to conclude that the lifetime of the isomer increases with the depth of deposition of ^{229m}Th in the material.

In conclusion, it is possible to influence the lifetime of the isomeric state in surface bound ^{229m}Th atoms. Further measurements with controlled clean surfaces are needed to further investigate these properties.

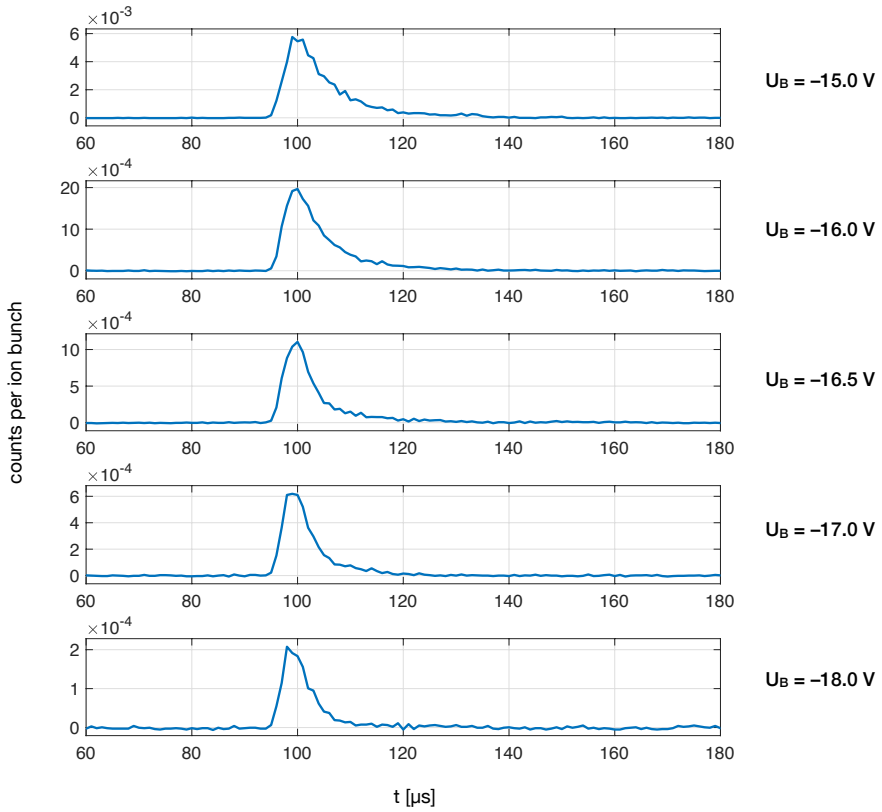

Figure 5.12: Temporal behaviour of the isomeric decay of $^{229\mathrm{m}}\mathrm{Th}^{2+}$ collected on a platinum catcher surface for different blocking voltages U_B applied to the retarding field unit. Electrons, counted in time bins of 1 μs, were normalized to the total number of collected ion bunches. Note that only a minor fraction of the IC electrons reaches the detector when -18 V blocking voltage are applied. Note, that the electrons are emitted from the catcher which is set to -15 V, which requires the rather large blocking voltages.

CHAPTER 6

Energy Measurements

Progress towards a nuclear optical clock was so far mainly impeded by the imprecise knowledge of the ^{229}Th isomer's excitation energy.
In the following chapter energy measurements are presented that use electrons which are emitted in the internal conversion (IC) decay of ^{229m}Th. The measurement of the kinetic energy of these electrons allows to determine the excitation energy of the isomer. $^{229(m)}$Th ions which were extracted from the buffer-gas stopping cell (as detailed in chapter 3) are used. As shown in chapter 5, the lifetime of the internal conversion decay process is in the range of microseconds and energetically only allowed in neutral ^{229m}Th. Therefore it is possible to trigger IC decay by neutralizing ^{229m}Th ions. Instead of neutralizing the ions by collecting them on a metallic surface (as in the lifetime measurements), the ions are now neutralized while traversing a bi-layer of graphene in order to allow for the internal conversion decay to occur in-flight. This enables measuring the IC electrons free from any surface influences.
After neutralization, ^{229m}Th continues its flight as a fast atom through the electron collection region of a magnetic bottle spectrometer (that is detailed in section 3.2). During their flight the isomers decay to their ground state by emitting IC electrons. The kinetic energies of the IC electrons are measured with the magnetic bottle spectrometer and its retardation unit, when the isomers decay inside the spectrometer's collection region. The process is shown in Fig. 6.1: $^{229(m)}$Th ions are guided by focusing electrodes onto a bi-layer of graphene. As the ions traverse the graphene, they are neutralized and fly towards a permanent magnet of a magnetic bottle spectrometer, that creates an inhomogeneous magnetic field in which electrons are collected. Charged particles that are created during the neutralization are hindered with bending electrodes from reaching the collection region above the permanent magnet. The collected electrons are guided towards a retarding field unit with its variable retardation potential, to be finally regis-

tered with an MCP detector if their kinetic energy is large enough. This enables to measure conversion electron spectra.
While at first glance measuring the kinetic energy of an electron seems straightforward by applying a variable retarding potential in front of the MCP detector, the physical reality is more complex: In the neutralization process atomic excited states can be populated which influence the IC electron spectra. The exact population of atomic excited states cannot be measured. The influence of the distribution of atomic excited states on the energy determination is quantified by comparing the measured spectra with theoretical predictions.

The subsequent chapter is structured as follows: First, the expected IC electron count-rate is estimated and the expected shape of IC electron spectra are shown in section 6.1. Second, the conversion electron measurements are shown together with comparative measurements that allow to unambiguously attribute the measured signal to IC electrons from the ^{229m}Th decay (section 6.2.2). In a third part (section 6.3) the measured data is compared to predicted spectra, which allows for the first time to deduce a value for the excitation energy of ^{229m}Th based on direct decay properties.

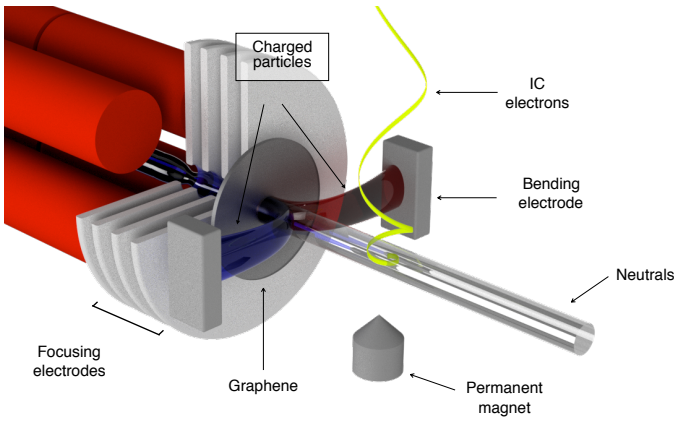

Figure 6.1: Visualization of the main underlying experimental concept and the neutralization principle that is used for the direct energy determination of ^{229m}Th. $^{229(m)}$Th ions are sent through a bi-layer of graphene, where the ions are neutralized. Neutral $^{229(m)}$Th atoms continue their flight towards the collection region of a magnetic bottle spectrometer, where emitted IC electrons are collected. Charged particles generated during the neutralization or $^{229(m)}$Th ions that were not fully neutralized are deflected with bending electrodes, so that they do not cause any background signal. Figure is taken from Ref. [1].

6.1 Expected signal

In the following sections the expected signal measured with the MCP detector in terms of count rate and spectral shape is discussed. The results are used to estimate the feasibility and to identify possible shortcomings and limitations of the approach.

6.1.1 Expected IC electron count rate

The expected number of internal conversion electrons per extracted ^{229m}Th ion bunch as well as the resulting signal-to-noise ratio is calculated in the following. As soon as the ions are neutralized, the isomer decays within the next microseconds. In the spectrometer setup only those IC electrons are detected which are emitted in the collection region above a permanent magnet. In the context of the experiment it makes sense to consider the number of decays per length dN/dx (instead of the conventional quantity dN/dt). The activity per length is plot-

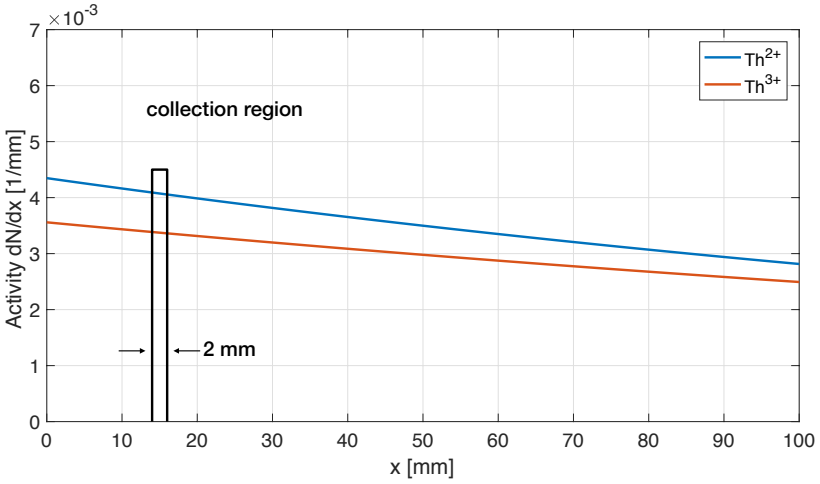

Figure 6.2: The isomer decay activity per length unit of the flight path (normalized to unity) plotted against the distance from the point of neutralization. The curves are generated under the assumption that the q = 2+ and q = 3+ ions are accelerated with −315 V before neutralization. Additionally, the position of the electron collection region, in which the electrons are counted, is shown by the black rectangle.

ted in Fig. 6.2 for $^{229m}Th^{2+}$ and $^{229m}Th^{3+}$ ions accelerated with 315 V before neutralization. Additionally, the position and width of the collection region is shown. The collection region is centered at a distance $d_1 \approx 16$ mm behind the neutralization position and extends over $d_2 \approx 2$ mm. The ions fly with a velocity $v = \sqrt{2E_{\text{ion}}/m_{229}}$ (where E_{ion} is the ion's kinetic energy and m_{229} is the mass of ^{229}Th) towards the electron collection region of the spectrometer.
In the experiment we start with N_0 ions that are contained in one bunch. The fraction of isomers contained per bunch is given with $\epsilon_{\text{iso}} = 2$ % and only a fraction ϵ_n is neutralized. The neutralization efficiency, ϵ_n, takes the transmission of the TEM grid supporting the graphene layers into account and is conservatively estimated to be 25 %. This means there are

$$N_{\text{iso}} = \epsilon_{\text{iso}} \epsilon_n N_0 \tag{6.1}$$

neutralized isomers available for subsequent conversion electron studies.
After neutralization, the isomer decays with a decay constant of $\lambda = 1/(10\ \mu\text{s})$ [11]. The isomer fraction that survives until it reaches the collection region at a distance d_1 can be calculated via $\epsilon_d = \exp(\lambda d_1/v)$. In this way, the IC activity in the center of the collection region can be expressed as

$$A_{IC} = \lambda N_{\text{iso}} \exp(\lambda d_1/v) = \lambda N_{\text{iso}} \epsilon_d, \tag{6.2}$$

where $N_{\text{iso}} = \epsilon_{\text{iso}} \epsilon_n N_0$ is the number of neutralized ^{229}Th atoms which are in the isomeric state. The number of IC electrons,N_{IC}, that are emitted in the collection region is calculated under the realistic assumption that only a small fraction of the isomers decay while traversing the collection region (*i.e.* $\lambda d_2/v << 1$, so that $\exp(\lambda d_2/v) \approx 1$):

$$N_{IC} = A_{IC} \Delta T = A_{IC} \frac{d_2}{v}, \tag{6.3}$$

where $\Delta T = \frac{d_2}{v}$ is the time the atoms spend in the collection region. The combined collection, transmission and detection efficiency of the magnetic bottle spectrometer (80% collection efficiency, 3 grids with 90% transmission, 50 % detection efficiency of the MCP) is assumed to be $\epsilon_{\text{MaBo}} \approx 30$ %. So finally the number of measured electrons per bunch N_{MaBo} can be calculated to be

$$N_{\text{MaBo}} = \epsilon_{\text{MaBo}} N_{IC} = \lambda \Delta T \epsilon_{\text{MaBo}} \epsilon_{\text{iso}} \epsilon_n N_0. \tag{6.4}$$

An overview of the resulting numbers for Th^{2+} and Th^{3+} ions accelerated with -315 V onto graphene is given in Table 6.1.
The derived number of 2.4 to 4.2 electrons per 1000 ion bunches is well in agreement with measured data, where a count rate of typically 5 to 10 electrons per

	v [$\times 10^4$ m/s]	N_0	$\frac{N_{IC}}{N_{\text{iso}}}$ [%]	e$^-$ per 10^3 bunches
$^{229(\text{m})}\text{Th}^{2+}$	2.30	200	0.8	**2.4**
$^{229(\text{m})}\text{Th}^{3+}$	2.81	400	0.7	**4.2**

Table 6.1: Overview of the values that are used to calculate the expected IC electron count rate. N_0 is the number of ions per bunch. $\frac{N_{IC}}{N_{\text{iso}}}$ gives the ratio between the total number of isomers in the bunch and the number of isomers which decay in the collection region. For the velocity it is assumed that the kinetic energy of the atoms is 630 eV and 945 eV for the 2+ and 3+ charge states, respectively.

1000 $^{229(\text{m})}$Th ion bunches is measured. Note that in the above calculations it is assumed that 100% of the neutralized atoms reach the collection region of the spectrometer. This, however, requires proper collimation of the ions onto the graphene layers. The focal point is charge state dependent and was optimized for $^{229(\text{m})}\text{Th}^{3+}$ ions.
The dark count rate of the MCP detector is typically 3 counts per second. The arrival time of the IC electrons is correlated with the ion bunch in a time window of 6 μs/bunch (see section 4.1 and Fig. 6.5). Therefore, one expects 18×10^{-6} dark counts per bunch. This leads to an excellent signal-to-noise ratio of 170:1 and 280:1 for 2+ and 3+ ion bunches, respectively.

6.1.2 Excited electronic states after neutralization

The mechanisms involved in the neutralization of ions penetrating matter are detailed in Ref. [96] and shortly reviewed in section 2.4. The dominant process involved in the neutralization of Th ions in graphene is resonant neutralization. Here, electrons from the graphene conduction band are transferred resonantly to excited states in the Th atom. The exact population of these states cannot be measured in our experimental setup and is the largest source of uncertainty (see section 6.3).

A first estimate of the electronic excited state distribution can be made by comparing the work function of graphene with the ionization potential of thorium: When a particle approaches a solid, its vacuum energy level is aligned with the vacuum energy level of the solid E_{vac}. The atom's ground state E_0 lies below the vacuum energy. For an unperturbed atom, this difference is given by the ionization potential of the atom: $E_{\text{vac}} - E_0 = \text{IP}$. In the conduction band of a solid,

electrons are populated up to the Fermi level E_F which lies below the vacuum level, and the difference is given by the work function: $E_{\text{vac}} - E_F = W$. Only electrons from the conduction band can be resonantly transferred to the impinging atom. An upper energy limit for excited atomic states can thus be estimated by subtracting the atom's ionization potential from the work function. For Th ions (the Th^{0+} IP is given by 6.3067±0.0002 eV (in the following this is approximated with ≈ 6.31 eV) [10]) neutralized in graphene (with a work function of 4.57 eV [123]) the maximum accessible excited state can be estimated to be ≈ 1.74 eV.
For a reliable estimate of excited states it needs to be considered that the levels in the Th atom are bent and change their energy as they are approaching or transiting a solid due to image charges in the solid or screening by the solid's electrons. A detailed description can be found in section 2.4. Density functional theory (DFT) calculations allow to calculate which states become resonant with the graphene conduction band. These calculations show that excited states up to an excitation energy of 2.5 eV can come into resonance as they transit the graphene layers [1]. A table of all excited states with their configurations is given in Table B.1 in Appendix B.

6.1.3 Internal conversion from ^{229m}Th atoms

Expected IC electron spectra were calculated by the theory group from the Max-Planck-Institut für Kernphysik in Heidelberg as introduced and developed in Ref. [87]. An overview of the findings from Ref. [87] as used for the energy determination performed here is also given in section. 2.3.1.
The kinetic energy of the electron (E_{kin}) after IC is expressed via

$$E_{\text{kin}} = E_I - (IP - E_i + E_f), \tag{6.5}$$

where E_I is the isomeric energy, IP is the ionization potential (precisely known as 6.3067±0.0002 eV [10]), E_i is the initial excitation energy of the electronic shell and E_f is the excitation energy of the ion in the final state after internal conversion. Pairs of initial and final states follow certain selection rules. The resulting decay rates are calculated with Eq. (2.35) in section 2.3.1, taken from Ref. [87].
IC rates were calculated for all excited electronic states which potentially came into resonance with the graphene conduction band. These calculations were used to predict the IC electron spectra that can be measured with the magnetic bottle spectrometer.
The predicted IC electron spectrum for ^{229m}Th in the electronic ground state with an expected isomeric energy of 8.3 eV is shown in the left panel of Fig. 6.3.

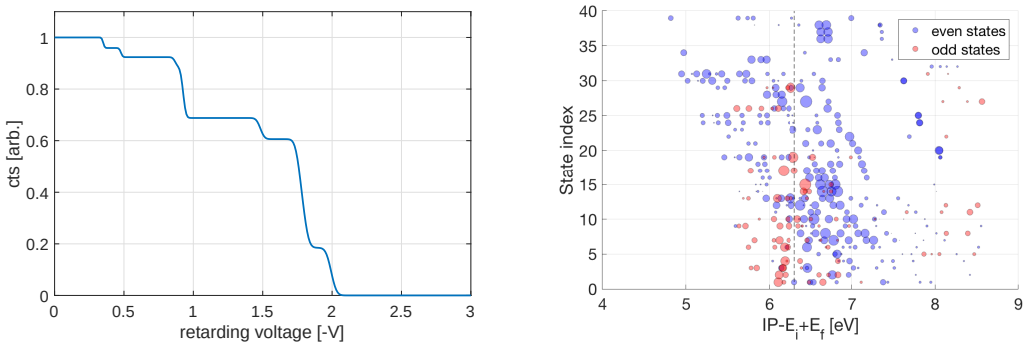

Figure 6.3: Left panel: Internal conversion electron spectrum as expected to be measured with the electron spectrometer from the decay of ^{229m}Th in its electronic ground state. The energy of the isomer was assumed to be 8.3 eV. Right panel: Scatter plot of the possible pairs of initial (E_i) and final (E_f) states. Each row (represented by the y-position in the scatter plot) corresponds to an initial electronic state, which can be identified by its "state index" listed in Table B.1. Even (odd) electronic initial states are shown in blue (red). The size of the points represents the rate of IC electrons for the corresponding (E_i, E_f)-pair. The vertical black dashed line visualizes the ionization potential (IP=6.31 eV).

The spectrum takes the energy resolution ($\Delta E/E = 3\%$) of the spectrometer into account. It illustrates the resulting broadened edge of the kinetic energy distribution of the electrons that reach the MCP detector across the blocking voltage of the electron spectrometer. The spectrum contains the contribution of 7 excited final states (2 cannot be separated and appear as a single edge in the spectrum). The right panel of Fig. 6.3 visualizes the internal conversion rates for all initial excited states that can possibly come into resonance with the graphene conduction band (see section 6.1.2 and Table B.1). The blue circles denote states with even wave functions, the red ones with odd wave functions. The size of the symbols indicates the rate of IC electrons expected from the specific (E_i, E_f) pair of states. The "state index" on the y-axis represents the list item number of the respective initial state listed in Table B.1 in the Appendix.

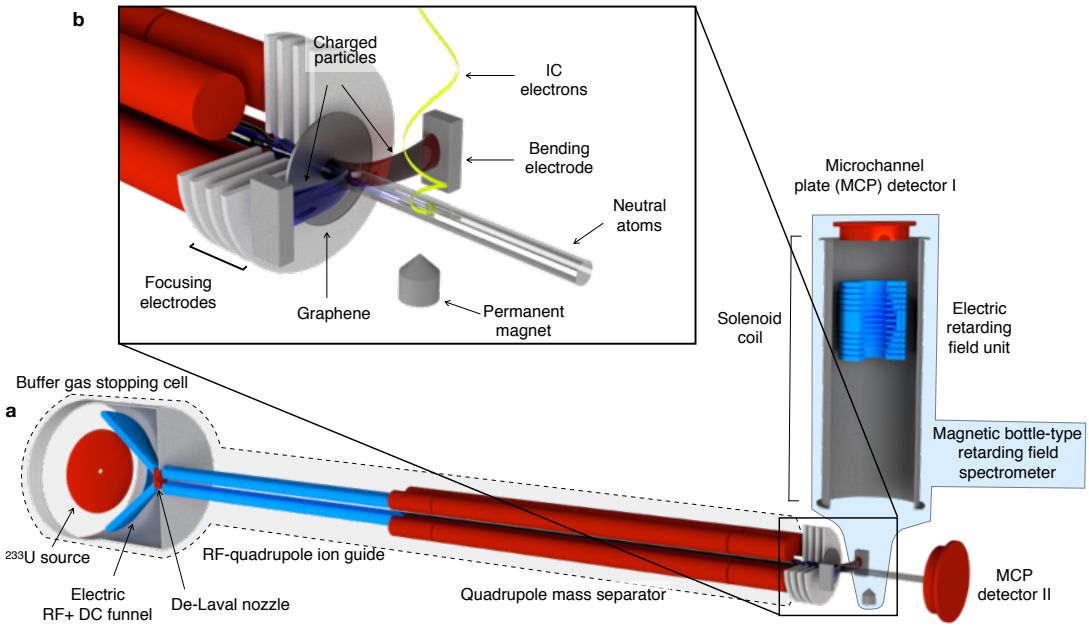

Figure 6.4: Overview of the experimental setup that is used for the energy determination. A detailed description is given in chapter 3 and in Ref. [1]. Panel a shows the extraction part as detailed in chapter 3 and already used for the lifetime measurements in chapter 5. Panel b gives a detailed view of the focusing electrodes together with the graphene foil and the bending electrodes that are used to reduce background which is induced by remaining charged particles. Figure is taken from Ref. [1].

6.2 Internal conversion electron measurements

In the following section the internal conversion electron measurements performed with the setup shown in Fig. 6.4 are described. The measurements were performed with the graphene layers set to −300 V. The applied voltages to each element are listed in the Appendix in Table C.1. An overview of the experimental setup (as described in chapter 3) is shown in Fig. 6.4: ^{229m}Th ions that are extracted from a buffer-gas stopping cell are phase-space cooled, transported through the mass separator and finally electrostatically focused onto a bi-layer of graphene where they neutralize. They decay in flight by internal conversion as they travel through the collection region of a magnetic bottle spectrometer. Conversion electrons that are collected by the spectrometer and able to overcome a retarding voltage applied to an electric retarding field unit are counted with an

MCP detector (MCP I in Fig. 6.4). The neutralized atoms can be counted with MCP II, which is placed in the beam axis. For the experiment no mass separation was required, as an IC electron signal can only be expected for the ^{229}Th isomer and the measurement can be assumed to be background free (see section 6.2.1). The corresponding IC electron signal, as measured with the magnetic bottle spectrometer at two different retarding voltages, is shown in Fig. 6.5a. The characteristic time-of-flight spectrum of Th^{2+} (peaking at t≈97 μs relative to the release time of the ion bunch in the RFQ buncher) and Th^{3+} (t≈80 μs) is clearly visible. By increasing the blocking voltage (from 0 V to −3 V) the conversion electrons can be suppressed.
The atoms that are generated by neutralization in the graphene and are transmitted through the spectrometer are counted with an MCP detector placed in the beam axis (MCP detector II in Fig. 6.4). A corresponding signal from the atom transmission is shown in Fig. 6.5b. The efficiency of the atom transmission, and hence also of the IC electron signal, depends strongly on the voltages applied to the focusing electrodes. Additionally, the focusing is charge state dependent. The focusing electrodes are optimized such that the number of transmitted atoms generated from $^{229(m)}Th^{3+}$ ions (corresponding to the peak at ≈ 80 μs) is maximized.
Note that the ratio of the 3+ and 2+ peaks (at ≈ 80 μs and 97 μs, respectively) in the IC electron measurement is not reflected in the atom transmission measurements, which is due to the contribution of $^{233}U^{2+}$ in the atom transmission signal. While the counts in the IC electron measurements are only due to ^{229m}Th (as shown in the following section), the atom transmission signal additionally contains counts due to ^{233}U. ^{233}U is efficiently extracted in the 2+ charged state (in an equal share as ^{229}Th), but not in the 3+ charged state [107]. As there is no mass filter applied to the ion beam and the bunch width does not allow to separate ^{233}U from ^{229}Th, both contribute to the 2+ peak in the atom transmission measurement. The reason to not use any mass separation is that it allows to measure the IC decay of neutralized ^{229}Th ions in two different charge states at the same time. These should lead to the same results and can thus be used to check for consistency.

6.2.1 Potential background

In the neutralization process there are several effects that may cause secondary electrons: *ion scattering*, *secondary electrons* produced during the neutralization, *fast atom impact* or *auto-ionizing states*.
In order to exclude that the measured IC electron signal is due to such secondary

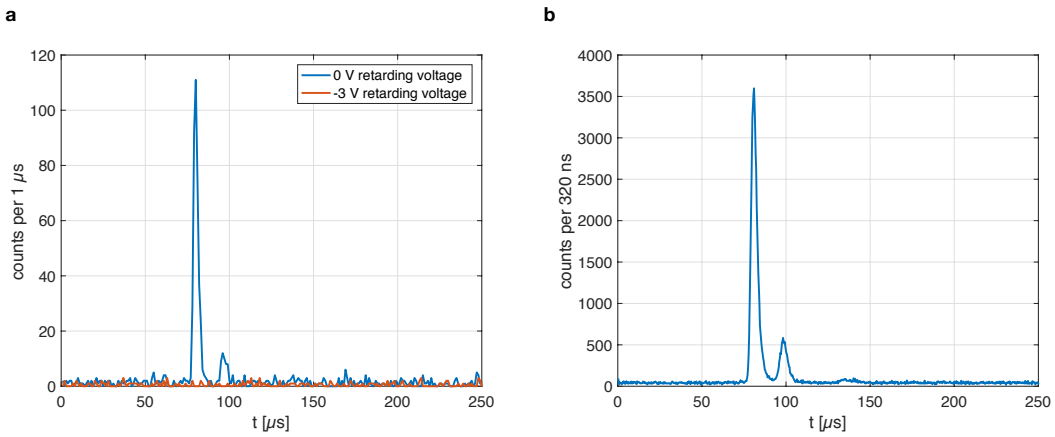

Figure 6.5: a) IC electron signal as measured with the magnetic bottle spectrometer. The signal at ≈80 μs (≈97 μs) results from neutralized $^{229m}Th^{3+}$ ($^{229m}Th^{2+}$) ions. Two different blocking voltages were applied (blue: 0 V, red: −3 V). The IC electron count rate can be suppressed at higher blocking voltages.
b) Number of transmitted atoms that are measured with the MCP detector placed in the beam axis behind the magnetic bottle spectrometer (MCP detector II in Fig. 6.4). For a detailed description see text.

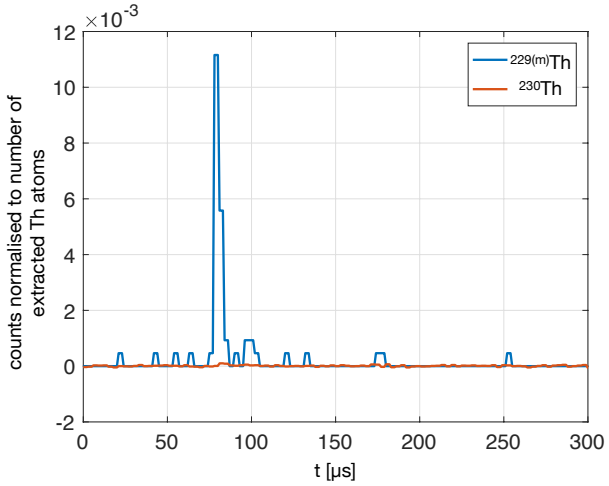

Figure 6.6: IC electron signal measured with ^{229m}Th ions (blue) and with ^{230}Th ions (red). The ^{229m}Th data results from 5000 ion bunches. For the ^{230}Th data more than 800 000 ion bunches were recorded. The measurements were normalized to the atom transmission signal of Th^{3+}.

electron processes, comparative measurements with ^{230}Th ions (which were extracted from a ^{234}U α-recoil source) were performed. Apart from the low-energy nuclear isomeric state, only present in ^{229}Th, ^{230}Th ions behave identical. Fig. 6.6 shows the electron signal measured with the magnetic bottle spectrometer (0 V blocking voltage) for both $^{229(m)}$Th ions (blue) and ^{230}Th ions (red). The counts were normalized to the number of neutralized and transmitted atoms (counted with MCP II). In these comparative measurements no signal was found for ^{230}Th. Consequently, the measured signal in the spectrometer must be fully attributed to the isomeric decay of ^{229m}Th. Still, the possible sources of background and their suppression are discussed in the following section.

Scattered ions (and ions resulting from charge exchange) are deflected by the bending electrodes which are set to +300 V and +1000 V, respectively (see Fig. 3.12). This leads to repelling forces acting on positively charged particles. Additionally, secondary electrons, which might be generated from ions impinging on the bending electrodes, are energetically not able to enter the spectrometer region.

Secondary electrons are generated when the ions pass through the carbon foil. These electrons can also be hindered from entering the spectrometer region by applying the voltages described above to the bending electrodes. The electrons

are simply bent towards the electrode which is set to the higher potential (as visualized in Fig. 3.12).

Fast atoms which are generated in the foil cannot be influenced by the bending electrodes, therefore fast atoms overcome the blocking electrodes and it could potentially happen that they hit surfaces near the collection region. In this way secondary electrons could be generated, while the fast atoms continue their flight as ions or generate ions in sputtering processes.
Such effects have not been observed in the setup. The reason for this behaviour is the special geometry of the spectrometer collection region: the fast atom beam is guided through apertures before reaching the spectrometer's collection region. Therefore only a well collimated atom beam will allow to measure IC electrons. Furthermore, the collection region is cut out so that there is no material that could generate secondary electrons near the collection region.

Auto-ionizing states were investigated in measurements with ^{230}Th ions and have not been observed. There are several reasons: First, one can expect that these states have a short lifetime compared to the time-of-flight between the point of neutralization and the spectrometer collection region (some 100 ns). Second, if auto-ionizing states would be strongly populated in the neutralization process, there would not be any neutral thorium atoms left after their decay.

In conclusion, the measured electron signal in the magnetic bottle spectromer, as shown in Fig. 6.5a, can be unambiguously attributed to the ground-state decay of $^{229\mathrm{m}}$Th. Thus, the experimental setup provides the means for a background free measurement of the kinetic energy of the internal conversion electrons emitted in the ground-state decay of the isomer.

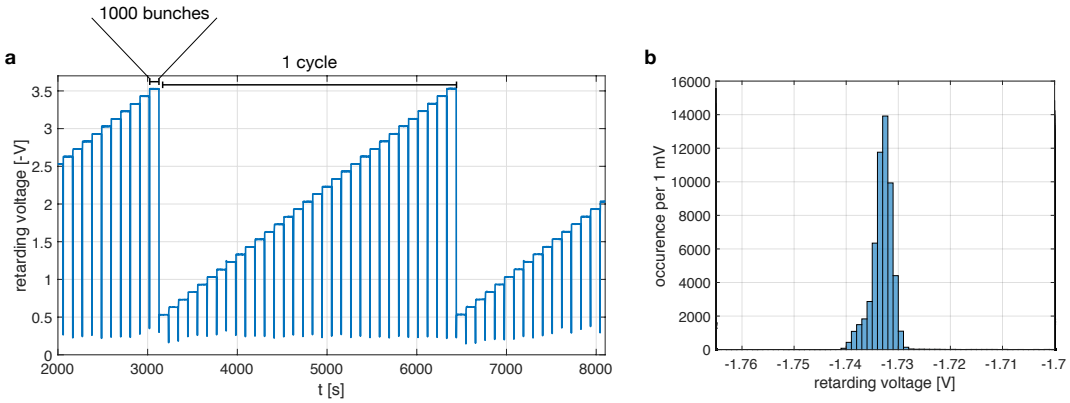

Figure 6.7: The applied retarding voltages throughout the measurement, whose data are shown in Fig. 6.8. The left panel shows the temporal sequence of the applied retarding voltage. The retarding voltage is incremented by 0.1 V every 1000 bunches (≈100 s). The right panel shows the distribution of an exemplary retarding voltage, indicating its stability to better than 10 mV. Figure taken from Ref. [1].

6.2.2 IC electron spectra

In order, to record IC electron spectra, conversion electrons are counted for different retarding voltages. The applied retarding voltage is monitored throughout the whole time of the measurement (see Fig. 6.7). In order to reduce the influence of the extracted number of particles on the IC electron spectrum, the retarding voltages are ramped in discrete steps in saw-tooth shaped cycles. During one cycle, each blocking voltage is held for a fixed number of bunches (1000 ion bunches ($\hat{=}$ 100 s) per blocking voltage) and is incremented afterwards. Before the voltage is incremented, it is set to 0 V. This makes the measurement independent from the slope of the ramp. After reaching the highest retarding voltage, the cycle starts again with the lowest blocking voltage (see Fig. 6.7a). Typically, blocking voltages are incremented by 0.1 V and applied with a high precision voltage supply unit[1]. Fig. 6.7b shows a histogram of one exemplary applied retarding voltage as monitored during the whole measurement period of ≈3 days. The stability is better than 10 mV and limited by temperature fluctuations. A typical resulting IC electron spectrum is shown in Fig. 6.8, together with a fit function, which is

[1] mesytec GmbH, MHV-4.

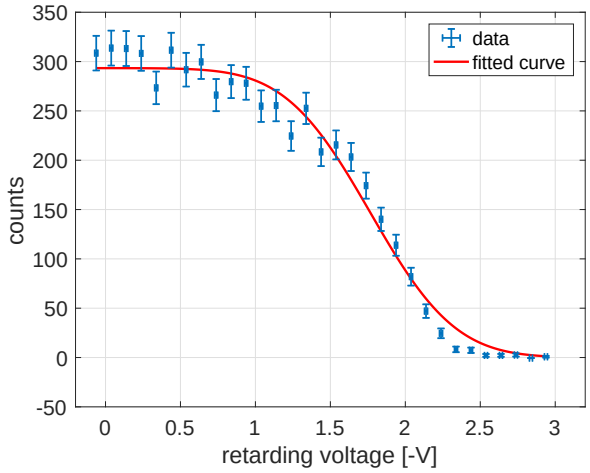

Figure 6.8: Integrated conversion electron spectrum of $^{229(m)}$Th as measured with the magnetic bottle spectrometer for a period of about 3 days. The shown data was taken with neutralized $^{229(m)}Th^{3+}$ ions. The retarding voltage is corrected for surface potential differences.

explained in the subsequent section. Spectra with smaller increments of ≈0.04 V were also recorded to investigate possible internal structure of the spectra.

In both measurements (0.1 V or 0.04 V increments) no distinct reproducible lines, which would manifest themselves as obvious edges in the retarding field spectrum, were measurable which otherwise could serve for the energy determination of the isomer. This is a clear indication that the IC electrons are not emitted from just a single excited atomic state. Considering the energy resolution of the spectrometer in the range between 1 eV and 2 eV, found to be between 0.03 eV and 0.06 eV (FWHM), it should be possible to resolve at least 16 lines (1 eV/0.06 eV ≈ 16.7). From the theoretical spectra, we can estimate that there are typically about four lines per excited atomic state with kinetic energies between 1 eV and 2 eV. As there are no lines resolvable, we can conclude that there are at least five initial atomic states contributing strongly to the IC electron spectrum. This motivated an analysis procedure which is described in the next section.

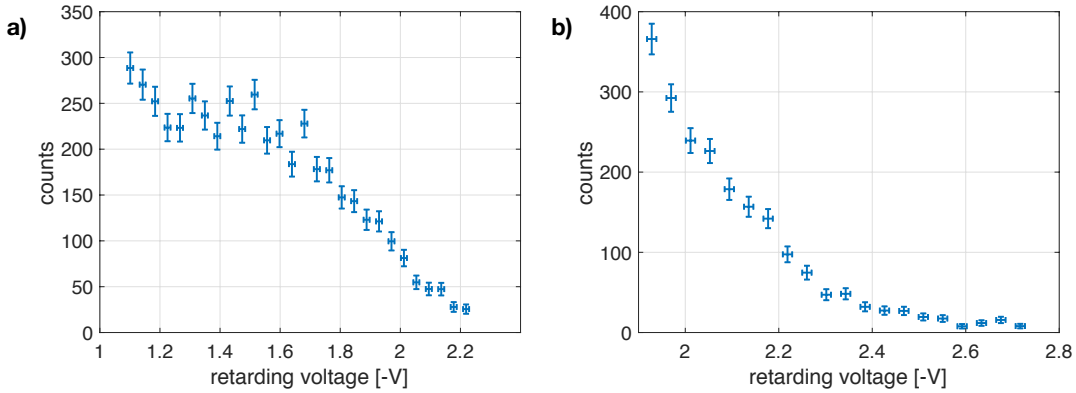

Figure 6.9: Measurements performed with a step size of ≈0.04 V. No conclusive edges (*i.e.* distinct lines of electron energies) have been found in these measurements. a) Fine measurement between ≈-1.1 V and ≈-2.2 V retarding voltage.
b) Fine measurements of the "high-energy" part of the conversion electron spectrum between retarding voltages of≈-1.9 V and ≈-2.7 V.

6.3 Energy determination

Given the absence of distinct lines in the IC electron spectrum that would allow to determine the isomeric energy by the assignment of (E_i,E_f)-pairs to these lines, another method for the determination of the isomeric energy is needed. Consequently a method was developed, where the first step consists of fitting a complementary error function

$$f(U) = a\left(1 - \mathrm{erf}\left[\frac{U - E_{\mathrm{defl}}}{b}\right]\right) \tag{6.6}$$

to the measured data, where U is the applied retarding voltage, a is a scaling factor, E_{defl} is the deflection point of the error function and b is a parameter related to its width. The data and fit is shown in Fig. 6.8. It should be pointed out that the fit function was not chosen to reach an optimized reproduction of the experimental data, but rather to provide a tool to determine the deflection point of the energy spectrum. Further details turn out to be irrelevant for the determination of the isomer's excitation energy. The fit results in E_{defl}=1.77±0.03 eV and b = 0.6 ± 0.1 eV. The kinetic energy of the electrons depends linearly on the energy of the isomer, therefore the deflection point of the error function can be used as

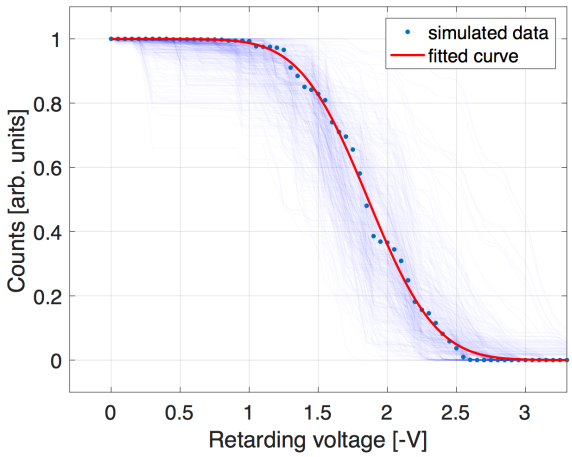

Figure 6.10: Error function fit (red) applied to an exemplary simulated spectrum, with 5 initial excited electronic states. The thin lines in the background are a family of curves consisting of simulated spectra generated from an arbitrary selection of 5 electronic excited states. These curves should give an impression of the scattering (or bandwidth) of spectra due to unknown excited state distributions.

a measure for the latter:

$$E_I = E_{\text{defl}} + E_0, \tag{6.7}$$

where E_0 is a reference energy. The reference energy E_0 is determined by applying the identical fit function to simulated data, which use the IC rates determined in [87]. Since the exact population of the electronic excited states is not known, random populations of electronic states are simulated and fitted with the complementary error function. An exemplary (arbitrarily selected) simulated spectrum together with the fit function that determines the deflection point is shown in Fig. 6.10. Additionally, a family of curves is shown in the background which consists of 500 simulated spectra each with different arbitrary initial atomic state distribution[2]. The resulting deflection of each simulated population is filled in a histogram which includes typically 20,000 entries of deflection points. The histogram allows to quantify the influence of the excited state distribution on the energy determination via the behaviour of the deflection point of the error function. Values are only filled into the histogram if the width (defining the shape of

[2]The number of 500 spectra in Fig. 6.10 was only chosen for illustrative purposes, as this number already gives a good impression of the scattering of spectra. If significantly more spectra would be plotted as thin lines in this figure, the whole plot would have become unclear.

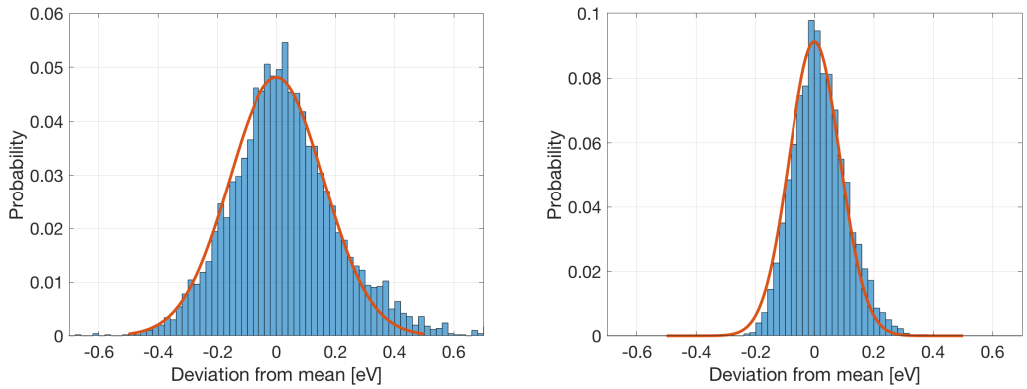

Figure 6.11: Histograms of the resulting deflection point of the error function fit applied to the predicted IC electron spectra which were generated with random populations of initial electronic states. The left panel shows the distribution resulting from the selection of 5 states out of the 83 possible initial electronic excited states. In the right panel the distribution corresponding to the selection of 20 states is displayed. The deviation from the mean value of the distribution is plotted. The corresponding mean values can be found in Table 6.2. The red lines are gaussian fits to the histogram data.

the spectrum) is comparable to the measured width and thus the fit parameter b is in the interval 0.60±0.15 eV.
For random population of excited states it is found that:

(*i*) the deflection points scatter around a robust central value and the distribution has a gaussian shape. Two histograms are shown in Fig. 6.11. Note that the histograms are slightly asymmetric, which is, however, not taken into account, as the asymmetry has only minor influence on the total width of the spectrum.

(*ii*) the central value shifts linearly with the simulated isomeric energy. This results from Eq. (6.5) and justifies Eq. (6.7): the kinetic energy of the electrons differs from the isomer only by an offset value given by the ionization potential and the initial and final state energies. The number of final electronic states which are accessible by internal conversion depends on E_I. In the energy region under consideration (≈7.8±1.0 eV, *i.e.* a 2σ range of the energy measured in [31]), it can be expected, however, that the position of the deflection point as determined by the error function fit is not affected by new accessible final states (which lead to low energy electrons).

(*iii*) the scattering of the values, defined by the standard deviation of the histogram, depends strongly on the number of randomly selected excited states that make a strong contribution to the IC electron spectrum. This can be understood as follows: the more states contribute to the spectra the lower is the influence of one state on the position of the deflection point.

The central value of the deflection point histogram is subtracted from the simulated isomeric energy and taken as the reference energy E_0 (as listed in Table 6.2). These findings allow to determine the isomer's excitation energy by fitting the complementary error function to the data as shown in Fig. 6.8 and using Eq. (6.7). The uncertainty of this analysis is defined by the standard deviation of the resulting histogram.

From the findings in section 6.2.2 it follows that at least 5 atomic states are populated, which leads to a systematic uncertainty of 0.16 eV introduced by the described analysis procedure (see Tab. 6.2). It should be noted that the choice of 5 excited initial electronic states for the determination of the systematic uncertainty is in fact the most conservative choice, given the measured spectrometer resolution and the correlation of σ as a function of the number of states shown in Fig. 6.12 and listed in Tab. 6.2. The isomer's excitation energy value can be determined by adding the position of the deflection point E_{defl}=1.77 eV to the

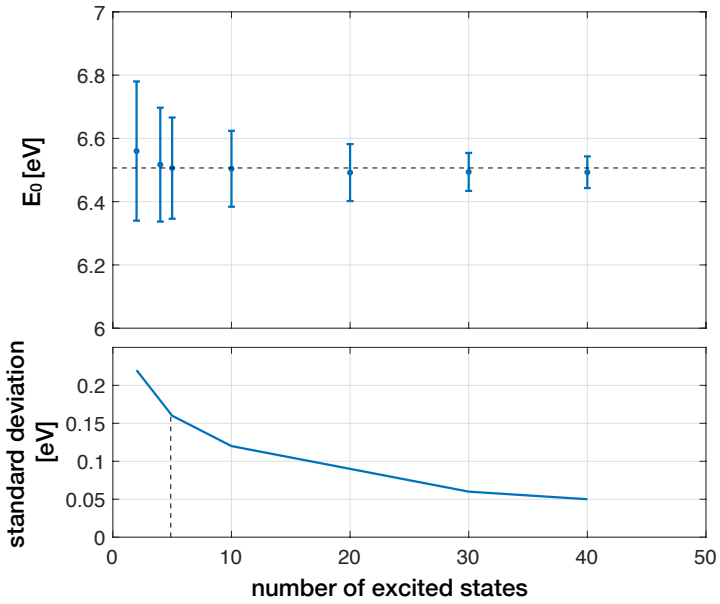

Figure 6.12: Behavior of the histogram with different numbers of initially excited states. The respective data is listed in Tab. 6.2. The top panel shows the reference energy E_0 (defined as the isomeric energy minus the mean value of the histogram) as a function of the number of initial excited electronic states contributing to the simulated spectra. Error bars indicate the standard deviation of the respective histogram, whose values are shown in the bottom panel. The black dashed lines indicate the values which are used for the energy determination.

Number of excited states (n)	E_0	Width of the distribution σ
2	6.56±0.02	0.22
4	6.517±0.003	0.18
5 *	6.506±0.001	0.16
10	6.504±0.001	0.12
20	6.492±0.001	0.09
30	6.494±0.001	0.06
40	6.493±0.001	0.05

Table 6.2: Quantification of the influence of different numbers of initially excited electronic states on the systematic uncertainty of the data analysis. The reference energy (E_0) stays almost constant. The systematic uncertainty (σ), however, decreases with increasing n. The calculations were performed with an assumed energy of 8.3 eV. The asterisk marks the values which are used to determine the isomer's excitation energy, for details see text.

reference energy E_0. The total uncertainty is then comprised of the statistical error (0.03 eV) and the uncertainty introduced by the unknown excited state distribution. Measurements that were performed with $^{229(m)}Th^{2+}$ ions lead to E_{defl}=1.73±0.05 eV, which agrees within its statistical uncertainty. The larger statistical uncertainty is due to the ≈10-times lower count rate of the $^{229(m)}Th^{2+}$ ions. Therefore the value obtained with $^{229(m)}Th^{3+}$ ions is used for the energy determination and the $^{229(m)}Th^{2+}$ results are only used to check for consistency. This leads to the final value of the energy ^{229}Th nuclear isomer, which represents the first ever determined value directly based on decay product properties:

$$E_I = 8.28 \pm 0.03_{\text{stat.}} \pm 0.16_{\text{sys.}} \text{ eV} \quad (6.8)$$

$$= 8.28 \pm 0.17 \text{ eV} \quad (6.9)$$

$$\hat{=} 149.7 \pm 3.1 \text{ nm.} \quad (6.10)$$

As the DFT calculations suggest that electronic states with f-orbitals have a higher probability of being excited during the neutralization process, this has also been investigated as a special case. Performing the same analysis procedure as described above, but assuming that all 83 initial states are populated, however, states with f-orbitals being populated 10 times stronger than the other ones, one arrives at an energy value of E_I = 8.17 ±0.05 eV. It must be pointed out, however, that these simulations take idealized conditions into account that cannot be guaranteed in experiments, like for example that the ions traverse the graphene

in the center of a graphene hexagon. Also the cleanliness of the graphene layer is not entering the considerations. Therefore this stronger constrained value, being in agreement with the value introduced above, is not used in any further discussion.

Atomic excited states with lifetimes much shorter than the time-of-flight between the point of neutralization and the spectrometer collection region (which amounts to $\approx$ 570 ns for $^{229(\mathrm{m})}\mathrm{Th}^{3+}$ ions) could potentially be excluded to contribute to the IC electron spectrum. By rescaling available theoretical decay rates [124] to measured relative intensities of spectral lines in thorium [125], it was estimated that all excited states that are involved have a lifetime of 1 μs or longer [1].

CHAPTER 7

Conclusion and Outlook

In the following chapter the findings of this thesis are summarized. Additionally, potential future follow-up experiments on the road towards the final goal of realizing a nuclear frequency standards are proposed.

7.1 Conclusion

The main goal of the thesis was to realize a first direct measurement of the decay properties of the ^{229}Th nuclear isomer. In a first experimental campaign, lifetime measurements of the ^{229m}Th internal conversion decay channel were performed, which act as a starting point for studying the behaviour of the isomer in different chemical environments.
The experiments detailed in chapter 5 represent the first lifetime measurements of the ^{229}Th isomer. These measurements were performed by collecting ^{229m}Th ion bunches on an MCP detector. A signal that can be attributed to the impact of the ions on the detector can be separated temporally from the internal conversion decay of the isomer, which allows to determine the half-life to 7 ± 1 μs. The measured lifetime confirms the predicted large internal conversion coefficient $\alpha_{\mathrm{IC}} = 10^9$.
In a second series of experiments, the ^{229m}Th ions were collected on metallic surfaces which were placed inside of an electron spectrometer. This allowed to analyze the kinetic energy of the emitted IC electrons. It was found that the lifetime is reduced for electrons with larger kinetic energies. A possible explanation is that conversion electrons with larger measured kinetic energies are emitted closer to the surface than those electrons with lower kinetic energy. These measurements demonstrate the strong influence of the chemical environment on the lifetime of the isomer. The lifetime is reduced by about a factor of 2, which is,

to the best knowledge of the author, the strongest measured perturbation of a nuclear lifetime due to the chemical environment.
In view of the heavily pursued approach to realize a solid-state nuclear clock, these findings set a starting point for further investigations (as described in chapter 7.2) aiming to prolong the isomeric lifetime and to allow for the detection of γ rays directly emitted in the ground-state decay of ^{229m}Th.

The main focus of the thesis was on a direct and more precise measurement of the isomer's excitation energy, as this was considered the still missing "holy grail" of ^{229m}Th research, mainly impeding progress towards a nuclear clock.
Before this thesis, indirect measurements, leading to $E_I = 7.8 \pm 0.5$ eV, placed the energy in a delicate region of the optical spectrum: Vacuum ultra violet (VUV) wavelengths require that related experiments are performed under vacuum and the use of special optics and materials is mandatory. An even bigger problem, however, was that the techniques needed to address the lower end of the error bar around 7.3 eV ($\hat{=}$ 170 nm) are completely different to those needed to excited the isomer at the upper end around 8.3 eV ($\hat{=}$ 150 nm). Continuous-wave laser radiation at 170 nm can potentially be reached by high-harmonic generation (HHG) in crystals (like KBBF [126]), whereas, to the author's best knowledge, no crystal is available for second harmonic generation with a reasonable transmission below 160 nm. For these wavelengths HHG is possible in a gas jet, which requires higher intensities and is thus easier to realize with pulsed lasers.

In this thesis the first direct energy measurements of the ^{229}Th isomer are presented, which finally allow to define the technology that is required for the excitation of ^{229m}Th. IC electrons emitted in the ground-state decay of ^{229m}Th were used. ^{229m}Th ions have been neutralized in graphene and the IC electrons were emitted in-flight, which made it possible to measure the isomeric energy free from any surface influence. A value for the isomeric excitation energy of 8.28 $\pm$0.17 eV was measured. The uncertainty is dominated by the systematic error originating from excited atomic states that are populated in the neutralization process.
Still, these results are sufficiently precise to define the laser technology that is needed to perform future precision laser spectroscopy of the ^{229}Th nuclear isomer. The measured energy corresponds to a wavelength of 149.7$\pm$3.1 nm, which is accessible with high-harmonic generation in a gas jet. Frequency combs operational in this energy region have been reported already [127]. Recently, all-solid-state frequency comb generation in the VUV range has been reported [128].

The new findings reported here pave the way towards a nuclear clock, which might reach and potentially surpass currently operated atomic clocks already employed in fundamental research as well as for applied science. As a prototypical and prominent example, the possibly enhanced sensitivity of a ^{229m}Th-based nuclear clock for temporal variations of fundamental constants like the fine-structure constant α make such a clock a promising tool for fundamental physics.
Moreover, a solid-state nuclear clock, where ^{229}Th is embedded in VUV transparent crystals, forming a novel and elegant concept for a nuclear frequency standard, is feasible in the energy region determined by this thesis.

7.2 Potential future experiments

In the following section future experiments that build on the findings of this thesis are proposed.

7.2.1 Isomer lifetime in free Th atoms

The lifetime of ^{229m}Th under internal conversion is only known for surface-bound ^{229m}Th atoms. As shown in chapter 5 the IC lifetime depends on the electronic environment of the surface. Therefore it is desirable to measure the isomeric lifetime in free thorium atoms. In the following, a simple experimental setup is proposed that can provide such a measurement and as well serve to identify the ^{229}Th isomer if laser spectroscopic [17] or soft-landing techniques on detector or catcher surfaces [4] are not applicable.

The setup is shown in Fig. 7.1. Similar to the energy measurements described in chapter 6, ^{229m}Th ion bunches are neutralized in flight by traversing a graphene foil. The atom bunches then enter a flight tube. It consists of a solenoid that generates a homogeneous magnetic transport field, whose axis coincides with the atom beam axis. In this way, IC electrons emitted in flight are axially confined by the magnetic field. By superimposing the magnetic field with a DC-field gradient, the IC electrons can be accelerated towards an electron detector. By a proper choice of the DC gradient, the IC electron detection can be considered to occur promptly ($\Delta T \approx$ 10 - 50 ns) after the decay. As in the lifetime measurements described in chapter 5, the lowest achievable lifetime that can be measured in this approach is connected to the falling edge of the ion bunch shape. The longest measurable lifetime is limited by the length of the flight tube, as the atoms will at some time impinge on the surface of the detector (leading to secondary electrons and subsequent surface-bound IC decay). Considering a velocity of $\approx 3\times10^4$ m/s

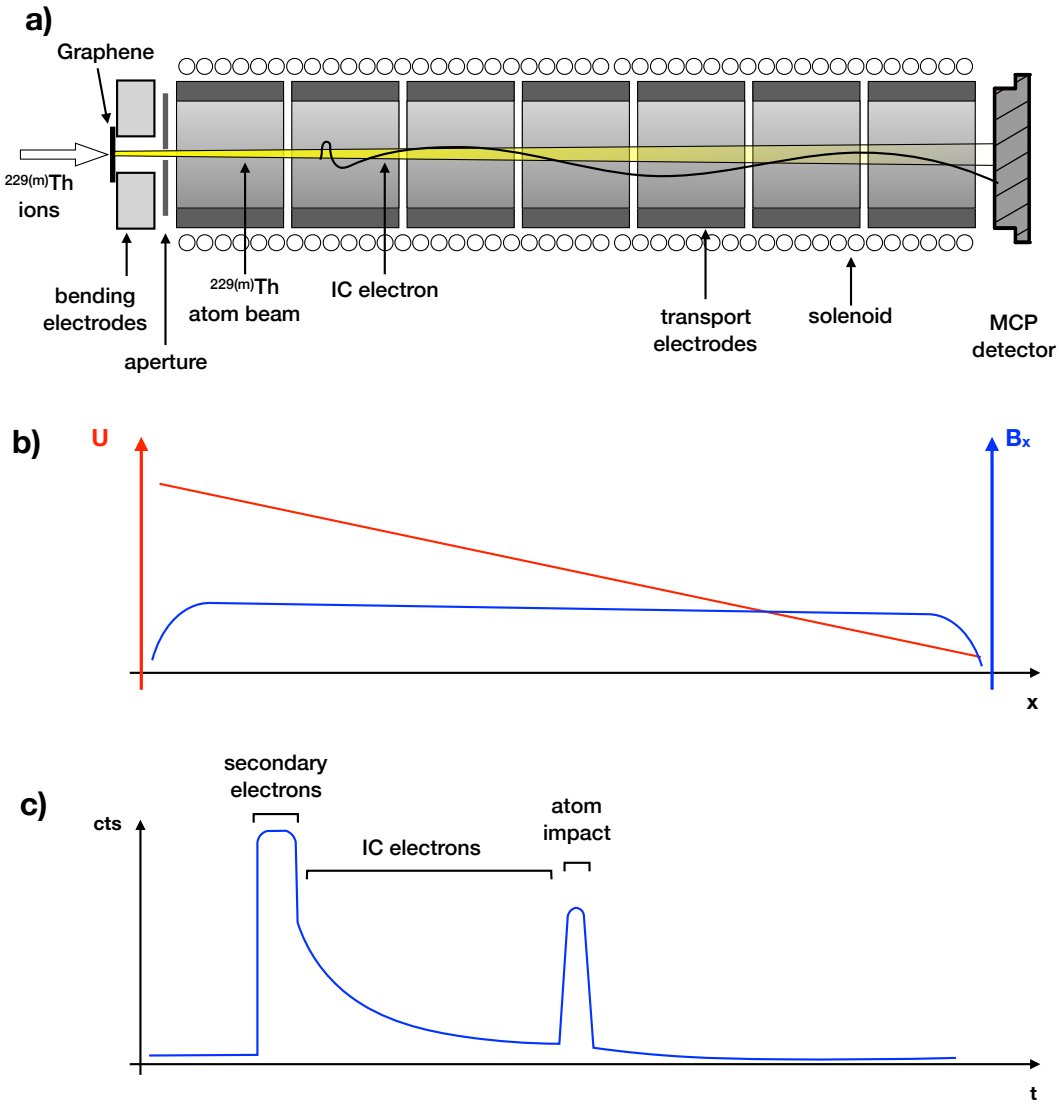

Figure 7.1: Proposed lifetime measurement of the thorium isomer in free ^{229m}Th atoms. a) Sketch of the experimental setup. b) DC-potential curve and magnetic field strength along the flight path of the atom. c) Qualitative sketch of the expected signal. Secondary electrons are due to the neutralization process. They can be potentially suppressed with bending electrodes. Conversion electrons form an exponential tail that can be separated from the secondary electrons. These IC electrons emitted from free Th atoms can be measured until the atoms impact on the detector surface, relase secondary electrons. The remaining surface-bound ^{229m}Th atoms will decay via IC on the surface.

(see Table 6.1, for $^{229m}Th^{3+}$ ions neutralized at a kinetic energy of 945 eV), the flight tube needs to have a length of ≈60 cm in order to measure IC electrons for to 20 μs.
As the IC decay rate is directly proportional to the reduced matrix element B(M1) (see Eq. (2.35)), a measurement of the isomeric lifetime in neutral thorium could enable an experimental determination of this value. However, as this approach also uses graphene to neutralize the ions, it can be expected that similar to the situation described for the energy measurements electronic excited states are populated whose exact distribution is not known. Therefore, not a single, but the sum of several decay constants will be measured, which might render the determination of B(M1) cumbersome.

7.2.2 Isomer lifetime measurements in solids

The unique feature of a nuclear clock is the opportunity to construct an operational solid-state optical clock. The nuclei can be embedded in a (VUV transparent, wide bandgap) crystal, which allows to address simultaneously a much larger number of nuclei than in a conventional ion trap. At present there is no scheme other than the measurement of γ decay of the isomer in the crystal. In the following, an experiment is proposed that does not use photons emitted during the decay, but electrons that are emitted by internal conversion inside a solid, comparable to an inner photo-effect.

Theoretical predictions indicate that the linewidth of the solid-state nuclear clock transition is not limited by the natural relative linewidth of the isomeric excitation (under the assumption of purely radiative decay) of 10^{-20}, but rather by influences of the crystal environment [48]. It is assumed that the linewidth of the transition is broadened to 0.5 to 10 kHz [48]. In an operational solid-state nuclear clock the narrow width of the transition (*i.e.* the long lifetime of the isomer) is not exploited. For this reason, IC does not need to be completely suppressed: it is sufficient to prolong the lifetime of the internal conversion decay by a factor of 10 to 100 (to 0.1 ms to 2 ms).
In measurements performed with the 76 eV isomer in ^{235}U it is found that the lifetime depends on the electronic environment of the nucleus [93], which was also observed for ^{229m}Th within the scope of the thesis. The measurements shown in section 5.3 indicate that the lifetime is shortened by a factor of about 2 for isomers which are deposited right on a metal surface.
Until today, no photons from the ground-state decay of ^{229m}Th were detected. Therefore it is proposed to measure IC electrons by implanting ^{229m}Th in the

depletion region of a semiconductor pn-junction under reverse bias.
This has two advantages compared to the conventional crystal-lattice approach:
1. it can be assumed that the lifetime of the isomer inside the silicon layer is equal or even longer than the one of Th atoms on a surface (measured as $\approx 10^{-5}$ s [11]). A prolongation of the IC lifetime by a factor of 10-200 could already be sufficient to be limited in the achievable clock performance by crystal temperature fluctuations [48].
2. the isomeric decay can be directly detected by (inner) internal conversion in the semiconductor. Novel silicon photomultipliers (SiPM) allow for single photon (or single electron) detection, which provides an efficient detection scheme for clock operation.

In the following, an experiment is proposed which might allow to perform measurements towards a solid-state nuclear optical clock along the conceptual idea sketched in the previous sentence. The experimental setup is similar to that used in the lifetime measurements, however, instead of collecting the ions on the surface of an MCP detector it is envisaged to implant them into the depletion region of a semiconductor detector. The idea is to use a VUV sensitive silicon photomultiplier (SiPM) for collection and detection of ^{229m}Th ions. There is a reason to use VUV sensitive SiPMs: normally SiPMs have a rather thick dead layer protecting the silicon. Infrared, visible and UV wavelengths can penetrate through the dead layer and still reach the depletion region to be finally detected. VUV photons, however, are absorbed within the first angstroms of the device. Therefore, VUV-sensitive SiPM have a very thin dead layer, meaning their sensitive region starts directly below the surface of the SiPM. This makes it possible to detect VUV photons. Moreover, this also allows for the detection of low-energy (above 1-3 keV) electrons and protons [129]. It is thus possible to deposit ^{229m}Th ions with low kinetic energy (some tens of keV) inside the sensitive region of the SiPM. If the isomer decays there via internal conversion, the electron is not emitted into vacuum but will be detected by the SiPM.
In a first proof-of-principle experiment ^{229m}Th ions could be implanted in a SiPM, which will allow to probe the lifetime of the isomer in a semiconductor environment and draw conclusions about the behaviour of the isomer in a solid state environment.

7.3 Summary & Outlook

Based on the results obtained in the course of this thesis project it is possible to further advance towards a nuclear clock. 40 years after the prediction of the isomer's existence, the presented measurements are the first to use decay products from the ground-state decay of $^{229\mathrm{m}}$Th, which allowed to directly measure properties of the ^{229}Th isomer.

The presented lifetime measurements confirm the strong dependence on the electronic environment and set a starting point for future investigations, as proposed for example in section 7.2.2. If well understood, the strong sensitivity on the chemical environment can also be used to investigate material properties. The spectroscopy of electrons emitted from surface-bound $^{229\mathrm{m}}$Th in its IC decay, which was only used qualitatively within this thesis, may also serve as a sensitive probe for surface properties.

The novel approach of neutralizing $^{229\mathrm{m}}$Th ions in graphene, that was used for the energy determination, did not only allow to measure the IC electron free from any surface influence, but might also lead to a new background-free detection scheme, as shown in section 7.2.1.

The energy determination experiments set the framework for further experiments to be performed: The comparison of the precision of the results ($\Delta E_{\mathrm{meas}}/E_I \approx 10^{-2}$) with the relative natural linewidth (of expectedly $\Delta E_{\mathrm{nat}}/E_I \approx 10^{-20}$), makes clear that there are still large hurdles to overcome along the way towards a nuclear clock. Strong improvements can be achieved in laser spectroscopy experiments: direct laser excitation of ^{229}Th atoms on a surface as propsed in Refs [74, 130] with an expected relative precision $\Delta E/E \approx 10^{-6}$ can be used as an intermediate step to reach the ultimate precision provided by a single-ion nuclear clock.

To finally conclude: the long way towards nuclear laser spectroscopy of $^{229(\mathrm{m})}$Th and ultimately towards a nuclear clock is paved.

Bibliography

[1] B. Seiferle, L. v.d. Wense, P.V. Bilous, I. Amersdorffer, C. Lemell, F. Libisch, S. Stellmer, T. Schumm, C.E. Düllmann, A. Pálffy, and P.G. Thirolf. Energy of the ^{229}Th nuclear clock transition. *Nature*, 573:243, 2019.

[2] J. K. Tuli. *Nuclear Wallet Cards*. National Nuclear Data Center, Brookhaven National Laboratory, 2011.

[3] A. D. Ludlow, M. M. Boyd, J. Ye, E. Peik, and P. O. Schmidt. Optical atomic clocks. *Rev. Mod. Phys.*, 87:637–701, 2015.

[4] L. v. d. Wense, B. Seiferle, M. Laatiaoui, J. B. Neumayr, H.-J. Maier, H.-F. Wirth, C. Mokry, J. Runke, K. Eberhardt, C. E. Düllmann, N. G. Trautmann, and P. G. Thirolf. Direct detection of the ^{229}Th nuclear clock transition. *Nature*, 533:47, 2016.

[5] E. V. Tkalya, C. Schneider, J. Jeet, and E. R. Hudson. Radiative lifetime and energy of the low-energy isomeric level in ^{229}Th. *Phys. Rev. C*, 92:054324, 2015.

[6] N. Minkov and A. Pálffy. Reduced transition probabilities for the gamma decay of the 7.8 eV isomer in ^{229}Th. *Phys. Rev. Lett.*, 118:212501, 2017.

[7] N. Minkov and A. Pálffy. Theoretical predictions for the magnetic dipole moment of ^{229m}Th. *Phys. Rev. Lett.*, 122:162502, 2019.

[8] T. Mayer-Kuckuk. *Kernphysik – eine Einführung*. Vieweg+Teubner Verlag, 1992.

[9] K. Bethge. *Kernphysik*. Springer-Verlag Berlin Heidelberg, 2008.

[10] S. Köhler, R. Deißenberger, K. Eberhardt, N. Erdmann, G. Herrmann, G. Huber, J.V. Kratz, M. Nunnemann, G. Passler, P.M. Rao, J. Riegel,

N. Trautmann, and K. Wendt. Determination of the first ionization potential of actinide elements by resonance ionization mass spectroscopy. *Spectrochimica Acta Part B: Atomic Spectroscopy*, 52(6):717 – 726, 1997.

[11] B. Seiferle, L. v. d. Wense, and P. G. Thirolf. Lifetime measurement of the ^{229}Th nuclear isomer. *Phys. Rev. Lett.*, 118:042501, 2017.

[12] F. F. Karpeshin and M. B. Trzhaskovskaya. Impact of the electron environment on the lifetime of the ^{229}Th^{m} low-lying isomer. *Phys. Rev. C*, 76:054313, 2007.

[13] J. F. Chemin, T. Carreyre, M. Aiche, F. Attallah, G. Bogaert, J. P. Grandin, M. Harston, W. E. Meyerhof, and J. N. Scheurer. A rare nuclear decay process: The internal conversion between bound atomic states. *Pramana*, 53(3):633–633, 1999.

[14] F.F. Karpeshin, I.M. Band, M.B. Trzhaskowskaya, and B.A. Zon. Study of ^{229}Th through laser-induced resonance internal conversion. *Physics Letters B*, 282(3):267 – 270, 1992.

[15] F. F. Karpeshin and M. B. Trzhaskovskaya. Bound internal conversion versus nuclear excitation by electron transition: Revision of the theory of optical pumping of the ^{229m}Th isomer. *Phys. Rev. C*, 95:034310, 2017.

[16] E.V. Tkalya. Probability of nonradiative excitation of nuclei in transitions of an electron in an atomic shell. *Journal of Experimental and Theoretical Physics*, 75(2):200 – 209, 1992.

[17] J. Thielking, M. V. Okhapkin, P. Głowacki, D. M. Meier, L. v. d. Wense, B. Seiferle, C. E. Düllmann, P. G. Thirolf, and E. Peik. Laser spectroscopic characterization of the nuclear-clock isomer ^{229m}Th. *Nature*, 556(7701):321–325, 2018.

[18] https://www.nndc.bnl.gov/ National Nuclear Data Center. Nudat 2.7.

[19] M. Verlinde et al. An alternative approach to populate and study the ^{229}Th nuclear clock isomer. *arXiv:1904.10245*, 2019.

[20] T. Masuda et al. X-ray pumping of the ^{229}Th nuclear clock isomer. *Accepted for publication in Nature*, 2019.

[21] L.A. Kroger and C.W. Reich. Features of the low-energy level scheme of ^{229}Th as observed in the γ-decay of ^{233}U. *Nuclear Physics A*, 259(1):29 – 60, 1976.

[22] M. J. Canty, R. D. Connor, D. A. Dohan, and B. Pople. The decay of 233U. *Journal of Physics G: Nuclear Physics*, 3(3):421, 1977.

[23] D. G. Burke, P. E. Garrett, Tao Qu, and R. A. Naumann. Additional evidence for the proposed excited state at $\leq$5 eV in ^{229}Th. *Phys. Rev. C*, 42:R499–R501, 1990.

[24] C. W. Reich and R. G. Helmer. Energy separation of the doublet of intrinsic states at the ground state of ^{229}Th. *Phys. Rev. Lett.*, 64:271–273, 1990.

[25] R. G. Helmer and C. W. Reich. An excited state of ^{229}Th at 3.5 eV. *Phys. Rev. C*, 49:1845–1858, 1994.

[26] G. M. Irwin and K. H. Kim. Observation of electromagnetic radiation from deexcitation of the ^{229}Th isomer. *Phys. Rev. Lett.*, 79:990–993, 1997.

[27] D. S. Richardson, D. M. Benton, D. E. Evans, J. A. R. Griffith, and G. Tungate. Ultraviolet photon emission observed in the search for the decay of the ^{229}Th isomer. *Phys. Rev. Lett.*, 80:3206–3208, 1998.

[28] S. B. Utter, P. Beiersdorfer, A. Barnes, R. W. Lougheed, J. R. Crespo López-Urrutia, J. A. Becker, and M. S. Weiss. Reexamination of the optical gamma ray decay in ^{229}Th. *Phys. Rev. Lett.*, 82:505–508, 1999.

[29] R. W. Shaw, J. P. Young, S. P. Cooper, and O. F. Webb. Spontaneous ultraviolet emission from ^{233}Uranium/^{229}Thorium samples. *Phys. Rev. Lett.*, 82:1109–1111, 1999.

[30] B. R. Beck, J. A. Becker, P. Beiersdorfer, G. V. Brown, K. J. Moody, J. B. Wilhelmy, F. S. Porter, C. A. Kilbourne, and R. L. Kelley. Energy splitting of the ground-state doublet in the nucleus ^{229}Th. *Phys. Rev. Lett.*, 98:142501, 2007.

[31] B. R. Beck, C. Y. Wu, P. Beiersdorfer, G. V. Brown, J.A. Becker, K. J. Moody, J. B. Wilhelmy, F. S. Porter, C. A. Kilbourne, and R. L. Kelley. Improved value for the energy splitting of the ground-state doublet in the nucleus ^{229m}Th. *LLNL-PROC-415170, Conference: Presented at: 12th International Conference on Nuclear Reaction Mechanisms, Varenna, Italy, Jun 15 - Jun 19, 2009.*

[32] Z. O. Guimarães Filho and O. Helene. Energy of the $3/2^+$ state of ^{229}Th reexamined. *Phys. Rev. C*, 71:044303, 2005.

[33] A. Kramida, Yu. Ralchenko, J. Reader, and and NIST ASD Team. NIST Atomic Spectra Database (ver. 5.6.1), [Online]. Available: `https://physics.nist.gov/asd` [2019, August 8]. National Institute of Standards and Technology, Gaithersburg, MD., 2018.

[34] E. R. Meyer, E. M. E. Timmermans, S. Rudin, J. D. Kress, L. A. Collins, and X. Zhao. Thorium-doped Csi: Implications for the thorium nuclear clock transition. *Phys. Rev. A*, 97:060503, 2018.

[35] W. Thomson and P.G. Tait. *Elements of Natural Philosophy*. Cambridge University Press, Cambridge, England, 1879.

[36] T. P. Heavner, S. R. Jefferts, E. A. Donley, J. H. Shirley, and T. E. Parker. NIST-f1: recent improvements and accuracy evaluations. *Metrologia*, 42(5):411–422, 2005.

[37] V. Gerginov, N. Nemitz, S. Weyers, R. Schröder, D. Griebsch, and R. Wynands. Uncertainty evaluation of the caesium fountain clock PTB-CSF2. *Metrologia*, 47(1):65–79, 2009.

[38] Bureau International des Poids et Mésures. The international system of units (SI).

[39] F. Riehle. *Frequency Standards Basics and Applications*. WILEY-VCH Verlag GmbH and Co. KGaA, Weinheim, 2004.

[40] T. Udem, R. Holzwarth, and T. W. Hänsch. Optical frequency metrology. *Nature*, 416:233, 2002.

[41] T. W. Hänsch. Nobel lecture: Passion for precision. *Rev. Mod. Phys.*, 78:1297–1309, 2006.

[42] John L. Hall. Nobel lecture: Defining and measuring optical frequencies. *Rev. Mod. Phys.*, 78:1279–1295, 2006.

[43] D. J. Berkeland, J. D. Miller, J. C. Bergquist, W. M. Itano, and D. J. Wineland. Minimization of ion micromotion in a paul trap. *Journal of Applied Physics*, 83(10):5025–5033, 1998.

[44] S. M. Brewer, J.-S. Chen, A. M. Hankin, E. R. Clements, C. W. Chou, D. J. Wineland, D. B. Hume, and D. R. Leibrandt. $^{27}Al^{+}$ quantum-logic clock with a systematic uncertainty below 10^{-18}. *Phys. Rev. Lett.*, 123:033201, 2019.

[45] E. Peik and Chr. Tamm. Nuclear laser spectroscopy of the 3.5 eV transition in Th-229. *EPL (Europhysics Letters)*, 61(2):181, 2003.

[46] C. J. Campbell, A. G. Radnaev, and A. Kuzmich. Wigner crystals of ^{229}Th for optical excitation of the nuclear isomer. *Phys. Rev. Lett.*, 106:223001, 2011.

[47] G. A. Kazakov, A. N. Litvinov, V. I. Romanenko, L. P. Yatsenko, A. V. Romanenko, M. Schreitl, G. Winkler, and T. Schumm. Performance of a ^{229}Thorium solid-state nuclear clock. *New Journal of Physics*, 14(8):083019, 2012.

[48] W. G. Rellergert, D. DeMille, R. R. Greco, M. P. Hehlen, J. R. Torgerson, and E. R. Hudson. Constraining the evolution of the fundamental constants with a solid-state optical frequency reference based on the ^{229}Th nucleus. *Phys. Rev. Lett.*, 104:200802, 2010.

[49] A. El-Rabbany. *Introduction to GPS: The Global Positioning System.* Artech House, Boston, MA., 2002.

[50] Y. Urlichich, V. Subbotin, G. Stupak, V. Dvorkin, A. Povaliaev, and S. Karutin. Glonass developing strategy,. *Proceedings of the 23rd International Technical Meeting of the Satellite Division of The Institute of Navigation (ION GNSS 2010), Portland, OR, September 2010*, 2010.

[51] E. Chatre. Galileo program status update. *Proceedings of the 30th International Technical Meeting of the Satellite Division of The Institute of Navigation (ION GNSS+ 2017), Portland, Oregon*, page 843, 2017.

[52] W. F. McGrew, X. Zhang, R. J. Fasano, S. A. Schäffer, K. Beloy, D. Nicolodi, R. C. Brown, N. Hinkley, G. Milani, M. Schioppo, T. H. Yoon, and A. D. Ludlow. Atomic clock performance enabling geodesy below the centimetre level. *Nature*, 564(7734):87–90, 2018.

[53] T. E. Mehlstäubler, G. Grosche, C. Lisdat, P. O. Schmidt, and H. Denker. Atomic clocks for geodesy. *Rept. Prog. Phys.*, 81(6):064401, 2018.

[54] J. P. Ostriker, P. J. E. Peebles, and A. Yahil. The size and mass of galaxies, and the mass of the universe. *Astrophys. J.*, 193:L1–L4, 1974.

[55] V. Trimble. Existence and nature of dark matter in the universe. *Annual Review of Astronomy and Astrophysics*, 25(1):425–472, 1987.

[56] P. G. Thirolf, B. Seiferle, and L. v. d. Wense. Improving our knowledge on the ^{229m}Thorium isomer: Toward a test bench for time variations of fundamental constants. *Annalen der Physik*, (531):1800381, 2019.

[57] J.-P. Uzan. The fundamental constants and their variation: observational and theoretical status. *Rev. Mod. Phys.*, 75:403–455, 2003.

[58] J.-P. Uzan. Varying constants, gravitation and cosmology. *Living Reviews in Relativity*, 14(1):2, 2011.

[59] J. K. Webb, M. T. Murphy, V. V. Flambaum, V. A. Dzuba, J. D. Barrow, C. W. Churchill, J. X. Prochaska, and A. M. Wolfe. Further evidence for cosmological evolution of the fine structure constant. *Phys. Rev. Lett.*, 87:091301, 2001.

[60] R. M. Godun, P. B. R. Nisbet-Jones, J. M. Jones, S. A. King, L. A. M. Johnson, H. S. Margolis, K. Szymaniec, S. N. Lea, K. Bongs, and P. Gill. Frequency ratio of two optical clock transitions in ^{171}yb^{+} and constraints on the time variation of fundamental constants. *Phys. Rev. Lett.*, 113:210801, Nov 2014.

[61] E. Litvinova, H. Feldmeier, J. Dobaczewski, and V. Flambaum. Nuclear structure of lowest ^{229}Th states and time-dependent fundamental constants. *Phys. Rev. C*, 79:064303, 2009.

[62] V. V. Flambaum, N. Auerbach, and V. F. Dmitriev. Coulomb energy contribution to the excitation energy in ^{229}Th and enhanced effect of variation. *EPL (Europhysics Letters)*, 85(5):50005, 2009.

[63] V. V. Flambaum and R. B. Wiringa. Enhanced effect of quark mass variation in ^{229}Th and limits from Oklo data. *Phys. Rev. C*, 79:034302, 2009.

[64] J. C. Berengut, V. A. Dzuba, V. V. Flambaum, and S. G. Porsev. Proposed experimental method to determine α sensitivity of splitting between ground and 7.6 eV isomeric states in ^{229}Th. *Phys. Rev. Lett.*, 102:210801, 2009.

[65] A. Fleischmann, C. Enss, and G.M. Seidel. Metallic magnetic calorimeters. In C. Enss, editor, *Cryogenic Particle Detection*, chapter 4, pages 151–216. Springer-Verlag Berlin Heidelberg, 2005.

[66] S. Kempf, A. Fleischmann, L. Gastaldo, and C. Enss. Physics and Applications of Metallic Magnetic Calorimeters. *Journal of Low Temperature Physics*, 193:365–379, 2018.

[67] G.A. Kazakov, V. Schauer, J. Schwestka, S.P. Stellmer, J.H. Sterba, A. Fleischmann, L. Gastaldo, A. Pabinger, C. Enss, and T. Schumm. Prospects for measuring the ^{229}Th isomer energy using a metallic magnetic microcalorimeter. *Nuclear Instruments and Methods in Physics Research Section A: Accelerators, Spectrometers, Detectors and Associated Equipment*, 735:229 – 239, 2014.

[68] C.M. Natarajan, M.G. Tanner, and R.H. Hadfield. Superconducting nanowire single-photon detectors: physics and applications. *Superconductor Science and Technology*, 25(6):063001, 2012.

[69] S. Stellmer, G. Kazakov, M. Schreitl, H. Kaser, M. Kolbe, and T. Schumm. Attempt to optically excite the nuclear isomer in ^{229}Th. *Phys. Rev. A*, 97:062506, 2018.

[70] J. Jeet, C. Schneider, S. T. Sullivan, W. G. Rellergert, S. Mirzadeh, A. Cassanho, H. P. Jenssen, E. V. Tkalya, and E. R. Hudson. Results of a direct search using synchrotron radiation for the low-energy ^{229}Th nuclear isomeric transition. *Phys. Rev. Lett.*, 114:253001, 2015.

[71] J. Jeet. *Search for the low lying transition in the ^{229}Th Nucleus*. PhD thesis, University of California, Los Angeles, 2018.

[72] D. M. Meier, J. Thielking, P. Głowacki, M. V. Okhapkin, R. A. Mller, A. Surzhykov, and Peik E. Electronic level structure of Th^+ in the range of the ^{229m}Th isomer energy. *arXiv:1902.09256*, 2019.

[73] J. Thielking and D. M. Meier. *Private Communication*, 2019.

[74] L. von der Wense, B. Seiferle, S. Stellmer, J. Weitenberg, G. Kazakov, A. Pálffy, and P. G. Thirolf. A laser excitation scheme for ^{229m}Th. *Phys. Rev. Lett.*, 119:132503, 2017.

[75] S.J. Hanna, P. Campuzano-Jost, E.A. Simpson, D.B. Robb, I. Burak, M.W. Blades, J.W. Hepburn, and A.K. Bertram. A new broadly tunable (7.4 − 10.2 eV) laser based VUV light source and its first application to aerosol mass spectrometry. *International Journal of Mass Spectrometry*, 279(2):134 – 146, 2009.

[76] H. Schomburg, H. F. Döbele, and B. Rückle. Generation of tunable narrow-bandwidth VUV radiation by anti-stokes SRS in H_2. *Applied Physics B*, 30(3):131–134, 1983.

[77] B. Seiferle, L. von der Wense, and P. G. Thirolf. Feasibility study of internal conversion electron spectroscopy of ^{229m}Th. *The European Physical Journal A*, 53(5):108, 2017.

[78] S. Stellmer, Y. Shigekawa, V. Rosecker, G. A. Kazakov, Y. Kasamatsu, Y. Yasuda, A. Shinohara, and T. Schumm. Toward an energy measurement of the internal conversion electron in the deexcitation of the ^{229}Th isomer. *Phys. Rev. C*, 98:014317, 2018.

[79] C. F. v. Weizsäcker. Zur Theorie der Kernmassen. *Zeitschrift für Physik*, 96(7):431–458, 1935.

[80] N. Takigawa and K. Washiyama. *Fundamentals of Nuclear Physics*. Springer Japan, 2017.

[81] R. Hofstadter. Electron scattering and nuclear structure. *Rev. Mod. Phys.*, 28:214–254, 1956.

[82] R. D. Woods and D. S. Saxon. Diffuse surface optical model for nucleon-nuclei scattering. *Phys. Rev.*, 95:577–578, 1954.

[83] S. G. Nilsson. Binding states of individual nucleons in strongly deformed nuclei. *Kong. Dan. Vid. Sel. Mat. Fys. Med.*, 29N16:1–69, 1955.

[84] R. B. Firestone, V.S. Shirley, and C.M. Baglin. *Table of isotopes CD-ROM*. Wiley, New York, 1996.

[85] A. M. Dykhne and E. V. Tkalya. Matrix element of the anomalously low-energy (3.5±0.5 eV) transition in ^{229}Th and the isomer lifetime. *Journal of Experimental and Theoretical Physics Letters*, 67(4):251–256, 1998.

[86] J.M. Blatt and V.F. Weiskopf. *Theoretical Nuclear Physics*. Springer-Verlag New York, 1979.

[87] P. V. Bilous. *Towards a nuclear clock with the ^{229}Th isomeric transition.* PhD thesis, University of Heidelberg, 2018.

[88] P. V. Bilous, G. A. Kazakov, I. D. Moore, T. Schumm, and A. Pálffy. Internal conversion from excited electronic states of ^{229}Th ions. *Phys. Rev. A*, 95:032503, 2017.

[89] P. V. Bilous, N. Minkov, and A. Pálffy. Electric quadrupole channel of the 7.8 eV ^{229}Th transition. *Phys. Rev. C*, 97:044320, 2018.

[90] P. Jönsson, G. Gaigalas, J. Bieron, C. Froese Fischer, and I.P. Grant. New version: Grasp2k relativistic atomic structure package. *Computer Physics Communications*, 184(9):2197 – 2203, 2013.

[91] S. Fritzsche. The ratip program for relativistic calculations of atomic transition, ionization and recombination properties. *Computer Physics Communications*, 183(7):1525 – 1559, 2012.

[92] F. Ponce, E. Swanberg, J. Burke, R. Henderson, and S. Friedrich. Accurate measurement of the first excited nuclear state in ^{235}U. *Phys. Rev. C*, 97:054310, 2018.

[93] M. Nève de Mévergnies. Chemical effect on the half-life of U^{235m}. *Phys. Rev. Lett.*, 23:422–425, 1969.

[94] M. Nève de Mévergnies. Perturbation of the ^{235m}U decay rate by implantation in transition metals. *Phys. Rev. Lett.*, 29:1188–1191, 1972.

[95] Y. Shigekawa, Y. Kasamatsu, Y. Yasuda, M. Kaneko, M. Watanabe, and A. Shinohara. Variation of half-life and internal-conversion electron energy spectrum between ^{235m}U oxide and fluoride. *Phys. Rev. C*, 98:014306, 2018.

[96] A. Arnau, F. Aumayr, P.M. Echenique, M. Grether, W. Heiland, J. Limburg, R. Morgenstern, P. Roncin, S. Schippers, R. Schuch, N. Stolterfoht, P. Varga, T.J.M. Zouros, and H.P. Winter. Interaction of slow multicharged ions with solid surfaces. *Surface Science Reports*, 27(4):113 – 239, 1997.

[97] M.L.E. Oliphant and E. Rutherford. The liberation of electrons from metal surfaces by positive ions. part i. *Proceedings of the Royal Society of London. Series A, Containing Papers of a Mathematical and Physical Character*, 127(805):373–387, 1930.

[98] H. D. Hagstrum. Theory of Auger ejection of electrons from metals by ions. *Phys. Rev.*, 96:336–365, 1954.

[99] H. D. Hagstrum. Auger ejection of electrons from tungsten by noble gas ions. *Phys. Rev.*, 104:317–318, 1956.

[100] H. Winter and F. Aumayr. Hollow atoms. *Journal of Physics B: Atomic, Molecular and Optical Physics*, 32(7):R39–R65, 1999.

[101] I. Amersdorffer. Charge exchange of $^{229(m)}$Th ions in carbon foils, Bachelor Thesis, LMU Munich, 2018.

[102] P. Hohenberg and W. Kohn. Inhomogeneous electron gas. *Phys. Rev.*, 136:B864–B871, 1964.

[103] W. Kohn and L. J. Sham. Self-consistent equations including exchange and correlation effects. *Phys. Rev.*, 140:A1133–A1138, 1965.

[104] U. Stroth. *Plasmaphysik − Phänomene, Grundlagen und Anwendungen.* Springer Spektrum, 2018.

[105] J. B. Neumayr. *The buffer-gas cell and the extraction RFQ for SHIPTRAP.* PhD thesis, LMU Munich, 2004.

[106] L. v.d. Wense. *On the direct detection of ^{229m}Th.* PhD thesis, LMU Munich, 2017.

[107] L. v.d. Wense, B. Seiferle, M. Laatiaoui, and P. G. Thirolf. Determination of the extraction efficiency for ^{233}U source α-recoil ions from the mll buffer-gas stopping cell. *The European Physical Journal A*, 51(3):29, 2015.

[108] G. L. Cano and R. W. Dressel. Energy loss and resultant charge of recoil particles from alpha disintegrations in surface deposits of ^{210}Po and ^{241}Am. *Phys. Rev.*, 139:A1883–A1892, 1965.

[109] J. Gal, Z. Hadari, E. Yanir, E.R. Bauminger, and S. Ofer. Charge states of np recoil atoms following decay. *Journal of Inorganic and Nuclear Chemistry*, 32(8):2509 – 2512, 1970.

[110] WM Brubaker. An improved quadrupole mass analyser. *Adv. Mass. Spectrom.*, 5:493–299, 1968.

[111] E. Haettner, W.R. Plaß, U. Czok, T. Dickel, H. Geissel, W. Kinsel, M. Petrick, T. Schäfer, and C. Scheidenberger. A versatile triple radiofrequency quadrupole system for cooling, mass separation and bunching of exotic nuclei. *Nuclear Instruments and Methods in Physics Research Section A: Accelerators, Spectrometers, Detectors and Associated Equipment*, 880:138 – 151, 2018.

[112] J. L. Wiza. Microchannel plate detectors. *Nuclear Instruments and Methods*, 162(1):587 – 601, 1979.

[113] *Technical Information – MCP Assembly*. Hamamatsu Photonics, K.K., `https://www.hamamatsu.com/resources/pdf/etd/MCP_TMCP0002E.pdf`, 2006.

[114] B. Seiferle, L. v.d. Wense, I. Amersdorffer, N. Arlt, B. Kotulski, and P.G. Thirolf. Towards a precise determination of the excitation energy of the thorium nuclear isomer using a magnetic bottle spectrometer. *Nuclear Instruments and Methods in Physics Research Section B: Beam Interactions with Materials and Atoms*, 2019.

[115] Y. Yamakita, H. Tanaka, R. Maruyama, H. Yamakado, F. Misaizu, and K. Ohno. A highly sensitive electron spectrometer for crossed-beam collisional ionization: A retarding-type magnetic bottle analyzer and its application to collision-energy resolved penning ionization electron spectroscopy. *Review of Scientific Instruments*, 71(8):3042–3049, 2000.

[116] D. A. Dahl. SIMION for the personal computer in reflection. *International Journal of Mass Spectrometry*, 200(1):3 – 25, 2000. Volume 200: The state of the field as we move into a new millenium.

[117] J. B. Boffard, M. E. Lagus, L. W. Anderson, and C. C. Lin. Apparatus for measuring electron impact excitation cross sections using fast metastable atoms produced via charge exchange. *Review of Scientific Instruments*, 67(8):2738–2751, 1996.

[118] P.J. Schneider, W. Eckstein, and H. Verbeek. Charge states of reflected particles for grazing incidence of D+, D2+ and D0 on Ni and Cs targets. *Nuclear Instruments and Methods in Physics Research*, 194(1):387 – 390, 1982.

[119] E. Gruber, R. A. Wilhelm, R. Pétuya, V. Smejkal, R. Kozubek, A. Hierzenberger, B. C. Bayer, I. Aldazabal, A. K. Kazansky, F. Libisch, A. V.

Krasheninnikov, M. Schleberger, S. Facsko, A. G. Borisov, A. Arnau, and F. Aumayr. Ultrafast electronic response of graphene to a strong and localized electric field. *Nature Communications*, 7:13948, 2016.

[120] K. Harada, T. Wada, and T. Tanaka. Near-infrared diode laser spectroscopy of the (2, 0) band of the $A^2\pi_u$-$X^2\sigma_g^+$ system of the N_2^+ ion. *Journal of Molecular Spectroscopy*, 163(2):436 – 442, 1994.

[121] C. J. Schmitt. *Equilibrium charge state distributions of low-Z ions incident on thin self-supporting foils*. PhD thesis, University of Notre Dame, Indiana, USA, 2010.

[122] F.F. Karpeshin and M.B. Trzhaskovskaya. Impact of the ionization of the atomic shell on the lifetime of the 229mth isomer. *Nuclear Physics A*, 969:173 – 183, 2018.

[123] Young-Jun Yu, Yue Zhao, Sunmin Ryu, Louis E. Brus, Kwang S. Kim, and Philip Kim. Tuning the graphene work function by electric field effect. *Nano Letters*, 9, 2009.

[124] S. K. Roy, R. Prasad, and P. Chandra. Electron correlation and relativistic effects in atomic structure calculations of the thorium atom. *The Journal of Chemical Physics*, 134(23):234302, 2011.

[125] R.G. Behrens, M. Bickel, R. Engleman, J. Fuger, L.E. Grimes, B. Kanellakopulos, D.J. Lam, K. Roessler, and B. Veal. *Gmelin Handbook of Inorganic Chemistry. Th Thorium. Supplement Volume A 4, General Properties. Spectra. Recoil Reactions*. Springer, 1989.

[126] Yun Zhang, Yusuke Sato, Nobuyoshi Watanabe, Riskey Ananda, Yoshiko Okada-Shudo, Masayoshi Watanabe, Masaharu Hyodo, Xiaoyang Wang, Chuangtian Chen, Teruto Kanai, and Shuntaro Watanabe. Generation of quasi-continuous-wave vacuum-ultraviolet coherent light by fourth-harmonic of a Ti:sapphire laser with KBBF crystal. *Opt. Express*, 17(10):8119–8124, 2009.

[127] A. Ozawa and Y. Kobayashi. VUV frequency-comb spectroscopy of atomic xenon. *Phys. Rev. A*, 87:022507, 2013.

[128] J. Seres, E. Seres, C. Serrat, E. C. Young, J. S. Speck, and T. Schumm. All-solid-state VUV frequency comb at 160 nm using high-harmonic generation in nonlinear femtosecond enhancement cavity. *Opt. Express*, 27(5):6618–6628, 2019.

[129] K. Ogasawara, F. Allegrini, M. A. Dayeh, M. I. Desai, S. A. Livi, Y. Hakamata, K. Sato, K. Ujihara, and R. Yamada. UV-grade silicon photomultipliers for direct counting of low-energy electrons and protons. *IEEE Transactions on Nuclear Science*, 64(10):2733–2741, 2017.

[130] L. v.d. Wense and C. Zhang. Concepts for direct frequency-comb spectroscopy of ^{229m}Th. *Preprint, arXiv:1905.08060*, 2019.

APPENDIX A

MatLab Code for the lifetime measurement simulations

Given an excited state (or particle) with a decay constant λ, the probability for it to decay within a time interval $t + \delta$ is given by $p = \lambda \cdot \delta$ (for $\lambda \cdot \delta << 1$). This is used in the Monte-Carlo simulation that were used in Sect. 5.1 to simulate the decay behavior of Th isomers which are accumulated in bunches on an MCP detector.

The central function of the MatLab code for the generation of the Monte Carlo simulations of the lifetime measurements (Sect. 5.1) is displayed below. The input variables which are used are

- `Bunch`: The temporal structure of the ion bunch that is accumulated. Each entry `Bunch(t)` contains the counts per time interval `[t*t_bin (t+1)*t_bin]`.
- `t_bin`: Binning/time interval length that is used in the simulation.
- `lambda`: Decay constant λ of the isomeric decay ($\lambda = 1/\tau = \log 2/t_{1/2}$).
- `iso_branch`: Branching ratio of ions which are in the isomeric state (as the isomer is populated in the ^{233}U α-decay, a branching ratio of 2% was used).
- `N_total_Bunch`: Total number of ions per bunch.

The isomeric activity resulting from the accumulation of a bunch with a shape defined by `Bunch` is then output as `Bunch_activ`. `Bunch_activ(t)` reflects the number of isomeric decays in the time interval `[t*t_bin (t+1)*t_bin]`.

```
function Bunch_activ = calcActivityMC(Bunch, t_bin,
   lambda, iso_branch, N_total_Bunch)

Bunch_activ = [];

Bunch = Bunch/(sum(Bunch))*iso_branch*N_total_Bunch;
N = 0;
N_loop = 0;
R = lambda*t_bin;

for t = 1 : length(Bunch)

    N = N + Bunch(t);
    N_loop = N;

    for k = 1:N
        rnd = rand(1);
        if rnd < R
            N = N-1;
        end
    end
    Bunch_activ(t) = N_loop-N;
end
%%NOISE
for t = 1 : length(Bunch)

    if rand(1)<t_bin * 5
    Bunch_activ(t) = Bunch_activ(t) + 1;
    end

end

end
```

In the simulations shown in Sect. 5.1 the above function is called N_{bunch} times (where N_{bunch} is the number of accumulated bunches) and the resulting activities were then added and plotted.

APPENDIX B

List of excited states

Below a list can be found with the excited states that are considered in the energy determination. The data is taken from `http://web2.lac.u-psud.fr/lac/Database/Tab-energy/Thorium/Th-tables/` where also mixing components are listed that were considered in the calculation of the internal conversion electron spectra.

even states			**odd states**		
State index	E_i [cm^{-1}]	configuration	State index	E_i [cm^{-1}]	configuration
1	0	$6d^27s^2$	1	7795.275	5f 6d $7s^2$
2	2558.057	$6d^27s^2$	2	8243.601	5f 6d $7s^2$
3	2869.259	$6d^27s^2$	3	10414.136	5f 6d $7s^2$
4	3687.987	$6d^27s^2$	4	10526.544	5f 6d $7s^2$
5	3865.475	$6d^27s^2$	5	10783.154	6d $7s^2$ 7p
6	4961.659	$6d^27s^2$	6	11197.031	5f 6d $7s^2$
7	5563.142	$6d^37s$	7	11241.730	5f 6d $7s^2$
8	6362.396	$6d^37s$	8	11877.839	6d $7s^2$ 7p
9	7280.124	$6d^27s^2$	9	12114.366	5f 6d $7s^2$
10	7502.288	$6d^37s$	10	13175.113	5f 6d $7s^2$
11	8111.005	$6d^27s^2$	11	13945.307	6d $7s^2$ 7p
12	8800.251	$6d^37s$	12	14032.085	6d $7s^2$ 7p
13	9804.807	$6d^37s$	13	14206.917	5f 6d $7s^2$
14	11601.031	$6d^37s$	14	14243.993	5f 6d $7s^2$
15	11802.934	$6d^37s$	15	14247.307	5f 6d $7s^2$
16	12847.971	$6d^37s$	16	14465.222	6d $7s^2$ 7p
17	13088.563	$6d^37s$	17	14481.869	5f 6d $7s^2$
18	13297.434	$6d^37s$	18	15166.901	6d $7s^2$ 7p
19	13847.771	$6d^37s$	19	15490.077	5f 6d $7s^2$
20	13962.522	$6d^37s$	20	15618.984	5f 6d $7s^2$
21	14204.264	$6d^37s$	21	15736.969	6d $7s^2$ 7p
22	14226.822	$6d^37s$	22	16217.482	6d $7s^2$ 7p
23	15493.221	$6d^37s$	23	16346.651	5f 6d $7s^2$
24	15863.891	$6d^37s$	24	16783.847	5f 6d $7s^2$
25	15970.095	$6d^37s$	25	17224.303	6d $7s^2$ 7p
26	16351.943	$6d^27s^2$	26	17354.639	5f 6d $7s^2$
27	16554.245	$6d^37s$	27	17411.224	6d $7s^2$ 7p
28	17073.811	$6d^37s$	28	17501.176	5f 6d $7s^2$
29	17166.108	$6d^37s$	29	17847.077	5f 6d $7s^2$
30	17398.398	$6d^37s$	30	18011.380	5f 6d $7s^2$
31	17959.898	$6d^37s$	31	18053.617	6d $7s^2$ 7p
32	18431.686	5f $7s^2$ 7p	32	18069.065	6d $7s^2$ 7p
33	18549.405	$6d^37s$	33	18382.826	$6d^2$ 7s 7p
34	18574.608	$6d^37s$	34	18614.338	$6d^2$ 7s 7p
35	18699.623	5f $7s^2$ 7p	35	18809.887	$6d^2$ 7s 7p
36	19273.279	$6d^37s$	36	18930.293	$6d^2$ 7s 7p
37	19532.419	$6d^37s$	37	19039.153	6d $7s^2$ 7p
38	19713.031	$6d^37s$	38	19227.336	6d $7s^2$ 7p
39	19832.116	$6d^37s$	39	19503.144	6d $7s^2$ 7p
			40	19516.981	6d $7s^2$ 7p
			41	19588.362	6d $7s^2$ 7p
			42	19817.182	6d $7s^2$ 7p
			43	19948.395	6d $7s^2$ 7p
			44	19986.166	5f 6d $7s^2$

Table B.1: List of all states in the Th atom below 20000 cm^{-1} (2.5 eV) that are considered in the analysis. Full data can be found on `http://web2.lac.u-psud.fr/lac/Database/Tab-energy/Thorium/Th-tables/`.

APPENDIX C

Voltage Settings

	Source offset	**RF+DC Funnel**				*Nozzle*	**RFQ Buncher**							**QMS**				**Triode**			*Focus*	*Graphene*	*Comments*
	[V]	Offset [V]	Gradient [V per cm]	V_{pp} [V]	f [kHz]	[V]	Offset [V]	Gradient [V per segment]	Trap [V]			V_{pp} [V]	f [kHz]	Offset [V]	f [kHz]	V_{pp} [V]	U_{DC} [V]	[V]			[V]	[V]	
Lifetime Measurements	80	23	−4	120	850	22	21.8	−0.2	18	15	34	160	880	−2	925	600.5	50.15	−2	−62	−22	/	/	$^{229}Th^{2+}$
	80	23	−4	120	850	22	21.8	−0.2	18	15	34	160	880	−2	925	901.2	75.23	−2	−62	−22	/	/	$^{229}Th^{2+}$
Energy Measurements	80	23	−4	120	850	22	21.8	−0.2	18	15	34	160	880	−2	925	≈500	0	−2	−75	−120	−300	−300	no mass separation

Table C.1: Table that contains all voltages that were set in the experiments. The RF+DC funnel offset is the offset voltage applied to the ring electrode next to the nozzle. The RFQ offset is the offset voltage applied to the first RFQ segment. The gradients are given in the direction of the ion beam (from source to detector).

Publication List

1. Benedict Seiferle, Lars v.d. Wense, Pavlo V. Bilous, Ines Amersdorffer, Chirstoph Lemell, Florian Libisch, Simon Stellmer, Thorsten Schumm, Christoph E. Düllmann, Adriana Pálffy, and Peter G. Thirolf. *Energy of the ^{229m}Th nuclear clock transition.*, Nature 573, 243 (2019).

2. Benedict Seiferle, Lars v.d. Wense, Ines Amersdorffer, Nicolas Arlt, Benjamin Kotulski, and Peter G. Thirolf. *Towards a precise determination of the excitation energy of the thorium nuclear isomer using a magnetic bottle spectrometer.* accepted for publication in Nucl. Instrum. Meth. B (2019).

3. Peter G. Thirolf, Benedict Seiferle, Lars v.d. Wense, *Improving Our Knowledge on the ^{229m}Thorium Isomer: Toward a Test Bench for Time Variations of Fundamental Constants.* Annalen der Physik, 1800381 (2019).

4. Peter G. Thirolf, Benedict Seiferle Lars v.d. Wense, *The 229-thorium isomer: doorway to the road from the atomic clock to the nuclear clock* Journal of Physics B: Atomic, Molecular and Optical Physics, accepted for publication (2019).

5. Peter G. Thirolf, Benedict Seiferle Lars v.d. Wense, *Ein Solitair der Kernphysik: mit dem Thorium-Isomer auf dem Weg zur Kernuhr* Physik Journal, accepted for publication (2019).

6. Lars v.d. Wense, Benedict Seiferle, Ines Amersdorffer, Peter G. Thirolf, *Generation of high-quality beams of the thorium isomer ^{229m}Th.* Journal of Visualized Experiments 147, e58516 (2019).

7. Lars v.d. Wense, Benedict Seiferle, Christian Schneider, Justin Jeet, Ines Amersdorffer, Nicolas Arlt, Florian Zacherl, Raphael Haas, Dennis Renisch, Patrick Mosel, Philip Mosel, Milutin Kovacev, Uwe Morgner, Christoph

E. Düllmann, Eric R. Hudson, Peter G. Thirolf, *The concept of a laser-based conversion electron nuclear Mssbauer spectroscopy for a precise energy determination of ^{229m}Th*, Hyperfine Interactions 240, 23 (2019).

8. Johannes Thielking, Maxim V. Okhapkin, Przemyslaw Głowacki, David M. Meier, Lars v.d. Wense, Benedict Seiferle, Christoph E. Düllmann, Peter G. Thirolf, and Ekkehard Peik. *Laser spectroscopic characterization of the nuclear-clock isomer ^{229m}Th.* Nature, 556:321, (2018).

9. Lars v.d. Wense, Benedict Seiferle, Peter G. Thirolf, *Towards a ^{229}Th based nuclear clock.* Measurement Techniques 60, 1178-1192 (2018).

10. Lars v.d. Wense, Benedict Seiferle, Simon Stellmer, Johannes Weitenberg, Georgy Kazakov, Adriana Pálffy, and Peter G. Thirolf. *A laser excitation scheme for ^{229m}Th.* Phys. Rev. Lett., 119:132503, (2017).

11. Benedict Seiferle, Lars v.d. Wense, and Peter G. Thirolf. *Lifetime measurement of the ^{229}Th nuclear isomer.* Phys. Rev. Lett., 118:042501, (2017).

12. Benedict Seiferle, Lars v.d. Wense, and Peter G. Thirolf. *Feasibility study of internal conversion electron spectroscopy of ^{229m}Th.* The European Physical Journal A, 53(5):108, (2017).

13. Lars v.d. Wense, Benedict Seiferle, Mustapha Laatiaoui, Jurgen B. Neumayr, Hans- Jörg Maier, Hans-Friedrich Wirth, Christoph Mokry, Jörg Runke, Klaus Eberhardt, Christoph E. Düllmann, Norbert G. Trautmann, and Peter G. Thirolf. *Direct detection of the ^{229}Th nuclear clock transition.* Nature, 533:47 (2016).

14. Benedict Seiferle, Lars v.d. Wense, Mustapha Laatiaoui, and Peter G. Thirolf, *A VUV detection system for the direct photonic identification of the first excited isomeric state of ^{229}Th.* Eur. Phys. J. D, 70(3):58, (2016).

15. Lars v.d. Wense, Benedict Seiferle, Mustapha Laatiaoui, Peter G. Thirolf, *The extraction of $^{229m}Th^{3+}$ from a buffer-gas stopping cell*, Nucl. Instr. Meth. B 376, 260 (2016).

16. Lars v.d. Wense, Benedict Seiferle, Mustapha Laatiaoui, and Peter G. Thirolf. *Determination of the extraction efficiency for ^{233}U source α-recoil ions from the MLL buffer-gas stopping cell.* Eur. Phys. J. A, 51(3):29, (2015).

List of Presentation

List of conference or seminar presentations:

1. Advanced Seminar on Condensed Matter Physics, Kirchhoff Institute for Physics, University of Heidelberg: "*Energy of the ^{229}Th nuclear clock transition*", November 2019. **invited**
2. ISTROS 2019, Bratislava, Slovakia: "*Energy of the ^{229}Th nuclear clock transition*", October 2019. **invited**
3. PSI Seminar, TU Munich: "*Energy of the ^{229}Th nuclear clock transition*", May 2019. **invited**
4. LS Parodi Group Seminar, LMU Munich: "*Energy of the ^{229}Th nuclear clock transition*", May 2019.
5. DPG Frühjahrstagung München 2019, "*Towards a direct energy determination of the ^{229}Th nuclear isomer*", March 2019.
6. DPG Frühjahrstagung Rostock 2019, "*Towards a direct energy determination of the ^{229}Th nuclear isomer*", Hauptvortrag, March 2019. **invited**
7. Thorium Energy World 2018, Brussels (Belgium),"*Internal conversion electron spectroscopy of ^{229m}Th*", October 2018. **invited**
8. International NOCAN Conference (676. Heraeus Seminar), Bad Honnef,"*Internal conversion electron spectroscopy of ^{229m}Th*", July 2018. **Hot Topic Talk**
9. DPG Frühjahrstagung Bochum 2018, Bochum,"*Towards a precise energy determination of the ^{229}Th nuclear clock transition*", March 2018.
10. Topical Workshop on Modern Aspects in Nuclear Structure, Bormio (Italy), "*Internal Conversion Electron Spectroscopy of ^{229m}Th*", February 2018.

11. SPES NUSPRASEN Workshop, Pisa (Italy), "*Internal Conversion Electron Spectroscopy of ^{229m}Th*", February 2018. **invited**

12. LS Schätz Group Seminar, University of Freiburg, Freiburg, "*Internal Conversion Electron Spectroscopy of ^{229m}Th*", January 2018.

13. LS Parodi Group Seminar, LMU Munich, Munich, "*Internal Conversion Electron Spectroscopy of ^{229m}Th*", November 2017.

14. nuClock Meeting, Max-Planck-Institute Heidelberg, "*Internal Conversion Electron Spectroscopy of ^{229m}Th*", September 2017.

15. ARIS 2017, Keystone (Colorado), USA, "*Lifetime measurement of the internal conversion decay of ^{229m}Th*", May 2017. **invited**

16. DPG Frühjahrstagung Münster 2017, Münster,"*Lifetime measurement of the internal conversion decay channel of ^{229m}Th*", March 2017.

17. LS Parodi Group Seminar, LMU Munich, Munich, "*New results from ^{229}Th*", July 2016.

18. DPG Frühjahrstagung Heidelberg 2015, Münster,"*A VUV detection system for the direct identification of the fluorescence radiation of ^{229m}Th*", March 2017.

List of posters:

1. FoQus Conference, Innsbruck (Austria), "*Energy of the ^{229}Th nuclear clock transition*", February 2019.

2. DPG Frühjahrstagung Darmstadt 2016, "*Prospects for an energy determination of the ^{229m}Th nuclear isomer via IC electrons*", March 2016.

Acknowledgements

At first I would like to express my greatest gratitude to PD Dr. Peter G. Thirolf for his supervision and for giving me the opportunity to work on this interesting experiment. His expertise and knowledge were a tremendous support that significantly helped to turn this difficult endeavour into a great success.

I would also like to add my greatest thanks to Dr. Lars von der Wense for his support, his physical insights and his encouragement to pursue new ideas. I will keep the uncountable hours we were working on the stopping cell, as well as the muffin+coffee discussion breaks, but also the hiking trips and other fun times besides thorium in very good memory.

I would like to thank the people who were involved in this work and helped to make the experiments run! Especially Ines Amersdorffer, Florian Zacherl, Nicolas Arlt and Benjamin Kotulski.

I want to express special thanks to Dr. Pavlo Bilous, Brenden Nickerson and PD Dr. Adriana Pálffy at the Max-Planck-Institut für Kernphysik in Heidelberg for the great support and insightful discussions about internal conversion and the interpretation of the spectra.

I would like to thank the thorium-group at PTB Braunschweig for hosting me for some days and for very helpful discussions with Dr. Maksim Okapkhin, Johannes Thielking, Dr. David-Marcel Meier, Gregor Zitzer and Dr. Ekkehard Peik.

I want to express my thanks to Prof. Dr. Thorsten Schumm from the Technical University of Vienna and Prof. Dr. Simon Stellmer from the University of Bonn for managing the nuClock project, for stimulating discussions, the temporary loan of equipment and also for good company during several conferences.

I want to thank Dr. Christoph Lemell and Dr. Florian Libisch for helping to understanding the neutralization of thorium in graphene.

I would like to express my gratitude to Dr. Johannes Weitenberg and Prof. Dr. Thomas Udem from the Max-Planck Institut für Quantenoptik for insights into

frequency combs.

I want to express my thanks to Dr. Andreas Ulrich for helping with the very first calibration measurements and Prof. Dr. Peter Feulner for valuable discussions on electron spectroscopy. I especially want to thank our lab neighbors from the UCN group at the Technical University of Munich, Dr. Christian Bocquet, Werner Adler, Johann Schlicher and Dr. Andreas Frei for helping with any technical problems.

I would like to thank Dr. Galen O'Neill & Dr. Sae-Woo Nam from NIST, Dr. Christian Schneider & Dr. Justin Jeet from UCLA, and Kjeld Beeks & Marion Mallweger from the TU Vienna for good times at the experiment and fruitful discussions.

I thank Prof. Dr. Christoph E. Düllmann and his group at the University of Mainz for providing the Uranium sources which were indispensable for our experiments.

I am indebted to the mechanical workshop at LMU, especially to Rolf Oehm for very instructive discussions and support with technical drawings. I also want to thank Johann Krapfl for supporting our group in the electronics workshop.

I am also indebted to Prof. Dr. Katia Parodi and the chair of medical physics. I especially want to thank my colleagues Tim Binder, Dr. Christine Weber, Dr. Saad Aldawood, Dr. Munetaka Nitta, Franz Siegfried Englbrecht, Dr. Silvia Liprandi, Michael Mayerhofer, Dr. Matthias Würl, Dr. Jonathan Bortfeld, Prof. Dr. Jörg Schreiber, Daniel Haffa, Peter Hilz and Andrea Leinthaler.

Without the help of my family and friends this work would not have turned out as it is. I would like to thank my parents and family for their encouragement and unconditional support. I want to thank Andreas, Philipp, Anja, Dennis, Jonas, Anna, Franz, Benni, Niko, Miles and Jan. Finally I want to thank Julia for her support, patience and understanding: Thank you!